DISSERTATION

RADIOFREQUENCY HEATING OF NANOCLUSTERS AND NANOPARTICLES FOR ENZYME ACTIVATION

Submitted by

Christian Blake Collins

Department of Chemistry

In partial fulfillment of the requirements

For the Degree of Doctor of Philosophy

Colorado State University

Fort Collins, Colorado

Summer 2018

Doctoral committee:

Advisor: Christopher Ackerson

Alan van Orden
Rick Finke
George Collins

ABSTRACT

RADIOFREQUENCY HEATING OF NANOCLUSTERS AND PARTICLES FOR ENZYME ACTIVATION

Radiofrequency (RF) fields heat magnetic nanoparticles. Applications include remote drug delivery and noninvasive cancer therapy. The underlying objective is to increase temperatures precisely where desired without heating the surroundings. Before our work, the replicable limit of this precision has been in the micrometer range. To investigate the lower limit of this concept of local heat, we explored the RF remote activation of a thermophilic enzyme, thermolysin, covalently attached to gold coated iron oxide nanoparticles (6.1 nm in core diameter). Thermolysin activity was a function of applied radiofrequency power, independent of bulk solution temperature. Besides iron oxides, many other inorganic nanomaterials have been investigated for RF heating. One of the more interesting and controversial material choices is gold nanoparticles, primarily investigated for cancer treatment. Early reports of gold nanoparticle heating conflated the heating of supporting electrolytes with the heating of nanoparticles. Multiple mechanisms were proposed to account for the observed heat of gold nanoparticle suspensions. There was no consensus among specialists on how gold nanoparticles heat, if they heat at all. To investigate this, a critical review of the RF heating of gold nanoparticles field was performed with new experimental results presented to elucidate the confounding results. Following this, $Au_{25}(SR)_{18}$ gold nanoclusters were used as a model system to investigate the controversial heating

rates reported for gold nanoparticles. For the first time the observed rates were explained entirely with a single mechanism: electrophoretic heating. The success of this reconciliation of theory and experiment considered the screened charge of the particle in addition to the contribution of the counterions. To enable deconvolution of possible contributions to gold nanoparticle heating by cluster decomposition products, an investigation of the practical stability of gold nanoclusters was conducted. It was found that organo-soluble particles with large ligands possessed over one-month long lifetime in air-free non-polar solvents.

ACKNOWLEDGEMENTS

First and foremost, I need to thank Chris Ackerson for giving me the opportunity to work in his lab. I got to work on some neat science while working with great people; it doesn't get much better than that. Chris has been the best advisor I could have imagined for this experience. I had many struggles during this project and Chris was patient and supportive the whole time, allowing me to get through the struggles on my own in a way that was most beneficial for my development and education.

I have had the pleasure of working with amazing colleagues and collaborators who have helped immensely along the way. I'm so grateful for everyone who helped me when I first joined the lab. Specifically, the support I received from Scott Compel, Marcus Tofanelli, Andrea Wong, and Thomas Ni is gratefully acknowledged. It was amazing to have colleagues that were brilliant and a true pleasure to be around. They helped alleviate the almost constant feeling of being in way over my head. I can confidently say that I will always consider these people to be friends. Besides the initial group of friends/colleagues, the Ackerson lab has attracted many more brilliant and wonderful people with whom I've been lucky enough to work with and learn from.

My family has been incredibly supportive during this whole pursuit. They were very good at pretending to be interested in my research and not asking me when I'm going to be finished or what I'm going to do with the degree too much. An invaluable part of my family is my dog, Annabel; she has been incredibly comforting during this whole experience and it's amazing how many times a long walk with her has been exactly what I needed to turn a day around or brainstorm new ideas for research.

TABLE OF CONTENTS

CHAPTER 1: AN INTRODUCTION TO HEATING NANOMATERIALS IN RADIOFREQUENCY FIELDS

1.1 Synopsis

The generation of heat through the interaction between nanomaterials and electromagnetic fields in the infrared, radio and microwave frequencies has been explored for many applications. Heating mechanisms and potential applications vary widely depending on the frequency and nanomaterial being used. There is a consensus of heating mechanisms in the infrared (IR) and microwave range, and magnetic heating in the radiofrequency (RF) range, but observed heating rates of gold particles in RF fields remain somewhat mysterious. It also remains to be seen whether regions of local heat can be generated around nanoparticles with useful applications. These concepts are discussed to provide context for the work that follows.

1.2 Introduction and history

The first report of nanoparticles being used to generate heat in radiofrequency fields was in 1957 when a team of surgeons lead by Bruce Taylor were able to heat lymph tissue samples with 20-100 nm diameter iron-oxide nanoparticles in 1.2 MHz fields.[1] Since this seminal work, many investigations into different nanomaterials, frequencies, and fields have been performed to understand this phenomenon and its applications. The most common applications for heating iron-oxide nanoparticles have been noninvasive tumor therapy[2–7] (i.e., cancer hyperthermia), and remote drug delivery.[8–10] Cancer hyperthermia is a treatment where heat from nanoparticles induces apoptosis in cancer cells, leading to their death. Remote drug delivery is accomplished by loosely associating drugs with the ligand layer of a nanoparticle or encapsulating the

drug and nanoparticle in a liposome and then heating the particle to release the drug payload. The nanoparticles absorb heat from the RF fields as work is being done on the particle by the field. There is a strong consensus that magnetic particles absorb energy from magnetic fields as the magnetic moment is torqued by the alternating magnetic field.[2-6,10,11]

In 2002 a report in Nature by Hamad-Schifferli found that gold particles appeared to heat in AC fields and DNA hair pins could be melted with heat from the nanoparticles.[12] They briefly proposed the heat could be due to induction; the same phenomena that causes the heating of bulk metals in RF fields. Subsequently dozens of reports of gold nanoparticles heating in RF fields were published, attributing the observed heat to numerous possible mechanisms.[13–15] Unfortunately there is no consensus on how RF fields interact with particles without ferromagnetic ordering to produce heat. None of the proposed mechanisms can theoretically account for the observed heating rates. In fact, there is much debate in the field about whether gold nanoparticles absorb enough energy from RF fields to produce any measurable heat.[16,17]

1.3 Gold nanoparticle introduction

In Chapter 2 we present a featured review article that provides thorough background for gold particle heating as well as the controversy behind the gold nanoparticle heating observations.[20] Briefly, there is no consensus on the heating mechanism of gold nanoparticles, if they heat at all, or whether they interact with the magnetic or electric component of RF fields. In the frequency range used, (13.56MHz -1

GHz) salt solutions heat as much or more than gold nanoparticles, confounding the interpretation of heating results.[20]

1.4 Magnetic particle background

The most commonly used magnetic nanoparticles, and the ones used in this work, are iron-oxide particles known as magnetite (Fe_3O_4). These particles are a mixed oxide composed of Fe(II) and Fe(III) in which the magnetic moments of the unpaired electrons in Fe(III) cancel out each other by aligning anti-parallel while the Fe(II) electron spins are aligned parallel.[18] This combination of parallel and anti-parallel ordering results in an overall magnetic moment,known as ferrimagnetism. When magnetite particles are smaller than 20 nm in diameter, they consist of a single magnetic domain.[19] These single domain ferro/ferrimagnetic particles are classified as superparamagnetic because in the absence of an externally applied field, they appear to have no intrinsic magnetism like simple paramagnetic materials.[11,19] The particles do have magnetic moments, but thermal energy is enough for the magnetic moment of the particle to spontaneously flip back and forth. Superparamagnetic particles are the ideal magnetic nanoparticles for biological applications because they do not undergo magnetic induced aggregation since the individual magnetic moments are constantly flipping back and forth.[11]

1.5 Superparamagnetic particle radiofrequency heating

Superparamagnetic particles heat in radiofrequency fields as the particle's magnetic moment chases the field.[11] Briefly, each time the field oscillates back and forth the magnetic moments of the particles are torqued and rotate to align with the field and minimize potential energy. If the field is oscillating faster than the particle can relax, or

re-orient its magnetic moment, then AC hysteresis occurs. Magnetic hysteresis is a phenomenon arising from remnant magnetization after an external field has been removed (Figure 1.1). Each oscillation results in net work being done on the particle, the excess energy is converted to heat. This heating theory was presented by Rosensweig[11] and is discussed in more detail in section 2.7.1.

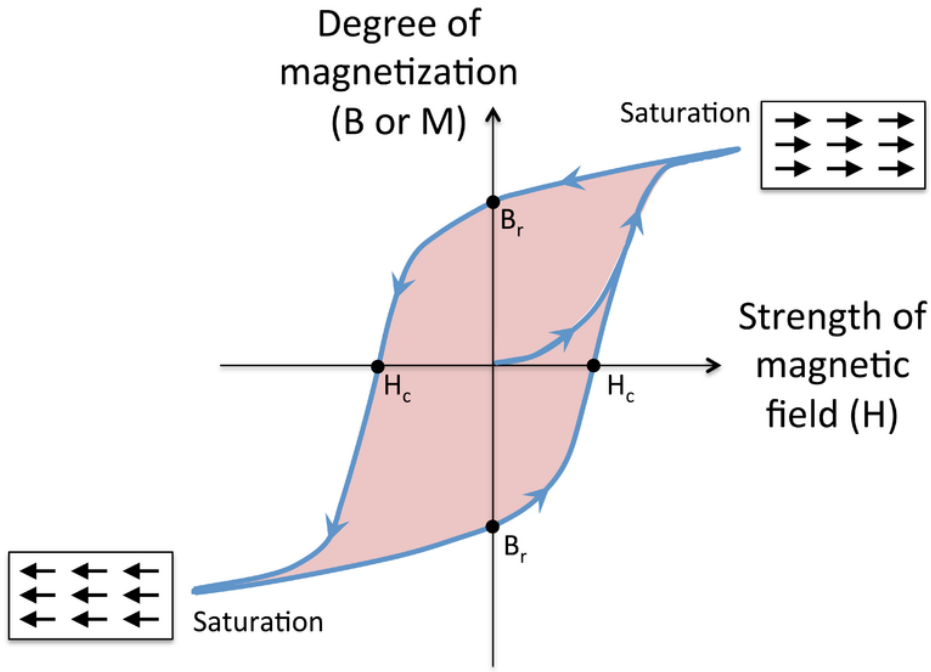

Figure 1.1 AC hysteresis curve. The area of the curve represents the net work done on the particle for each cycle of the field. Image from commons.wikipedia.org, 2014.

1.6 Local heating and enzyme activation

The central concept for local heating experiments is to generate regions of local heat in precise areas to induce a measurable effect without increasing the 'bulk' solution temperature of the surroundings. In 2002, the seminal report of gold heating in radiofrequency fields by Hamad-Schifferli introduced the idea of local heat generation.[12] They reported DNA hair pins attached to 1.4 nm gold nanoparticles melting when exposed to 1 GHz RF fields. This melting was attributed to increases in local temperatures in the immediate vicinity of the nanoparticles because the melting did not

occur in the absence of the gold nanoparticles. Despite claims of local heating, the temperature of the solution was never measured, so it's unclear if the bulk solution temperature increased. If the bulk solution temperature increased its unclear whether the nanoparticles or electrolytes added with the nanoparticles caused the temperature increase, which has been shown to be the case for multiple studies.[16,17,23]

Since this report more attempts have been made to use local heat from RF fields for remote drug delivery[9,24–26] and remote enzyme activation.[27] Remote enzyme activation is the use of nanoparticles to manipulate enzymes through the temperature dependence of enzymatic activity. The successful report of remote enzyme activation did not combine the remote activation and local heating concepts because the entire bulk surroundings were heating. Ideally, an enzyme could be activated remotely through the generation of local heat without disturbing or bulk heating the surroundings. This could potentially enable the remote control of certain cellular processes without harming or disrupting the rest of the cell.

1.7 Research approach

In Chapter 2 a feature review article is presented as a critical analysis of the gold heating literature along with experimental evidence supporting our conclusions made about the gold heating phenomenon.

- Collins, C. B.; McCoy, R. S.; Ackerson, B. J.; Collins, G. J.; Ackerson, C. J. Radiofrequency Heating Pathways for Gold Nanoparticles. *Nanoscale* **2014**, *6*, 8459–8472.

In Chapter 3 the first report of gold nanoparticle heating results that match calculated heating rates is presented. This was accomplished using atomically precise gold

nanoclusters and an electrophoretic heating mechanism. The theoretical calculations were made by measuring the screened charge of the particle, which is much lower than the predicted charge, as well as calculating the contribution of extant counter ions in solution.

- Collins, C. B.; Tofanelli, M. A.; Noblitt, S. D.; Ackerson, C. J. Electrophoretic Mechanism of $Au_{25}(SR)_{18}$ Heating in Radiofrequency Fields. *J. Phys. Chem. Lett.* **2018**, 1516–1521.

In Chapter 4 a study of the solution stability of organosoluble gold nanoclusters is presented to determine conditions in which gold nanoclusters should be stored for maximum solution stabilit, with large protecting ligands in nonpolar solvents.

- Collins, C. B.; Tofanelli, M. A.; Crook, M. F.; Phillips, B. D.; Ackerson, C. J. Practical Stability of $Au_{25}(SR)_{18}^{-1/0/+1}$. *RSC Adv.* **2017**, *7*, 45061–45065.

In Chapter 5, a study of gold coated iron-oxide nanoparticles, used to RF heat a covalently attached enzyme (thermolysin), is presented. In this work we are able to induce protease activity in bulk solution temperatures in which the enzyme is not normally active, successfully demonstrating the concept of remote activation of enzymes with local heat.

- Collins, C. B.; Ackerson, C. J. Radiofrequency Remote Control of Thermolysin. Manuscript in progress

1.8 Future of gold nanoparticle RF heating

We have successfully explained the observed heating trends of gold nanoparticles, but unfortunately these heating rates are very modest compared to salt ions with much larger charge to volume ratios. The exception to this may be ultra small

gold clusters such as Au_{25} because they can achieve a much higher charge to volume ratio than larger gold clusters/nanoparticles. These clusters have a higher charge to volume ratio and serve as an excellent model system for calculations due to their atomic precision. Unfortunately, the hydrodynamic diameter increases greatly resulting in a drastic decrease of the charge-to-volume ratio as soon as they are attached to a heating target, or coated with a protein corona. This reduces the large charge-to-volume ratio necessary for heating via an electrophoretic mechanism. Studies suggest superparamagnetic particles are much better suited for radiofrequency heating experiments, so we switched to using magnetite (Fe_3O_4) particles for enzyme activation experiments.

1.9 Future of remote enzyme activation

While we, and another group[28] have now successfully shown remote enzyme activation with local heat from nanoparticles, the activity increase is relatively modest compared to the optimal activity of the enzyme. We have reached the limit of our current heating system. But in the future, we can tune the heat production of the particle and distance between the particle and the enzyme target to increase the activity. With these advances we are getting closer to the enticing end goal of remotely controlling cellular processes as a noninvasive tool for learning about cellular processes without disrupting the rest of the cell.

REFERENCES

1. Gilchrist, R. K.; Medal, R.; Shorey, W. D.; Hanselman, R. C.; Parrott, J. C.; Taylor, C. B. Selective Inductive Heating of Lymph Nodes. *Ann. Surg.* **1957**, *146*, 596–606.

2. Bae, K. H.; Park, M.; Do, M. J.; Lee, N.; Ryu, J. H.; Kim, G. W.; Kim, C.; Park, T. G.; Hyeon, T. Chitosan Oligosaccharide-Stabilized Ferrimagnetic Iron Oxide Nanocubes for Magnetically Modulated Cancer Hyperthermia. *Acs Nano* **2012**, *6*, 5266–5273.

3. Beik, J.; Abed, Z.; Ghoreishi, F. S.; Hosseini-Nami, S.; Mehrzadi, S.; Shakeri-Zadeh, A.; Kamrava, S. K. Nanotechnology in Hyperthermia Cancer Therapy: From Fundamental Principles to Advanced Applications. *J. Controlled Release* **2016**, *235*, 205–221.

4. Espinosa, A.; Di Corato, R.; Kolosnjaj-Tabi, J.; Flaud, P.; Pellegrino, T.; Wilhelm, C. Duality of Iron Oxide Nanoparticles in Cancer Therapy: Amplification of Heating Efficiency by Magnetic Hyperthermia and Photothermal Bimodal Treatment. *ACS Nano* **2016**, *10*, 2436–2446.

5. Cristina Popescu, R.; Mihai Grumezescu, A. Magnetite Nanostructures with Applications in Cancer Therapy. *Curr. Proteomics* **2014**, *11*, 128–138.

6. Glazer, E. S.; Curley, S. A. The Ongoing History of Thermal Therapy for Cancer. *Surg. Oncol. Clin. N. Am.* **2011**, *20*, 229–235.

7. Kobayashi, T. Cancer Hyperthermia Using Magnetic Nanoparticles. *Biotechnol. J.* **2011**, *6*, 1342–1347.

8. Bonini, M.; Berti, D.; Baglioni, P. Nanostructures for Magnetically Triggered Release of Drugs and Biomolecules. *Curr. Opin. Colloid Interface Sci.* **2013**, *18*, 459–467.

9. Tietze, R.; Lyer, S.; Dürr, S.; Struffert, T.; Engelhorn, T.; Schwarz, M.; Eckert, E.; Göen, T.; Vasylyev, S.; Peukert, W.; et al. Efficient Drug-Delivery Using Magnetic Nanoparticles — Biodistribution and Therapeutic Effects in Tumour Bearing Rabbits. *Nanomedicine Nanotechnol. Biol. Med.* **2013**, *9*, 961–971.

10. Tietze, R.; Jurgons, R.; Lyer, S.; Schreiber, E.; Wiekhorst, F.; Eberbeck, D.; Richter, H.; Steinhoff, U.; Trahms, L.; Alexiou, C. Quantification of Drug-Loaded Magnetic Nanoparticles in Rabbit Liver and Tumor after in Vivo Administration. *J. Magn. Magn. Mater.* **2009**, *321*, 1465–1468.

11. Rosensweig, R. E. Heating Magnetic Fluid with Alternating Magnetic Field. *J. Magn. Magn. Mater.* **2002**, *252*, 370–374.

12. Hamad-Schifferli, K.; Schwartz, J. J.; Santos, A. T.; Zhang, S.; Jacobson, J. M. Remote Electronic Control of DNA Hybridization through Inductive Coupling to an Attached Metal Nanocrystal Antenna. *Nature* **2002**, *415*, 152–155.

13. Chen, H.-J.; Wen, D. Experimental Study of Electromagnetic Heating of Gold Nanoparticle Dispersions at 200 KHz. *Nanomed.* **2013**, *8*, 215–222.

14. Kruse, D. E.; Stephens, D. N.; Lindfors, H. A.; Ingham, E. S.; Paoli, E. E.; Ferrara, K. W. A Radio-Frequency Coupling Network for Heating of Citrate-Coated Gold Nanoparticles for Cancer Therapy: Design and Analysis. *IEEE Trans. Biomed. Eng.* **2011**, *58* (7), 2002–2012.

15. McCoy, R. S.; Choi, S.; Collins, G.; Ackerson, B. J.; Ackerson, C. J. Superatom Paramagnetism Enables Gold Nanocluster Heating in Applied Radiofrequency Fields. *ACS Nano* **2013**, *7*, 2610–2616.

16. Kim, H. K.; Hanson, G. W.; Geller, D. A. Are Gold Clusters in RF Fields Hot or Not? *Science* **2013**, *340*, 441–442.

17. Li, D.; Jung, Y. S.; Tan, S.; Kim, H. K.; Chory, E.; Geller, D. A. Negligible Absorption of Radiofrequency Radiation by Colloidal Gold Nanoparticles. *J. Colloid Interface Sci.* **2011**, *358*, 47–53.

18. Ferguson, R. M.; Khandhar, A. P.; Jonasson, C.; Blomgren, J.; Johansson, C.; Krishnan, K. M. Size-Dependent Relaxation Properties of Monodisperse Magnetite Nanoparticles Measured Over Seven Decades of Frequency by AC Susceptometry. *IEEE Trans. Magn.* **2013**, *49*, 3441–3444.

19. Dunlop, D. J. Superparamagnetic and Single-Domain Threshold Sizes in Magnetite. *J. Geophys. Res.* **1973**, *78*, 1780–1793.

20. Collins, C. B.; McCoy, R. S.; Ackerson, B. J.; Collins, G. J.; Ackerson, C. J. Radiofrequency Heating Pathways for Gold Nanoparticles. *Nanoscale* **2014**, *6*, 8459–8472.

21. Hanson, G. W.; Monreal, R. C.; Apell, S. P. Electromagnetic Absorption Mechanisms in Metal Nanospheres: Bulk and Surface Effects in Radiofrequency-Terahertz Heating of Nanoparticles. *J. Appl. Phys.* **2011**, *109*, 124306-124306–6.

22. Gupta, A.; Kane, R. S.; Borca-Tasciuc, D.-A. Local Temperature Measurement in the Vicinity of Electromagnetically Heated Magnetite and Gold Nanoparticles. *J. Appl. Phys.* **2010**, *108*, 064901.

23. Collins, C. B.; Tofanelli, M. A.; Noblitt, S. D.; Ackerson, C. J. Electrophoretic Mechanism of Au25(SR)18 Heating in Radiofrequency Fields. *J. Phys. Chem. Lett.* **2018**, 1516–1521.

24. Majeed, M. I.; Lu, Q.; Yan, W.; Li, Z.; Hussain, I.; Tahir, M. N.; Tremel, W.; Tan, B. Highly Water-Soluble Magnetic Iron Oxide (Fe3O4) Nanoparticles for Drug Delivery: Enhanced in Vitro Therapeutic Efficacy of Doxorubicin and MION Conjugates. *J. Mater. Chem. B* **2013**, *1*, 2874–2884.

25. Romero, G.; Christiansen, M. G.; Barbosa, L. S.; Garcia, F.; Anikeeva, P. Localized Excitation of Neural Activity via Rapid Magnetothermal Drug Release. *Adv. Funct. Mater.* **2016**, *26*, 6471–6478.

26. Tao, C.; Zhu, Y. Magnetic Mesoporous Silica Nanoparticles for Potential Delivery of Chemotherapeutic Drugs and Hyperthermia. *Dalton Trans.* **2014**, *43*, 15482–15490.

27. Knecht, L. D.; Ali, N.; Wei, Y.; Hilt, J. Z.; Daunert, S. Nanoparticle-Mediated Remote Control of Enzymatic Activity. *ACS Nano* **2012**, *6*, 9079–9086.

28. Suzuki, M.; Aki, A.; Mizuki, T.; Maekawa, T.; Usami, R.; Morimoto, H. Encouragement of Enzyme Reaction Utilizing Heat Generation from Ferromagnetic Particles Subjected to an AC Magnetic Field. *Plos One* **2015**, 10, 11.

CHAPTER 2: RADIOFREQUENCY HEATING PATHWAYS FOR GOLD NANOPARTICLES

2.1 Synopsis

While applications in biology motivated initial investigation of RF heating of gold nanoparticles, recent controversy concerning whether thermal effects can be attributed to nanoscopic gold highlight the need to understand the mechanism or mechanisms of heating. Both the nature of the particle and the nature of the RF field influence heating. Aspects of nanoparticle chemistry and physics, including the hydrodynamic diameter of the particle, the oxidation state and related magnetism of the core, and the chemical nature of the ligand shell may all strongly influence to what extent a nanoparticle heats in an RF. Aspects of RF include: power, frequency and antenna designs that emphasize relative strength of magnetic or electric fields, and influence the extent to which a gold nanoparticle heats in RF. These nanoparticle and RF properties are analyzed in the context of three heating mechanisms proposed to explain gold nanoparticle heating in RF. This article also makes a critical analysis of the existing literature in the context of the nanoparticle preparations, RF structure, and suggested mechanisms in previously reported experiments.

2.2 Introduction

The interaction of electromagnetic radiation with metal nanoparticles is presently explored for a wide range of applications, such as hyperthermal therapy,[1] catalysis,[2,3] biomedical contrast,[4,5] and waste treatment.[6] Nearly every region of the electromagnetic spectrum is examined (figure 2.1), with some spectral selectivity conferred by particle size and morphology.

The heating of metal nanoparticles in electromagnetic radiation is investigated with both infrared radiation and radio-frequency / microwave radiation. Nanoparticle-localized heat is used in the nascent field of remote-control biology.[7] Visible and infrared light can excite surface plasmon resonance in gold nanoparticles, provoking photothermal heating through well understood mechanisms.[8,9] In the case of radiofrequency and microwave irradiation of metal nanoparticles, mechanisms of heating are poorly understood. In fact, several reports question both experimentally[10-12] and theoretically[11,13] whether metal nanoparticles heat in RF or microwave radiation at all.

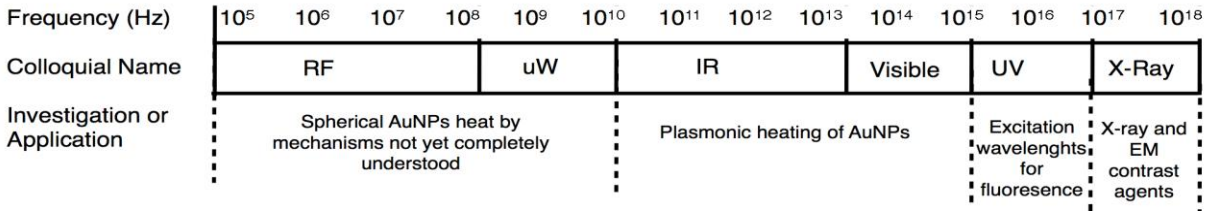

Figure 2.1. Nanoscopic gold and interactions with the electromagnetic spectrum.

Radiofrequency is especially desirable in many downstream applications because it penetrates through most non-conductive materials. This property is of course the basis for wireless communication.

Mechanistic insight may allow for more effective heating by revealing the effects of AuNP properties such as size, shape, oxidation state, and magnetic moment, as well as RF characteristics, including relative emphasis of electric (E-field) or magnetic (B-field), field strength, and chosen frequency.

The literature on heating of AuNPs with RF contains experiments with dramatically different RF and nanoparticle properties. In terms of nanoparticles, spherical diameters used range from 1.4nm to 100nm, a size regime over which size-dependent physical chemistry evolves markedly. In terms of RF, investigations include

RF that emphasizes E-field, RF that emphasizes B-field, and frequencies that range from kHz to GHz. While the higher frequencies used in this literature are technically microwave frequency, we will use RF as a shorthand in this review to encompass experiments done with both RF and microwave frequency radiation.

In this article we distil this complex and contradictory literature into a set of plausible heating mechanisms, and reinterpret much of the historical literature that invoked mechanisms that are now apparently discarded by researchers active in the field. We first make a brief overview of the history of the field, then review tunable RF field characteristics and AuNP properties. Then we synthesize this literature, presenting mechanisms and a unified set of mechanistic predictions in terms of particle size and RF nature. Finally, we present a critical analysis of the literature in which we reinterpret some older papers in terms of presently accepted mechanisms.

2.2.1 The History of AuNP Heating in RF Fields

Investigation of AuNP heating in RF initially proceeded along two independent lines of research, both of which initially emphasized biological application over mechanistic understanding. The earlier line of research aimed to thermally manipulate molecules with nano-localized heat.[14,15] The later line of research focused on hyperthermal therapy of cancer.[16,17] These two independent lines of research differed initially in two important aspects: first, in the size (and therefore underlying physical chemistry) of gold nanoparticle used, and second, in the nature of the radiofrequency used (in terms of power, frequency and antenna design.) A unified literature emerged recently, where attempts to integrate the phenomena across a wide range of experimental approaches are made.[11-13,18,19]

The first report of gold nanoparticles heating in a radiofrequency field came from a group led by a chemist in the MIT Media Lab. [14] In this landmark work, a 1.4nm diameter commercial Nanogold™ particle in a 0.4 W 1GHz solenoid generated radiofrequency *magnetic* (RFMF) field generated localized heat sufficient to melt a covalently attached stretch of hairpin DNA (whose melting temperature was ~35^{o}C) without, apparently, heating the surrounding solution (Figure 2.2). An inductive or Joule-type mechanism of heating, with some theoretical support, was postulated to explain the heat. The Joule-type heating arises from inductive coupling, from the applied magnetic field to the metal cluster. This results in creation of eddy currents in the metal cluster, via Faraday induction. The phenomenon is well understood for macroscopic systems, such as transformer or inductor core materials.

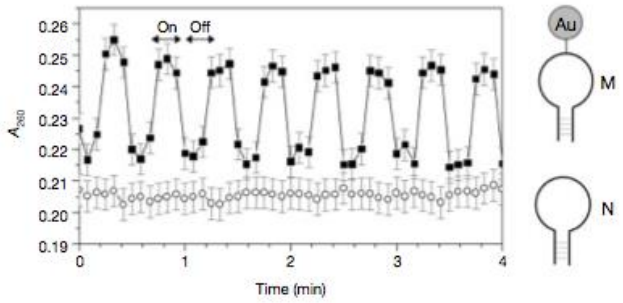

Figure 2.2. Absorbance at 260 nm (e260) of a solution of M in RFMF (squares). Arrows indicate when the RFMF is on/off. Circles, response of N (no nanocrystals) in RFMF. Gold nanocrystals also show an absorbance increase under RFMF, qualitatively attributed to the change in the optical absorption due to eddy currents. However, the absorbance increases nearly uniformly over 200±300 nm with RFMF and is small relative to the oligo change in absorbance. Reproduced from reference 14.

Experimental follow ups by the authors of this paper are minimal.[20] Other direct experimental follow ups that cited this initial report used substantially different experimental conditions,[15,21,22] as discussed below.

In a set of studies that did not cite initial study of RF interacting with nanoparticles,[16,17,23] groups lead by surgeons began investigating the heating of nanomaterials including metal nanoparticles under RF irradiation for the destruction of cancer. RF ablation is used in clinical practice to treat tumors, and academic surgeons familiar with the technique began publishing experiments on the thermal properties of gold nanoparticles in the presence of RF irradiated cells.[16,17,23] These initial papers focused on killing cancer cells in cell culture and animal cancer models and made use of the so-called "Kanzius Machine" (Therm-Med LLC, Erie, PA).[24] The Kanzius Machine generates a capacitively coupled radiofrequency *electric* field at 13.56 MHz, and is generally operated at higher power output (up to 1000W.) Figure 2.3 shows an example of the destruction of cultured model cancer cells with RF irradiated gold nanoparticles in the first paper reporting this method. All experiments so far reported with the Kanzius machine utilize AuNPs in the 5 – 100 nm diameter regime. While initial reports did not make in-depth investigation of the mechanism for AuNP heating, a subsequent report postulated a Joule-type mechanism of heating,[25] similar to the mechanism suggested in the original report of Hamad-Schifferli.[14]

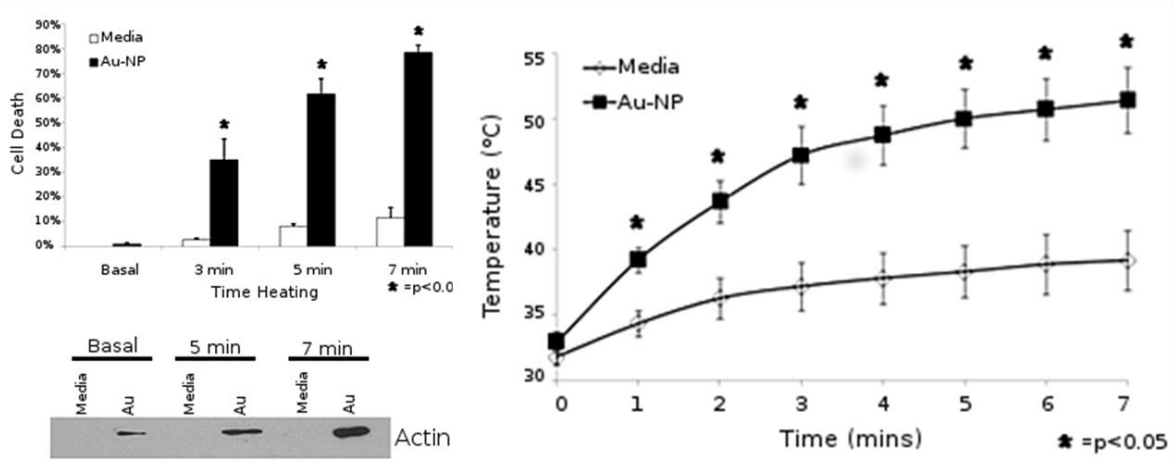

Figure 2.3. In vitro cell culture demonstrates effective heating and cell death with Au-NP treated cells in the RF field. A, Temperature of HepG2 cells exposed to 35 W in the RF field in the presence (squares) or absence (diamonds) of Au-NP over a time course. Results reported are the average of 3 separate experiments. B, Percent cell death as assessed by LDH assay of HepG2 cells exposed to 35 W in the RF field for 3, 5 or 7 minutes in the presence (black) or absence (white) of Au-NP. Results reported are the average of 3 separate experiments. C, Western blot for b-actin on the supernatants of HepG2 cells exposed to 35 W in the RF field in the presence or absence of Au- NP for 5 or 7 minutes. Reproduced with permission from reference 16.

Most successive reports of AuNP heating in RF build directly on either the Hamad-Schifferli report[14] or use the Kanzius machine. Although a unified literature that attempts to rationalize both experimental starting points has emerged, we suggest (*vide infra*) that these are potentially different experiments. Technically, they differ in both the nature of the RF and the nature of the gold nanoparticles used. In terms of RF, they are using different RF antenna designs, dramatically different frequencies, and markedly different applied power. These lines of research also use different sizes of inorganic gold nanoparticles. All of these experimental modifications may be important in the interpretation of the work (*vide infra*). Despite all these differences in experimental setup, Joule-type nanoparticle heating was proposed in each case.

The validity of Joule-type heating of metal nanoparticles in RF is questioned on both experimental[10-12,26] and theoretical[13] grounds. One study attributes the observed

heating to Joule-type heating not of nanoparticles, but of surrounding electrolytes, based on the observation that when particles are dissolved in rigorously deionized water, little to no heat is observed.[12] Other experimental studies conclude that the amount of nanoparticle-attributed thermal dissipation reported could not be reproduced.[10,11,26] Theoretically, Joule-heating is difficult to reconcile with nanoparticles of the size used in these experiments.[13]

Two novel mechanisms for nanoparticle heating in RF emerged after the reports disputing the possibility of Joule-type heating. Two groups show both experimentally and theoretically that an electrophoretic mechanism can account for heat attributable to nanoparticles.[27,28] This mechanism becomes prominent when for nanoparticles 10nm in diameter or smaller.[27] We also recently found that an unexpected magnetic mechanism can account for heating of sub 2 nanometer diameter nanoparticles.[19] Furthermore, the question of the role of salts in heating is complicated by recent reports. Some reports suggest that dissolved salts *enhance* the heat that is attributable to nanoparticles.[19,28,29] In addition, a recent report highlighted that the shape of a vessel that holds the nanoparticles in an RF field is a critical and previously unrecognized component in whether heat attributable to particles is observed.[30] The interest and importance of some of these previously unrecognized experimental aspects was highlighted in a *Science* perspective.[18]

Thus, the history of gold nanoparticles heating in RF is one in which technically quite different experiments produced results that were attributed to the same underlying phenomenon—joule heating. Today, Joule heating as a mechanism for heating is essentially dismissed, even by research groups that previously attributed their heating

to that mechanism.[27] It is now also questionable whether any spherical AuNP larger than 10nm does heat in RF. As a not-very-unified field of inquiry, current interest lies in deciphering which mechanisms produce heating under different experimental conditions, as well as elucidating the role of salt solutions.

The area of study, as it has emerged, is highly interdisciplinary, with groups lead by disciplinary chemists, [19,20] surgeons,[16,17] electrical engineers,[31] and physicists[10] all making contributions, often in multidisciplinary teams. Straightforward comparison of results reported by different groups is confounded by different RF properties, different particle formulations, and different reporting rubrics for disclosing how much heat dissipation is attributable to nanoparticles.

To enable a critical analysis of the heating of metal nanoparticles in RF, we review nanoparticle structure and RF, focusing especially on the aspects of nanoparticle structure that may contribute to heating in RF. Following this introduction to the components in the system, we will summarize each of the mechanisms hypothesized to date that contribute to heating. After reviewing these components of the phenomenon, we make a critical analysis of the field as it stands and its prospects in the future.

2.3 The Mystery of Hot Gold Nanoparticles in RF

A debate is open regarding whether gold nanoparticles heat in an RF at all, and if AuNPs do heat in an RF, what is the mechanism? There are three mechanisms proposed in the current literature: Joule or inductive heating, magnetic heating and electrophoretic heating. Each mechanism has a strong dependence on the frequency of the applied RF and the diameter of the nanoparticle. Which mechanisms dominate

heating may depend on the exact experimental setup, with parameters of the RF field character and nanoparticle formulation both playing a role.

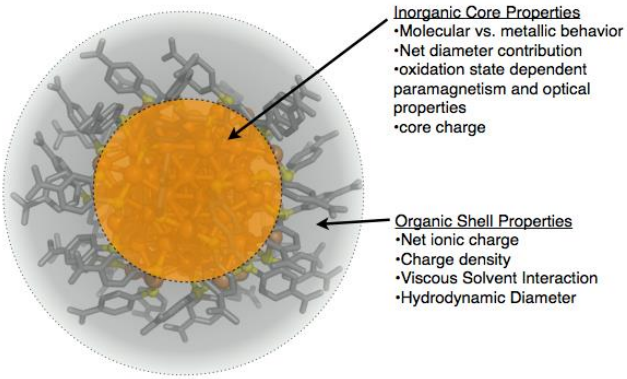

Figure 2.4. Illustration of the core and organic ligand shell of $Au_{102}(SR)_{44}$ nanocluster. The properties that are enumerated as belonging to the core or the ligand shell are generalizable to other sizes. Each of the enumerated properties may affect heating under one or more of the mechanistic considerations.

2.4 Physical Properties of Gold Nanoparticles

The early literature on RF heating of AuNPs assumes that very small pieces of gold (with diameters between 1 – 100 nm) behave as bulk gold.[14,25] This possibly erroneous assumption motivated the original hypotheses of induction heating. Research on the size-dependent physical properties of AuNPs reveals profound physical insights into the size and morphology dependent evolution of physical properties. In the 1-3 nm diameter size range, even the exact number of gold atoms and electrons strongly effects stability,[32-34] electronic and optical properties,[35-37] and magnetism.[38,39]

Many of these properties, including molecular vs metallic behavior, magnetic behavior and net charge may strongly influence interactions with RF. To fully account for gold nanoparticle interaction with RF fields, we enumerate the properties of nanoscopic gold that may allow interaction with the RF field under each mechanistic consideration. Figure 2.4 shows the chemical construction of a gold nanoparticle as an

inorganic core and a ligand shell. As we will show below, the nature of both the organic and inorganic parts play a role in the mechanism of gold nanoparticle heating in RF.

Structure. All of the AuNPs used in RF interaction studies are protected by an organic shell, which stabilizes the AuNPs against aggregation and sintering and solubilizes AuNPs in solvents. The organic ligands that stabilize the clusters used in reported studies are organophosphines, organothiolates, citrate, or proprietary commercial ligands of unknown composition. These ligands are generally present early in the synthesis and both control the size of the resulting particle and stabilize the particle against reversible or irreversible aggregation and sintering.

Ligand Shell. The ligand shell encodes two properties of potential importance for RF heating mechanisms: charge and thickness. Water-soluble AuNPs used universally in RF studies so far have carboxylic acid terminated ligand shells, conveying (ionic) charge and charge density to AuNPs. The interaction of this negatively charged ligand shell with RF is suggested as important in electrophoretic heating.[27,28] The other property of the ligand shell of potential importance is the “monolayer thickness” of the ligand shell, which plays a key role in the electrochemical properties of clusters,[35,37,40] as well as influencing hydrodynamic diameter. As discussed below, electrochemical properties and paramagnetism are tightly linked.

Inorganic Core. The range of sizes of spherical AuNPs that are studied for RF heating lie on the ‘molecular to metallic continuum’, meaning that the physical chemistry of the smaller particles tested for RF heating is very different than that of the larger particles tested for RF heating. The particle size at which transition from molecular-to-bulk or metallic like behavior is not discrete, and depends on which properties are considered.

Properties that evolve dramatically in this size regime include electrochemical,[35] optical (notably plasmon emergence) and collapse of the HOMO-LUMO gap,[41] and mechanism of stabilization.[32]

Mechanism of stabilization for metal nanoclusters is understood as either electronic or geometric, where electronic stabilization is favored for smaller nanoclusters and geometric stabilization for larger.[34] In the case of ligand protected gold, $Au_{11}(PPh_3)_7Cl_3$, $Au_{25}(SR)_{38}$, $Au_{38}(SR)_{24}$, $Au_{39}(PPh)_{14}Cl_6^-$, $Au_{102}(SR)_{44}$ among others are understood as electronically stabilized, as substantiated by generally low symmetry and conformance to electron counting rules.[32] For the larger clusters $Au_{144}(SR)_{60}$, $Au_{333}(SR)_{\sim 80}$ and $Au_{\sim 530}(SR)_{\sim 100}$, [42-44] structures are not yet available and the role of superatom orbitals is not fully defined. For instance, in the case of Au_{144} and Au_{333}, geometrically perfect models are proposed,[42,44] and yet evidence in each case for presence of superatom-type orbitals persists. [42,45]

Electronically Stabilized (Superatom) Nanoclusters. The 'superatom' concept is useful in explaining both what is meant by 'electronic stabilization' as well as some of the stability, reactivity, and *magnetic* properties of electronically stabilized clusters. To make the simplest explanation of the superatom concept, recall that the total filling of electron shells in atoms results in the well-known noble gas stability. Thus, the total filling of 1s | 2s 2p | 3s 3p | 3d 4s 4p| electron shells implies a 'magic number of electrons' for noble-gas-like stability of 2, 10, 18, 36, … For metal clusters in the gas phase, which may be in the simplest case considered as a collection of positive charged nuclei in an approximately spherical shape, interacting with electrons, the accepted (simple) treatment is the Schrodinger equation solved for a spherically symmetric

square-well potential. This gives the electron orbitals 1S | 1P | 1D | 2S | 1F | 2P 1G | etc, giving magic numbers of electrons of 2, 8, 18, 20, 34, 40, 58, to arrive at clusters of special stability.[32,34,46]

Superatom stabilization concepts were first adapted for gold nanoclusters (ligated by phosphines and thiolates) in 2008, following the crystal structure of Au_{102}-SR_{44}.[32,47] The atomic structures enabled DFT calculations that showed that the relatively simple predictions of the superatom model are confirmed by all-electron DFT calculations which reveal that the frontier orbitals of $Au_{102}(SR)_{44}$, $Au_{39}(PR_3)_{14}X_6^-$, $Au_{13}(PR_3)_{10}X_2^{3+}$, and $Au_{11}(PR_3)_7X_3$ have dominant angular momentum character and degeneracy predicted by simple application of the superatom theory. Later work showed the success of superatom theory in predicting the stability of other crystallographically resolved gold clusters.[48-50]

So far, superatom theory is used primarily to explain the special stability of apparently stable clusters, as resulting from a noble-gas-like superatom electron configuration. The effects of 'open shell' electron configurations are only recently beginning to be investigated explicitly. The "superatom electron configuration" of a gold nanocluster can be modified through well-established electrochemical methods.[33,35] These modifications can influence magnetism of AuNPs.

Larger Nanoparticles. The practical preparation of well defined (in terms of molecular formula and atomistic structure) nanoparticles larger than $Au_{\sim 530}(SR)_{\sim 100}$ (approximately 2.5 nm inorganic diameter) is the current frontier of research. There is some debate about the isolability of exactly defined particles larger than the currently identified upper limit, as the energetic differences between 'highly stable' numbers of atoms and less

stable numbers of atoms become small. In this 'metallic materials regime' the inorganic portion of nanoparticles are characterized in terms of size (usually diameter for spherical particles) and dispersity, where a commonly used definition of 'monodisperse' allows for 10% standard deviation in a collection of particle diameter measurements. There is little evidence for superatomic orbitals in particles larger than 2.5nm diameter. Such electronic structure is now well established for particles 1.5nm in inorganic diameter (i.e., $Au_{102}(SR)_{44}$) and smaller.

2.5 Magnetism in Gold Nanoparticles

Magnetism in AuNPs is of importance for AuNP heating in RF, since the magnetic moments of the cluster may interact with the magnetic portion of the applied RF field to produce heat. However, magnetism in gold nanoparticles is poorly understood, with the literature rife with results that are not repeatable across other labs or even within the same lab, as highlighted in a recent review.[38]

The oxidation state dependence of paramagnetism, however, is increasingly well established in the case of $Au_{25}(SR)_{18}$. In this case, the majority of magnetism measured can be attributed to the superatom nature of these small clusters.

From a superatom perspective, $Au_{25}(SR)_{18}^{-}$, which is the most stable redox state of the cluster,[32,33] is an $8e^{-}$ system, corresponding to the total filling of the 1S and 1P superatom orbitals. Multiple reports now use EPR, SQUID and redox chemistry to compare the anionic and neutral forms of $Au_{25}(SR)_{18}^{x}$ (where x= -1, 0 and +1) and these reports conclude universally that the anion is diamagnetic and the neutral compound paramagnetic.[39,51,52] This is consistent with the superatom-theory-predicted doublet state.

The picture is somewhat murky for the $Au_{25}(SR)_{18}^{+}$ cluster. Naïve superatom theory predicts a triplet spin state for the $Au_{25}(SR)_{18}^{+}$ compound, but the cluster may also distort to adopt an singlet state. Experimentally both paramagnetic and diamagnetic $Au_{25}(SR)_{18}^{+}$ have been reported.[52,53] Thus, it is not perfectly clear if the assumptions of naïve superatom theory hold with regard to spin multiplicity of highly oxidized species. Our results for Au_{102} suggest the latter possibility, namely that spin multiplicity of superatoms might increase until the orbital is ½ filled.[19] However, this area of research is not settled science. The role of the ligand shell in enforcing core symmetry, underlying flexibility of the gold core allowing Jahn-Teller like distortions, and instability of clusters charged to large charge states may all contribute to the effect of oxidation on magnetism.

2.6 Radio Frequency Field Background

RF is nominally electromagnetic radiation with frequencies between 1/2 MHz to 500 MHz. Above 500 MHz frequency is the beginning of the microwave region. The behavior of macroscopic pieces of metal (conductors) in RF circuits acting as loads is well understood and can be robustly modeled. But parasitic elements must be incorporated in models to account for capacitive coupling. Nevertheless, there remains, a substantial element of ‘art’ in RF circuit modelling. In short, quantitative models vary with metal cluster environments and changing parasitic components in the RF model of the loads circuit.

Three primary characteristics of an RF field determine the thermal dissipation of a ‘piece of metal’ in the near field: (1) The applied frequency of the RF fields (usually

reported in Hz); (2) The magnetic or electric emphasis of the field (determined by the inductive or capacitive antenna design), and (3) the maximum power of the RF field.

The behavior of nanoscopic pieces of metal in both near fields (where RF B fields dominate) and far RF fields (where B and E fields both play roles) remains poorly understood. There is presently not sufficient data in the literature to enable improved understanding. We aim to address by calorimetric means of quantifying heat adsorption versus location from the antenna and from frequency variations of the RF field. The present literature contains sparse systematic investigation of field composition (B- vs E-) and gleaned not from a single report but by comparing multiple reports. The effect of RF frequency on thermal dissipation is studied theoretically,[13,27] but there are no experimental reports of frequency dependence effects.

2.7 Mechanisms that Contribute to AuNP Heating in RF

There are three mechanisms discussed in the literature for heating of AuNPs in RF. Here we review each mechanism, and how it quantitatively interacts with the particles. We also synthesize a comparison of how the expected thermal dissipation of each heating mechanism pathway changes as either frequency or particle size change.

2.7.1 Magnetic Heating

Magnetic heating is relevant in the case of gold nanoparticles because tailored gold nanoparticles can be magnetic.[19,38,39] For the magnetic moment of a nanocluster to interact with an external alternating magnetic field to produce heat, two mechanisms may be considered. One mechanism, Brownian or viscous heating, assumes that the entire magnetic particle rotates to follow the directed and time varying alternating magnetic field (RFMF).[54] The resulting viscous friction between the particle and the

supporting solvent manifests as heat. The other mechanism considered, Néel relaxation,[55,56] occurs in media where the magnetic moment of the particle realigning with the magnetic field occurs without the particle rotating. Both mechanisms produce heat, but the fastest mechanism of relaxation dominates.[54]

The Brownian power dissipation (P) of a suspension of magnetic particles rotating in response to a magnetic field depends on several experimental variables. These include the size or volume of the individual particles, the concentration of the particles in solution (i.e., volume fraction), how magnetic the particles are, the magnitude of the magnetic field, the viscosity of the solvent, and the frequency of the RF.

The interaction of each of these experimental variables as they relate to power absorption (and subsequent generation of heat) was quantified theoretically by Rosensweig in the following equation[54]:

$$P = \frac{\phi M_d B}{2}\left(coth[\xi] - \frac{1}{\xi}\right)\frac{\omega^2\tau}{1+(\omega\tau)^2} \quad (2.1)$$

where $\xi = \frac{M_d BV}{k_B T}$ and $\tau = \frac{3\eta V}{k_B T}$. Here V is the particle volume, M_d the particle magnetization, η the dynamic shear viscosity of the solvent, $k_B T$ is the thermal energy, B is the magnetic field, φ is the volume fraction of the particles, and ω is the angular frequency which depends on the frequency of applied RF.

In contrast to Brownian dissipation of power, Néel dissipation does not depend on solvent viscosity, since Néel relaxation occurs in a stationary particle. The Néel relaxation times depend on the ability of the magnetic moment of the particle to rotate within a fixed particle. These times are described by the following equation:

$$\tau_N = \tau_0 e^{\left(\frac{KV}{k_b T}\right)} \quad (2.2)$$

Where τ_0 is the attempt time (~10^{-9} s), K is the anisotropy energy density and V is the magnetic volume.[54] Here the magnetic volume is used because it's assumed that the majority of the magnetic response comes from the core with little contribution from the presumably diamagnetic ligands.

Since the Brownian and Néel relaxation processes happen in parallel, Néel relaxations can be included in equation (1) by taking the harmonic average of the two relaxation times: [54]

$$\frac{1}{\tau} = \frac{1}{\tau_N} + \frac{1}{\tau_B} \quad (2.3)$$

This gives a better approximation of heating rates from equation (2.1), but also requires more involved calculations with approximations of the size-dependent anisotropy constant, and the attempt time. Therefore, we do not include Néel relaxations in our current models.

The fact that the relaxation mechanisms depend on different factors may allow for investigation of the heat produced by changing the relaxation times. The viscosity of the solvent is varied by changing the Brownian relaxation time. Many studies investigating the relationships between the relaxation times and heat generation for macroscopic size superparamagnetic iron-oxide particles have been conducted over the past few decades.[57] We can tailor the Brownian relaxation time of our nanosize particles by changing the ligand coating, which impacts the hydrodynamic volume. The Néel relaxation times are more difficult to change without also changing the Brownian times.

2.7.2 Electrophoretic Heating

Most soluble AuNPs incorporate a net ionic charge, which depends on both the charge of the inorganic core and the charge of the ligands that passivate the particles against sintering. Commercially produced and water-soluble laboratory syntheses generally produce particles with a net negative charge. Charged particles migrate in an applied electric field toward their complementary charge. In an alternating electric field, charged particles will follow the alternating electric field. The absorption of power because of this electrophoretic movement is described by the dielectric constant. The dielectric constant has real and imaginary components, with the imaginary component containing any variables affected by experimental parameters. The imaginary component corresponding to the power loss is quantified by Sassaroli[28]:

$$P = \frac{\phi}{\frac{4\pi}{3}a^3}\frac{E^2q^2}{\beta}\left(\frac{1}{1+\delta^2\omega^2}\right) \tag{2.4}$$

Where $\delta = \frac{2\rho a^2}{3\eta}$ and $\beta = 6\pi\eta a$. Here q is the particle charge, η the dynamic shear viscosity of the solvent, E is the electric field strength, ρ is the particle density, φ is the volume fraction of the particles, and a is the radius of the particle. As in magnetic heating, this mechanism depends on variables that we can test experimentally, including AuNP net charge, AuNP particle density, AuNP volume fraction (modifiable through size of ligand shell), and frequency.

2.7.3 Inductive (or Joule) Heating

Several early papers attribute gold nanoparticle heating in RF to Joule-type or inductive mechanisms.[14,15,25]. However, the tiny area that nanoclusters present to the applied magnetic field attenuates such eddy current effects.

The frequency dependence of inductive power absorption by a suspension of conductive spheres is given by Smythe[58]:

$$P = \frac{\varphi}{\frac{4\pi a^3}{3}} \frac{\left(\frac{6\pi a B^2 \tau^4}{\sigma {\mu_o}^2}\left(-cos[\sqrt{2}\tau] + cosh[\sqrt{2}\tau] - \frac{\tau}{\sqrt{2}}(sin[\sqrt{2}\tau] + sinh[\sqrt{2}\tau])\right)\right)}{\left((\tau^4 + \chi^2 - \tau^2\chi^2)cos[\sqrt{2}\tau] - (\tau^4 + \chi^2 + \tau^2\chi^2)cosh[\sqrt{2}\tau] + \sqrt{2}\tau\chi\left((\tau^2 + \chi)sin[\sqrt{2}\tau] + (-\tau^2 + \chi)sinh[\sqrt{2}\tau]\right)\right)} \quad (2.5)$$

where $\tau = a\sqrt{\mu\sigma\omega}$ and $\chi = \frac{\mu}{\mu_o} - 1$. Here a is the particle diameter, σ the particle conductivity, μ the particle permeability, μ_0 the permeability of the solvent, ω the angular frequency, Φ the particle volume fraction and B the magnetic field strength. As highlighted by Hanson[13] and Sassaroli[28], we also calculate that direct inductive heating proves much too small to rationalize the thermal dissipation for the size of particles used in the literature, even when plasmon and surface roughness are considered.

2.7.4 Comparative Modeling of Potential Heating Mechanisms

The main goal of the modeling exercise was to determine if different heating mechanisms should be experimentally distinguishable. To compare how the heating rate that results from each considered mechanism changes as a function of experimental parameters, we modeled the mechanistic dependencies on both nanoparticle size and frequency of RF (f_{RF}). We used Mathematica to model the expected heating rate of each mechanism based on equations 2.1, 2.4 and 2.5 above. Due to the magnitude of this modeling exercise, we made some simplifications that are not perfectly realistic in the experimental case, as detailed below. We also did not include Néel relaxation (equation 2.2) in the present exercise, although it is almost certainly important.

Figure 2.5 shows expected heating rate as a function of particle radius for the three mechanisms represented by equations 2.1, 2.4 and 2.5. The Y axis of heating rate is given as units of power (Watts) normalized by B^2, m^3 and Φ. This normalization is necessary so that heating rates can be compared without imposing explicit B-field and volume fraction values.

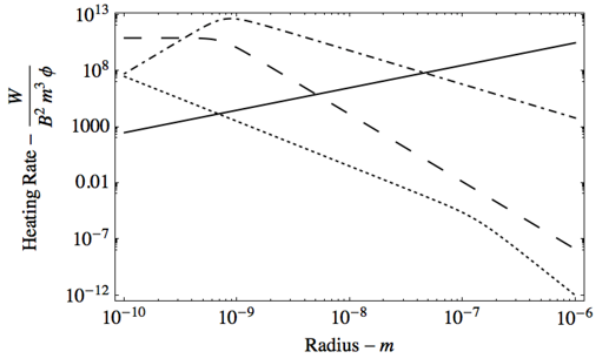

Figure 2.5. The plots of predicted heating in $\frac{W}{B^2 m^3 \phi}$ vs particle radius (in meters) at 13.56 MHz for induction (solid line, equation (2.5)), superatom (large dash, magnetic heating from equation (2.1)), ferromagnetic (dash-dot, magnetic heating from equation (2.1)) particles, and electrophoretic (dot, from equation (2.4)). The electrophoretic dissipation is normalized by f E^2 and scaled to fit on this.

The heating dependencies in this figure are varied only with AuNP diameter. Thus, the falloff in heat dissipation for the electrophoretic and magnetic mechanisms is accounted for partially by the effective dilution of a fixed amount of charge or unpaired spin over a larger and larger volume. Figure 2.6 shows the expected heating rate as a function of the f_{RF} for the three mechanisms represented by equations 2.1, 2.4 and 2.5. The Y axis in figure 2.6 is the same as in figure 2.5. For the inductive mechanism that drove initial work[14,25] heat varies with f_{RF} squared. In the electrophoretic mechanism[27,28] heating saturates and then falls off with varying f_{RF}. In the Brownian relaxation

(magnetic) mechanism highlighted in our recent work[19], we model a sublinear dependence on f_{RF}.

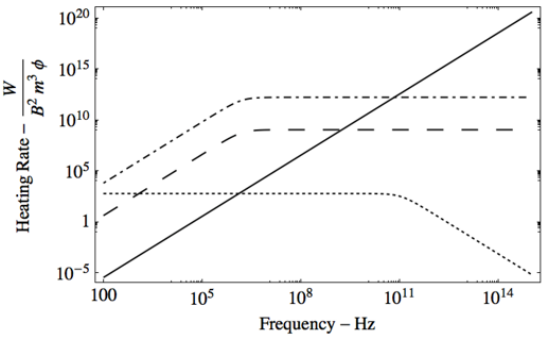

Figure 2.6. The plots of heating in $\frac{W}{B^2 m^3 \phi}$ vs frequency in Hz for 1.5 nm gold particles for induction (solid line, equation (2.5)), superatom (large dash, magnetic heating from equation (2.1)), ferromagnetic (dash-dot, magnetic heating equation (2.1)) particles, and electrophoretic (dot, from equation (2.4)). The simple electrophoretic model shows the effect of inertia reducing the loss at high frequency.

In figures 2.5 and 2.6 we considered two cases for the magnetic heating of equation (2.1) The heating of a 'superatom' and the heating of an ultra-small paramagnetic iron oxide (USPIO) of the same radius. The 'superatom' heating assumes the best-possible case for a superatom—that of a ½ filled G orbital in $Au_{102}(SR)_{44}$, giving 9 unpaired electrons. An USPIO of the same radius has less magnetization- and therefore typically less magnetic heating-- because the electron spins in magnetic iron oxides smaller than 3nm are typically not well ordered.[59]

Thus, the mechanisms should be experimentally distinguishable, and we expect that a unified picture of AuNP heating in RF may emerge that combines contributions from each mechanism or perhaps presently unconsidered mechanisms. To our knowledge, figures 2.5 and 2.6 contain the first simultaneous examination of frequency and nanoparticle size dependence of these mechanisms.

2.8 Heating of Salt Solutions

Joule-type heating of saline solutions is well known to occur. In this literature, it is shown that multiple antenna designs are capable of heating simple saline solutions at 13.56MHz, [12,19] presumably through Joule-type heating. Some reports that dismiss RF heating of AuNPs, suggest that all of heating previously attributed to gold nanoparticles can instead be attributed to joule-type heating of saline.[12,13]

The role of salts in particle heating may be the most unresolved aspect of thermal dissipation by gold nanoparticles in RF. Given the presence of relatively high concentrations of dissolved salts in biological tissues, and the interest in using this approach in biological systems, elucidating the role of dissolved salts in RF heating with and without nanoparticles is of high importance.

To date, biological applications drive the majority of research into RF heating of gold nanoclusters. In these applications a complex background that necessarily contains salts is present. Understanding of how that complex background affects salt-based heating is a missing link in this literature.

Other investigations suggest experimentally or theoretically that dissolved salts enhance heat transfer from the RF field to the gold nanoparticles.[19,28,29]. One study assesses several mechanisms of heating and concludes that most likely heat generation is due to concentration of the electric field at the surface of a nanoparticle.[29] Therefore, the removal of ions and thus the conducting medium diminishes this mechanism. We also previously suggested a cooperative effect between saline and nanoparticles. Specifically, we observed upon exposure to RF, solutions of

nanoparticles + salt produce notably more heat than either species alone.[19] A study of electrophoretic heating mechanisms also supports cooperative effects for salts.[28]

In salt-containing systems more complex than saline solutions, several reports show nanoparticle dependent tumor treatment in a complex biological background. [16,60] Background heating of physiological saline is not noted and would be catastrophic if it occurred.

We show here explicitly that the heating of salts in setups that minimize ion-mobility, such as biological tissues may be minimal, even while the heating of salts in simple saline solutions is significant. We show this for both a large molecule (a dendrimer), and a biological tissue model.

PAMAM dendrimers are large simple molecules with a number of carboxylic acid groups that doubles with each "generation."[61] We hypothesized that we could interrogate the effect of free ions in this system by comparing the response of equivalent number of ions as either "free" simple ions or large polyionic molecules. In our experiments, we used a generation 3 dendrimer with $2^{3+2} = 32$ carboxylic acid functional groups and a molecular weight of 6909 g/mol. When dissolved at a concentration of 140 µM, the concentration of ions is equivalent to free ions at 4.4 mM. We compared the heating response of such a 140 µM solution of a generation 3 PAMAM dendrimer (dialyzed against NH_4OH) to the heating of a 4.4 mM solution of NH_4OH. The results of this comparison are shown in Figure 2.7. The macromolecular nature of the counter ion in the dendrimer appears to substantially suppress heating compared to the 'free ion' case. We showed similar heating of 'free ions' in a previous

report.[19] This suggests that the ions must be freely diffusing in order to contribute maximally to salt based heating.

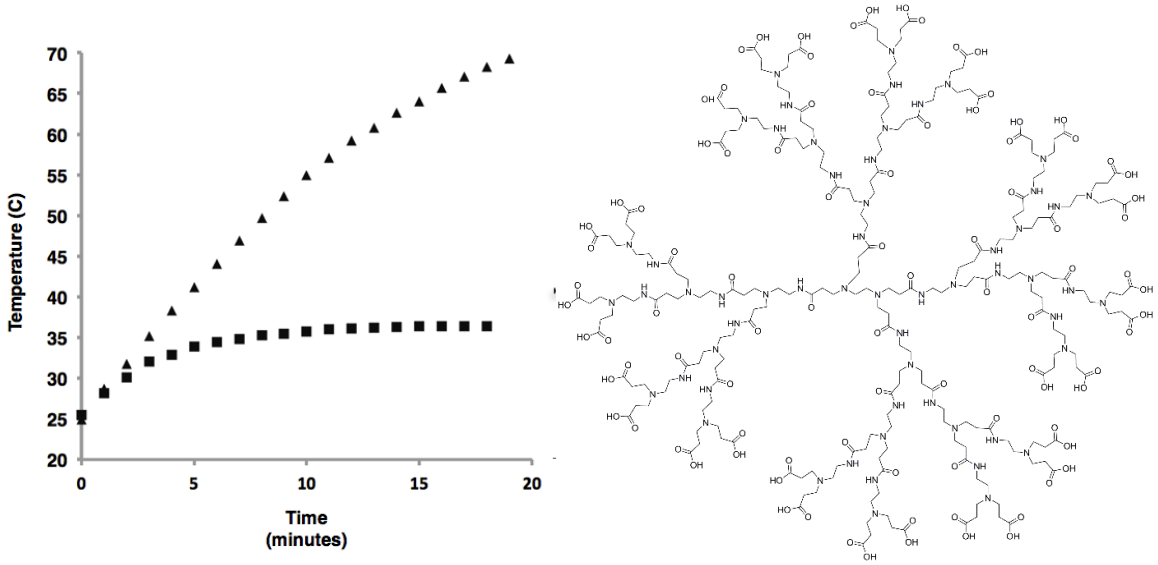

Figure 2.7. Left panel shows the time dependent thermal response of a solution containing PAMAM dendrimer (squares) and another solution containing an equivalent number of ammonium hydroxide ions (triangles). In the PAMAN solution the dendrimer concentration is 140 µM, thus the concentration of carboxylic acid groups is 4.4 mM and in the other solution total concentration of free ammonium ions is 4.4 mM. The heating of this solution is compared to the heating of a 4.4 mM solution of ammonium hydroxide. The right panel shows a Lewis diagram of the dendrimer used in this experiment.

The PAMAM dendrimer adds only a small amount of complexity to the system compared to a simple salt solution. Tissues are inordinately more complex than the PAMAM dendrimer, yet contain physiological amounts of salt. Food based models, such as chicken breast, are sometimes used as an inexpensive model of tissues.[62] Figure 2.8 shows the time-dependent heating response of chicken breast in a 13.56 MHz 50 W solenoid generated B-field. This piece of complex tissue, which contains ~150 mM NaCl, shows no apparent thermal dissipation. We showed earlier that oxidation of $Au_{102}(SR)_{44}$ substantially increases thermal dissipation for this compound.

Figure 2.8 shows that the effect is preserved even in the complex matrix of biological tissue.

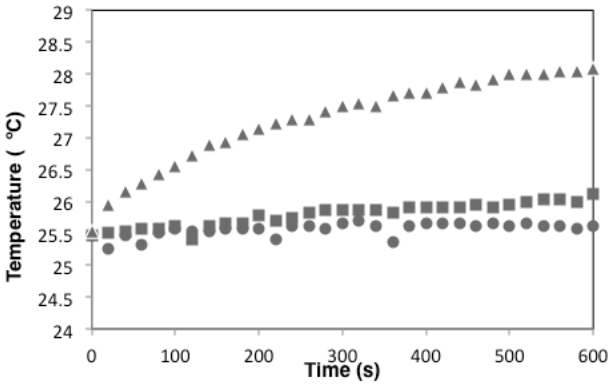

Figure 2.8. Samples of chicken muscle exposed to RF before soaking in $Au_{102}(SR)_{44}$ (circles), after soaking in $Au_{102}(SR)_{44}$ (squares) and after soaking in oxidized $Au_{102}(SR)_{44}$ (triangles).

In summary, the role of salts in radiofrequency heating of gold nanoparticles is unclear. Salts clearly confounded some earlier experimental interpretations of nanoparticle heating in simple solutions.[12,25,27] It appears, however, that salts in biological systems may not contribute to background heating, perhaps because they are comparatively immobile. Background salts may help elicit the maximum amount of thermal dissipation from metal nanoparticles immersed in RF fields.[28,29]

2.9 Critical Assessment of the Heating of Metal Nanoparticles with Applied Radio Frequencies

Twenty-five papers so far examine the heating of gold nanoparticles in RF (Table 2.1). Five of these papers challenge some aspect of gold nanoparticles heating in RF,[10-13,26] if not dismissing the entire phenomena. Parsing this controversy is complicated, because of differences in experimental approach that include frequency, antenna design, and nanoparticle preparation. We categorize the literature in terms of antenna design used in each experiment, as this commonality allows facile comparison

of reports made with the same antenna design. Table 2.1 also organizes the literature secondarily according to the diameter of AuNPs reported.

In terms of antenna design, capacitively coupled designs and solenoid antennae dominate the literature, accounting for 19 of the 24 reports. Eleven of the reports use the commercial Kanzius machine. There are 5 reports of solenoid generated RFMF, from 5 different labs. Other designs used that have not been adopted outside of a single lab include resonating chambers and microstrip waveguides, with unclear emphasis of B- or E- field. What these entire reports share in common is the examination of thermal dissipation of small pieces of gold in radio or microwave-frequency irradiation.

2.10 Capacitively Coupled Antennae

There are 13 reports using capacitively coupled electric fields, coming from a 4 different research groups. An apparent catalyst for this work was a cancer patient and retired radio-engineer, John Kanzius, who began working with academic surgeons to develop technology for non-invasive nanoparticle/RF based cancer hyperthermia.[24] One of the products of this collaboration is the Kanzius Machine, a capacitively coupled RF antenna. This instrument generates 13.56 MHz RF. The frequency is presumably chosen because it is in the industrial/medical frequency band, not regulated by the Federal Communications Commission (FCC). Industrial 13.56 MHz RF plasmas are commonly used to process semiconductor wafers and for RF-based surgical practices.

Early work with the Kanzius machine focused on cancer hyperthermia in both tissue culture and animal models, with some apparent success.[16,17,23]

In response to the suggestion that gold nanoparticles do not heat, a novel electrophoretic mechanism was proposed.[27,28] This electrophoretic mechanism

empirically fails to heat nanoparticles larger than 10 nm in diameter.[27] The theory for electrophoretic heating also predicts more heat than is yet observed for this system, meaning the system is not completely understood. Nonetheless, the heating appears real and independently confirmed among 3 labs. Notably, though, the heat observed for simple solutions of gold nanoparticles is much less than observed in earlier work with the Kanzius machine. This is most easily noted by comparing reported Specific Absorption Rate (SAR) values in recent and older papers (Table 2.1).

Early papers with the Kanzius machine reported SAR values on the order of 300,000 W/g (Table 2.1). More recent mechanistic work reports SAR values on the order of 2 W/g.[27] The more recent SAR value is on carefully desalted material and is concordant with the SAR value we reported in a different experimental setup of 9.1 W/g. A complete comparison of SAR values across this literature isn't possible because while reporting of SAR values is widespread for the heating of magnetic iron oxides in RF, but is not universally reported in the gold nanoparticle heating literature.

Much of the earlier literature with the Kanzius machine must, therefore be reinterpreted. SAR values larger than ~100W/g currently seem unrealistic, and the heating of AuNPs larger than 10 nm, as reported in previous papers, is an experimental result that is difficult to reconcile with current understanding.[16,25,31,63-66] Thus some of the early work may be artefactual, for instance attributing heating to particles that may be more appropriately attributed to saline.[12,13]

In summary, heat attributable to nanoparticles in Kanzius machine generated RF appears real when AuNPs are smaller than 10 nm in diameter. The Kanzius foundation website reports that the approach is moving forward into large-animal preclinical trials,

suggesting that the approach has proven effective at treating cancers in tissue culture and small animals.[71a]

2.11 Solenoid Generated RF Fields

There are 5 reports examining AuNPs heating in solenoid based antennae, from 5 different research labs.[10,14,19,20,67] Three of these reports examine the heating of the commercial product Nanogold™,[10,14,67] a 1.4 nm cluster suggested as $Au_{69}(PR_3)_{20}Cl_{12}^-$ [121,68,69]. One report examines the heating of iron-doped magnetic gold nanoparticles.[20] One report examines the heating of $Au_{102}(SR)_{44}$.[19] Notably, except for the iron doped 7.8 nm nanoparticle—which is an outlier in having iron content -- all of the nanoparticles used in solenoid based experiments are 1.4-1.5 nm in diameter, and significantly smaller than the nanoparticles used in Kanzius machine based experiments, the smallest of which were 5 nm.

Table 2.1. Summary and comparison of reports of RF and microwave heating of AuNPs. Many reports do not report specific absorption rate and do not include enough data for independent calculation.

Antenna Design	Operating Frequency	Operating Power	Particle Diameter	Application	Reference	SAR
Kanzius	13.56 MHz	200 – 800 W	5 nm	Cancer Hyperthermia	17	-
Kanzius	13.56 MHz	600 W	5 nm	Cancer Hyperthermia	23	~300 kW/g
Kanzius	13.56 MHz	600 W	5 – 250 nm	Mechanistic Study	25	380 kW/g
Kanzius	13.56 MHz	25 W	5 – 200 nm	Mechanistic Study	12	50nm; 8*10-17 W/AuNP
Capacitively Coupled	13.56 MHz	125 W	5 – 50 nm	Cancer Hypertherma	31	5nm, 356 kW/g
Kanzius	13.56 MHz	100 – 950 W	5 – 50 nm	Mechanistic Study	27	5nm, 1.82 W/kg 10nm, 1.24 W/kg
Kanzius	13.56 MHz	600 W	10 nm	Cancer Hyperthermia	64	-
Kanzius	13.56 MHz	600 W	10 nm	Mechanistic Study	70	-
Kanzius	13.56 MHz	10 – 100 W	13 nm	Cancer Hyperthermia	16	
Kanzius	13.56 MHz	200 – 250 W	20 nm	Cancer Hyperthermia	66	
Kanzius	13.56 MHz	200 W	20 nm	Cancer Hyperthermia	65	
Kanzius	13.56 MHz	25 W	100 nm	Mechanistic Study	30	
Theoretical E-field	13 MHz	Not Applicable	20 nm	Mechanistic Study	13	
Capacitively Coupled E-field	13.56 MHz	125 W	5 – 50 nm	Cancer Hypertherma	31	5nm, 356 kW/g
Solenoid	1GHz	0.4 – 4W	1.4 nm	DNA Melting	14	-
Solenoid	600 – 1000 kHz	Not reported	1.4 nm	Mechanistic Study	10	-
Solenoid	1 GHz	1.5 W	1.4nm	Aptamer Control	67	-
Multiple	13.56 MHz	50 W	1.5 nm	Mechanistic Study	19	9.1 W/g
Solenoid	100 KHz – 100 MHz	100 W	7.8 nm Fe Doped	Mechanistic Study	20	1.84 W/ g @ 40 MHz
Resonating Chamber	12 GHz	0.1W	10 nm	Amyloid Dissolution	15	989 W/g
Not Reported	12 GHz	0.1 W	10 nm	Amyloid Dissolution	22	989 W/g
Resonating Chamber	10 MHz – 50 GHz	0.1 W	12.5 nm	Amyloid Dissolution	21	-
Microstrip Waveguide	13.56 MHz	600W	15 nm	Mechanistic Study	11	
Microstrip Waveguide	13.56 MHz	600 W	10 – 30 nm	Mechanistic Study	26	-

Four of the papers attribute heating to nanoclusters in RF,[14,19,20,67] while one paper fails to observe heat attributable to nanoparticles.[10] In aggregate, this literature is surprising in that there is very little direct experimental follow-up to a very prominent and widely cited Nature paper.[14] The absence of direct experimental follow-up suggests

some difficulty in reproducing the Nature paper's results. In the report that fails to observe heat, Gupta and Kane examined local temperature of Nanogold™ conjugated to CdSe quantum dots (QD). They suggested that even subtle temperature changes at the nanocluster surface should induce a measurable change in fluorescence due to the close proximity of the gold cluster to the QD, and they fail to observe the change in fluorescence that they do observe for iron oxides which undoubtedly heat in RF. The frequency used in this report – 1000 kHz is lower than in others (13.56 MHz, 1 GHz), which could possibly account for the observational difference, but otherwise the report appears robust.

Another possible explanation for the small number of direct experimental follow-ups to the original Nature paper, as well as the failure to observe heat in one report, may lie with the oxidation state and therefore magnetism of the clusters. In one case, the gold nanoparticles are iron doped to make them magnetic, and indeed this work represents a bridge between the SPION literature.[20] In all other cases, with both Nanogold™ and $Au_{102}(SR)_{44}$, it is likely that the underlying superatomic structure is that of a $58e^-$ superatom.[32,47,68] It is known that ambient atmospheric oxygen is sufficient to oxidize diamagnetic $Au_{25}(SR)_{18}^{-1}$ to $Au_{25}(SR)_{18}^{0}$ which is a superatom paramagnet.[33] We showed that heat attributable to AuNPs is qualitatively related to oxidation state and resulting paramagnetism for $Au_{102}(SR)_{44}$.[19] We suggest that serendipitous oxidation, likely with atmospheric oxygen dissolved in the aqueous buffer that the Nanogold™ is dissolved in, may render this compound paramagnetic and capable of heating in an RFMF. This aspect of Nanogold™ heating in RF may help explain the small number of follow-up reports and also the failure to observe heat in one of the follow-up reports.[10]

2.12 Other Antenna Designs

One research group has reported on resonating chamber antennae, operated primarily in GHz frequency ranges for the explicit purpose of dissolving amyloid aggregates implicated in neurodegeneracy, specifically Alzheimer's disease.[15,21,22] Another research group has made fundamental inquiry into the nature of nanoparticle heating using microstrip waveguide antennae.[11,26] Neither of these strategies have been reproduced by other research labs.

The use of a resonating chamber antenna to heat 10nm AuNPs is inspired directly by the original report of DNA melting. These studies, however, use larger particles, different frequencies, and different antennae compared to the original report, making direct comparison difficult. These studies do report SAR values of ~989 W/g, which is a much larger SAR value than is observed in more recent and carefully controlled experiments (Table 2.1).

This work was always aimed at the applied goal of dissolving the amyloid aggregates that are a central feature of Alzheimer's disease. These authors note in their later works, citing the works of others in amyloid research, that dissolving amyloid aggregates may actually aggravate the disease, as a dissolved aggregate produces several new nucleation sites for formation of additional aggregates. In other words, dissolving aggregates does not neutralize them, and may accelerate the disease process. It is likely for this reason that this particular line of research appears to have ceased, with the last publication made in 2008.

The use of microstrip waveguides is reported by a single group that investigates the mechanism of heating. This group reports some heat from particles, but notes that

the heat they observe is miniscule compared to the heating rates reported by other groups.[11] The conclusions made in this report are similar to those made in other reports that question heating of AuNPs in RF: The heat observed is miniscule, greater heating is observed in samples that are not purified, presumably away from free salts, and that no presently considered mechanism can theoretically account for the amount of heat produced in experiments by groups using the Kanzius machine. Since this report focuses only on the thermal behavior of ~15 nm diameter AuNPs, the results have little bearing on the electrophoretic and magnetic mechanisms that emerged after publication of this work, which are empirically effective only for 10 nm and smaller particles.

2.13 Conclusions

The literature that reports on heating of AuNPs in RF electromagnetic fields contains a wide variety of experimental approaches. Despite the wide variety of approaches, some global conclusions can be drawn. The chief conclusion is that in some cases gold nanoparticles immersed in RF fields heat, and in other cases they do not. All reports of AuNPs larger than 10 nm in diameter heating in RF are, at this stage, questionable. Also, reports that claim an SAR larger than a ~100 W / gram are questionable. All things considered, it seems probable that these heating rates arise from conductivity of the sample.

Just as in the empirical case, where it seems clear now that some reports may be artifactual, some conclusions regarding mechanism appear safe to make. First, the pure Joule or inductive heating mechanism is unlikely. Other considered mechanisms, relying on dielectric or Mie theory are also unlikely as noted in papers that investigate them.[11,13] Particles larger than ~10 nm diameter probably do not heat detectably,

consistent with the recent experimental and theoretical reports.[19,27,28] Two mechanisms proposed within the past 18 months may explain heating of sub-10nm diameter particles. Electrophoretic mechanisms may heat AuNPs 10nm or smaller in concentrated electric fields. Magnetic mechanisms may function for sub-2.5 nm AuNPs and iron doped AuNPs.

If a combination of magnetic and electrophoretic mechanisms account for heating of particles smaller than 10 nm in diameter, then essentially every report that questions whether AuNPs heat in RF at all is problematic. Theoretical reports that question the phenomena don't consider these cooperative mechanisms, which emerged for consideration only after the theoretical reports were published.[11,13] Experimental reports that completely dismiss the phenomena are similarly problematic. Some of these reports only use AuNPs that are larger than 10 nm diameter.[11] Another study that questions the phenomena is difficult to evaluate as the applied frequency is lower than in other studies and the applied power is not reported.[10] Yet another study that dismisses the phenomenon[12] is followed up by the authors with a subsequent study highlighting that container shape is important in whether heat is observed.[18,30] In total, every report that questions the phenomenon of AuNPs heating does not dismiss electrophoretic heating of 10 nm or smaller particles, nor magnetic heating of 2.5 nm and smaller particles.

2.14 Future of AuNP heating in RF

For widespread adoption of this approach, it is clear that an empirically supported mechanism or set of mechanisms for heating must be validated. Presently, the electrophoretic mechanism overestimates heating and the magnetic mechanism

underestimates observed heat. These mechanisms are not yet rigorously tested in terms of frequency dependence, field type, and particle composition and topology. In many cases both mechanisms may be simultaneously operative. We expect that a full testing of all of these experimental variables will allow clarification of which heating mechanisms apply in various experimental conditions, ideally allowing accurate prediction and modeling of nanoparticle heat at varying distances from the surface of a particle. Such understanding may usher in a new era of nanoparticle mediated remote-thermal control of biology.[7]

REFERENCES

1. Glazer, E. S.; Curley, S. A. The Ongoing History of Thermal Therapy for Cancer. *Surg Oncol Clin N Am* **2011**, *20*, 229–235.

2. Mukherjee, S.; Libisch, F.; Large, N.; Neumann, O.; Brown, L. V.; Cheng, J.; Lassiter, J. B.; Carter, E. A.; Nordlander, P.; Halas, N. J. Hot Electrons Do the Impossible: Plasmon-Induced Dissociation of H2 on Au. *Nano Lett.* **2013**, *13*, 240–247.

3. Thomas, J. R. Particle Size Effect in Microwave-Enhanced Catalysis. *Catalysis Letters* **1997**, *49*, 137–141.

4. Hainfeld, J. F.; Slatkin, D. N.; Focella, T. M.; Smilowitz, H. M. Gold Nanoparticles: A New X-Ray Contrast Agent. *Br J Radiol* **2006**, *79*, 248–253.

5. Muhammed Madathumpady Abubaker Habeeb; Verma Pramod Kumar; Pal Samir Kumar; Kumar R. C. Arun; Paul Soumya; Omkumar Ramakrishnapillai Vyomakesannair; Pradeep Thalappil. Bright, NIR-Emitting Au23 from Au25: Characterization and Applications Including Biolabeling. *Chemistry – A European Journal* **2009**, *15*, 10110–10120.

6. Neumann, O.; Feronti, C.; Neumann, A. D.; Dong, A.; Schell, K.; Lu, B.; Kim, E.; Quinn, M.; Thompson, S.; Grady, N.; et al. Compact Solar Autoclave Based on Steam Generation Using Broadband Light-Harvesting Nanoparticles. *PNAS* **2013**, *110*, 11677–11681.

7. Ball, P. Material Witness: Nano Contraception. *Nature Materials* **2013**, *12*, 602.

8. Huang, X.; Jain, P. K.; El-Sayed, I. H.; El-Sayed, M. A. Plasmonic Photothermal Therapy (PPTT) Using Gold Nanoparticles. *Lasers Med Sci* **2008**, *23*, 217–228.

9. Dreaden, E. C.; Alkilany, A. M.; Huang, X.; Murphy, C. J.; El-Sayed, M. A. The Golden Age: Gold Nanoparticles for Biomedicine. *Chem. Soc. Rev.* **2012**, *41*, 2740–2779.

10. Gupta, A.; Kane, R. S.; Borca-Tasciuc, D.-A. Local Temperature Measurement in the Vicinity of Electromagnetically Heated Magnetite and Gold Nanoparticles. *Journal of Applied Physics* **2010**, *108*, 064901.

11. Liu, X.; Chen, H.; Chen, X.; Parini, C.; Wen, D. Low Frequency Heating of Gold Nanoparticle Dispersions for Non-Invasive Thermal Therapies. *Nanoscale* **2012**, *4*, 3945–3953.

12. Li, D.; Jung, Y. S.; Tan, S.; Kim, H. K.; Chory, E.; Geller, D. A. Negligible Absorption of Radiofrequency Radiation by Colloidal Gold Nanoparticles. *J Colloid Interface Sci* **2011**, *358*, 47–53.

13. Hanson, G. W.; Monreal, R. C.; Apell, S. P. Electromagnetic Absorption Mechanisms in Metal Nanospheres: Bulk and Surface Effects in Radiofrequency-Terahertz Heating of Nanoparticles. *Journal of Applied Physics* **2011**, *109*, 124306.

14. Hamad-Schifferli, K.; Schwartz, J. J.; Santos, A. T.; Zhang, S.; Jacobson, J. M. Remote Electronic Control of DNA Hybridization through Inductive Coupling to an Attached Metal Nanocrystal Antenna. *Nature* **2002**, *415*, 152–155.

15. Kogan, M. J.; Bastus, N. G.; Amigo, R.; Grillo-Bosch, D.; Araya, E.; Turiel, A.; Labarta, A.; Giralt, E.; Puntes, V. F. Nanoparticle-Mediated Local and Remote Manipulation of Protein Aggregation. *Nano Lett.* **2006**, *6*, 110–115.

16. Cardinal, J.; Klune, J. R.; Chory, E.; Jeyabalan, G.; Kanzius, J. S.; Nalesnik, M.; Geller, D. A. Noninvasive Radiofrequency Ablation of Cancer Targeted by Gold Nanoparticles. *Surgery* **2008**, *144*, 125–132.

17. Gannon, C. J.; Patra, C. R.; Bhattacharya, R.; Mukherjee, P.; Curley, S. A. Intracellular Gold Nanoparticles Enhance Non-Invasive Radiofrequency Thermal Destruction of Human Gastrointestinal Cancer Cells. *Journal of Nanobiotechnology* **2008**, *6*, 2.

18. Kim, H. K.; Hanson, G. W.; Geller, D. A. Are Gold Clusters in RF Fields Hot or Not? *Science* **2013**, *340*, 441–442.

19. McCoy, R. S.; Choi, S.; Collins, G.; Ackerson, B. J.; Ackerson, C. J. Superatom Paramagnetism Enables Gold Nanocluster Heating in Applied Radiofrequency Fields. *ACS Nano* **2013**, *7*, 2610–2616.

20. Wijaya, A.; Brown, K. A.; Alper, J. D.; Hamad-Schifferli, K. Magnetic Field Heating Study of Fe-Doped Au Nanoparticles. *Journal of Magnetism and Magnetic Materials* **2007**, *309*, 15–19.

21. Araya, E.; Olmedo, I.; Bastus, N. G.; Guerrero, S.; Puntes, V. F.; Giralt, E.; Kogan, M. J. Gold Nanoparticles and Microwave Irradiation Inhibit Beta-Amyloid Amyloidogenesis. *Nanoscale Res Lett* **2008**, *3*, 435–443.

22. Bastus, N. G.; Kogan, M. J.; Amigo, R.; Grillo-Bosch, D.; Araya, E.; Turiel, A.; Labarta, A.; Giralt, E.; Puntes, V. F. Gold Nanoparticles for Selective and Remote Heating of β-Amyloid Protein Aggregates. *Materials Science and Engineering: C* **2007**, *27*, 1236–1240.

23. Curley, S. A.; Cherukuri, P.; Briggs, K.; Patra, C. R.; Upton, M.; Dolson, E.; Mukherjee, P. Noninvasive Radiofrequency Field-Induced Hyperthermic Cytotoxicity in Human Cancer Cells Using Cetuximab-Targeted Gold Nanoparticles. *J. Exp. Ther. Oncol.* **2008**, *7*, 313–326.

24. Schmidt, C. The Kanzius Machine: A New Cancer Treatment Idea from an Unexpected Source. *J. Natl. Cancer Inst.* **2008**, *100*, 985–986.

25. Moran, C. H.; Wainerdi, S. M.; Cherukuri, T. K.; Kittrell, C.; Wiley, B. J.; Nicholas, N. W.; Curley, S. A.; Kanzius, J. S.; Cherukuri, P. Size-Dependent Joule Heating of Gold Nanoparticles Using Capacitively Coupled Radiofrequency Fields. *Nano Res.* **2009**, *2*, 400–405.

26. Liu, X.; Chen, H.; Yang, B.; Chen, X.; Parini, C.; Wen, D. Dielectric Property Measurement of Gold Nanoparticle Dispersions in the Millimeter Wave Range. *J Infrared Milli Terahz Waves* **2013**, *34*, 140–151.

27. Corr, S. J.; Raoof, M.; Mackeyev, Y.; Phounsavath, S.; Cheney, M. A.; Cisneros, B. T.; Shur, M.; Gozin, M.; McNally, P. J.; Wilson, L. J.; et al. Citrate-Capped Gold Nanoparticle Electrophoretic Heat Production in Response to a Time-Varying Radio-Frequency Electric Field. *J. Phys. Chem. C* **2012**, *116*, 24380–24389.

28. Sassaroli, E.; Li, K. C. P.; O'Neill, B. E. Radio Frequency Absorption in Gold Nanoparticle Suspensions: A Phenomenological Study. *J. Phys. D: Appl. Phys.* **2012**, *45*, 075303.

29. Pearce, J. A.; Cook, J. R. Heating Mechanisms in Gold Nanoparticles at Radio Frequencies. *Conf Proc IEEE Eng Med Biol Soc* **2011**, *2011*, 5577–5580.

30. Li, D.; Jung, Y. S.; Kim, H. K.; Chen, J.; Geller, D. A.; Shuba, M. V.; Maksimenko, S. A.; Patch, S.; Forati, E.; Hanson, G. W. The Effect of Sample Holder Geometry on Electromagnetic Heating of Nanoparticle and NaCl Solutions at 13.56 MHz. *IEEE Transactions on Biomedical Engineering* **2012**, *59*, 3468–3474.

31. Kruse, D. E.; Stephens, D. N.; Lindfors, H. A.; Ingham, E. S.; Paoli, E. E.; Ferrara, K. W. A Radio-Frequency Coupling Network for Heating of Citrate-Coated Gold Nanoparticles for Cancer Therapy: Design and Analysis. *IEEE Transactions on Biomedical Engineering* **2011**, *58*, 2002–2012.

32. Walter, M.; Akola, J.; Lopez-Acevedo, O.; Jadzinsky, P. D.; Calero, G.; Ackerson, C. J.; Whetten, R. L.; Grönbeck, H.; Häkkinen, H. A Unified View of Ligand-Protected Gold Clusters as Superatom Complexes. *PNAS* **2008**, *105*, 9157–9162.

33. Tofanelli, M. A.; Ackerson, C. J. Superatom Electron Configuration Predicts Thermal Stability of Au25(SR)18 Nanoclusters. *J. Am. Chem. Soc.* **2012**, *134*, 16937–16940.

34. de Heer, W. A. The Physics of Simple Metal Clusters: Experimental Aspects and Simple Models. *Rev. Mod. Phys.* **1993**, *65*, 611–676.

35. Murray, R. W. Nanoelectrochemistry: Metal Nanoparticles, Nanoelectrodes, and Nanopores. *Chem. Rev.* **2008**, *108*, 2688–2720.

36. Huang, T.; Murray, R. W. Visible Luminescence of Water-Soluble Monolayer-Protected Gold Clusters. *J. Phys. Chem. B* **2001**, *105*, 12498–12502.

37. Sardar, R.; Funston, A. M.; Mulvaney, P.; Murray, R. W. Gold Nanoparticles: Past, Present, and Future. *Langmuir* **2009**, *25*, 13840–13851.

38. L. Nealon, G.; Donnio, B.; Greget, R.; Kappler, J.-P.; Terazzi, E.; Gallani, J.-L. Magnetism in Gold Nanoparticles. *Nanoscale* **2012**, *4*, 5244–5258.

39. Zhu, M.; Aikens, C. M.; Hendrich, M. P.; Gupta, R.; Qian, H.; Schatz, G. C.; Jin, R. Reversible Switching of Magnetism in Thiolate-Protected Au25 Superatoms. *J. Am. Chem. Soc.* **2009**, *131*, 2490–2492.

40. Hicks, J. F.; Templeton, A. C.; Chen, S.; Sheran, K. M.; Jasti, R.; Murray, R. W.; Debord, J.; Schaaff, T. G.; Whetten, R. L. The Monolayer Thickness Dependence of Quantized Double-Layer Capacitances of Monolayer-Protected Gold Clusters. *Anal. Chem.* **1999**, *71*, 3703–3711.

41. Mulvaney, P. Surface Plasmon Spectroscopy of Nanosized Metal Particles. *Langmuir* **1996**, *12*, 788–800.

42. Qian, H.; Zhu, Y.; Jin, R. Atomically Precise Gold Nanocrystal Molecules with Surface Plasmon Resonance. *PNAS* **2012**, *109*, 696–700.

43. Dass, A. Faradaurate Nanomolecules: A Superstable Plasmonic 76.3 KDa Cluster. *J. Am. Chem. Soc.* **2011**, *133*, 19259–19261.

44. Lopez-Acevedo, O.; Akola, J.; Whetten, R. L.; Grönbeck, H.; Häkkinen, H. Structure and Bonding in the Ubiquitous Icosahedral Metallic Gold Cluster Au144(SR)60. *J. Phys. Chem. C* **2009**, *113*, 5035–5038.

45. Yi, C.; Tofanelli, M. A.; Ackerson, C. J.; Knappenberger, K. L. Optical Properties and Electronic Energy Relaxation of Metallic Au144(SR)60 Nanoclusters. *J. Am. Chem. Soc.* **2013**, *135*, 18222–18228.

46. Martin, T. P.; Bergmann, T.; Goehlich, H.; Lange, T. Shell Structure of Clusters. *J. Phys. Chem.* **1991**, *95*, 6421–6429.

47. Jadzinsky, P. D.; Calero, G.; Ackerson, C. J.; Bushnell, D. A.; Kornberg, R. D. Structure of a Thiol Monolayer-Protected Gold Nanoparticle at 1.1 Å Resolution. *Science* **2007**, *318*, 430–433.

48. Zeng, C.; Li, T.; Das, A.; Rosi, N. L.; Jin, R. Chiral Structure of Thiolate-Protected 28-Gold-Atom Nanocluster Determined by X-Ray Crystallography. *J. Am. Chem. Soc.* **2013**, *135*, 10011–10013.

49. Qian, H.; Eckenhoff, W. T.; Zhu, Y.; Pintauer, T.; Jin, R. Total Structure Determination of Thiolate-Protected Au38 Nanoparticles. *J. Am. Chem. Soc.* **2010**, *132*, 8280–8281.

50. Cheng, L.; Ren, C.; Zhang, X.; Yang, J. New Insight into the Electronic Shell of Au38(SR)24: A Superatomic Molecule. *Nanoscale* **2013**, *5*, 1475–1478.

51. Venzo, A.; Antonello, S.; Gascón, J. A.; Guryanov, I.; Leapman, R. D.; Perera, N. V.; Sousa, A.; Zamuner, M.; Zanella, A.; Maran, F. Effect of the Charge State (z = −1, 0, +1) on the Nuclear Magnetic Resonance of Monodisperse Au25[S(CH2)2Ph]18z Clusters. *Anal. Chem.* **2011**, *83*, 6355–6362.

52. Antonello, S.; Perera, N. V.; Ruzzi, M.; Gascón, J. A.; Maran, F. Interplay of Charge State, Lability, and Magnetism in the Molecule-like Au25(SR)18 Cluster. *J. Am. Chem. Soc.* **2013**, *135*, 15585–15594.

53. Akbari-Sharbaf, A.; Hesari, M.; Workentin, M. S.; Fanchini, G. Electron Paramagnetic Resonance in Positively Charged Au25 Molecular Nanoclusters. *The Journal of Chemical Physics* **2013**, *138*, 024305.

54. Rosensweig, R. E. Heating Magnetic Fluid with Alternating Magnetic Field. *Journal of Magnetism and Magnetic Materials* **2002**, *252*, 370–374.

55. Brown, W. F. Thermal Fluctuations of a Single-Domain Particle. *Phys. Rev.* **1963**, *130*, 1677–1686.

56. Pike, C. R.; Roberts, A. P.; Verosub, K. L. First Order Reversal Curve Diagrams and Thermal Relaxation Effects in Magnetic Particles. *Geophys J Int* **2001**, *145*, 721–730.

57. Dennis, C. L.; Ivkov, R. Physics of Heat Generation Using Magnetic Nanoparticles for Hyperthermia. *Int J Hyperthermia* **2013**, *29*, 715–729.

58. Smythe, W. R. *Static and dynamic electricity* **1950.**

59. Kim, B. H.; Lee, N.; Kim, H.; An, K.; Park, Y. I.; Choi, Y.; Shin, K.; Lee, Y.; Kwon, S. G.; Na, H. B.; et al. Large-Scale Synthesis of Uniform and Extremely Small-Sized Iron Oxide Nanoparticles for High-Resolution T1 Magnetic Resonance Imaging Contrast Agents. *J. Am. Chem. Soc.* **2011**, *133*, 12624–12631.

60. Cherukuri, P.; Glazer, E. S.; Curley, S. A. Targeted Hyperthermia Using Metal Nanoparticles. *Advanced Drug Delivery Reviews* **2010**, *62*, 339–345.

61. Svenson, S.; Tomalia, D. A. Dendrimers in Biomedical Applications--Reflections on the Field. *Adv. Drug Deliv. Rev.* **2005**, *57*, 2106–2129.

62. Song, K. H.; Kim, C.; Cobley, C. M.; Xia, Y.; Wang, L. V. Near-Infrared Gold Nanocages as a New Class of Tracers for Photoacoustic Sentinel Lymph Node Mapping on a Rat Model. *Nano Lett.* **2009**, *9* (1), 183–188.

63. Kruse, D. E.; Lai, C.-Y.; Stephens, D. N.; Sutcliffe, P.; Paoli, E. E.; Barnes, S. H.; Ferrara, K. W. Spatial and Temporal-Controlled Tissue Heating on a Modified Clinical Ultrasound Scanner for Generating Mild Hyperthermia in Tumors. *IEEE Trans Biomed Eng* **2010**, *57*, 155–166.

64. Glazer, E. S.; Zhu, C.; Massey, K. L.; Thompson, C. S.; Kaluarachchi, W. D.; Hamir, A. N.; Curley, S. A. Noninvasive Radiofrequency Field Destruction of Pancreatic Adenocarcinoma Xenografts Treated with Targeted Gold Nanoparticles. *Clin. Cancer Res.* **2010**, *16*, 5712–5721.

65. Glazer, E. S.; Massey, K. L.; Zhu, C.; Curley, S. A. Pancreatic Carcinoma Cells Are Susceptible to Noninvasive Radio Frequency Fields after Treatment with Targeted Gold Nanoparticles. *Surgery* **2010**, *148*, 319–324.

66. Glazer, E. S.; Curley, S. A. Radiofrequency Field-Induced Thermal Cytotoxicity in Cancer Cells Treated with Fluorescent Nanoparticles. *Cancer* **2010**, *116*, 3285–3293.

67. Taira, K.; Abe, K.; Ishibasi, T.; Sato, K; & Ikebukuro, K. Control of aptamer function using radiofrequency magnetic field. *J Nucleic Acids* **2011,** 103872.

68. Walter, M.; Moseler, M.; Whetten, R. L.; Häkkinen, H. A 58-Electron Superatom-Complex Model for the Magic Phosphine-Protected Gold Clusters (Schmid-Gold, Nanogold®) of 1.4-Nm Dimension. *Chem. Sci.* **2011**, *2*, 1583–1587.

69. Hainfeld, J. F.; Furuya, F. R. A 1.4-Nm Gold Cluster Covalently Attached to Antibodies Improves Immunolabeling. *J. Histochem. Cytochem.* **1992**, *40*, 177–184.

70. Raoof, M.; Zhu, C.; Kaluarachchi, W. D.; Curley, S. A. Luciferase-Based Protein Denaturation Assay for Quantification of Radiofrequency Field-Induced Targeted Hyperthermia: Developing an Intracellular Thermometer. *Int J Hyperthermia* **2012**, *28*, 202–209.

CHAPTER 3: ELECTROPHORETIC MECHANISM OF $Au_{25}(SR)_{18}$ HEATING IN RADIOFREQUENCY FIELDS

3.1 Synopsis

Gold nanoparticles in radiofrequency fields (RF) have been observed to heat. There is some debate over the mechanism of heating. $Au_{25}(SR)_{18}$ in RF is studied for the mechanistic insights obtainable from precise synthetic control over exact charge, size, and spin for this nanoparticle. An electrophoretic mechanism can adequately account for the observed heat. This study adds a new level of understanding to gold particle heating experiments, allowing for the first time a conclusive connection between theoretical and experimentally observed heating rates.

3.2 Introduction

The interaction of gold nanoparticles with radiofrequency radiation has been observed to generate heat. Applications of this heat include cancer hyperthermia,[1–4] amyloid dissolution,[5,6] aptamer control,[7] and enzyme activation.[8,9] Prompted by the promising applications of gold nanoparticle heat generation, the physical mechanisms by which nanomaterials may convert RF energy into thermal energy is an area of active inquiry.

Initial investigation into the observed heating rates of gold nanoparticle solutions in radiofrequency electric fields concluded that inductive currents caused joule heating of the electrons within the particle, resulting in a hot particle.[10–12] Consistent with joule-heating was the observation that particles smaller than 50 nm in diameter heat at nearly twice the rate of larger diameter gold nanoparticles, due to the higher resistivity of the

structures.[12] After several follow up reports, the validity of the joule heating mechanism was questioned both experimentally and theoretically.[13–16]

Two reports have concluded that observed heat could be attributed almost completely to background electrolyte resistive heating. They showed that AuNP resuspended in rigorously de-ionized water produce negligible observable heat or absorb negligible amounts of RF energy until protein corona formation increases the surface charge.[17,18] An additional report suggesting that oxidation of $Au_{102}(pMBA)_{44}$ clusters results in paramagnetism. Such paramagnetic clusters could heat by a mechanism similar to superparamagnetic iron-oxide particles.[19] In general reproducing heating rates experimentally observed in different labs is difficult and confounded by differences in RF antenna design, field properties and sample container geometry. We recently published a critical review of gold nanoparticle heating.[20]

An emerging consensus for mechanism of gold nanoparticle heating phenomena is that observed heating rates arise primarily from electrophoretic motion of charged particles in an alternating RF electric field. This is in addition to a small, likely negligible, contribution from the inductive heating of the particles.[13,14,21] This electrophoretic motion of the particles results in inelastic collisions with the surrounding solvent molecules, producing measurable heat.

Heat that arises from electrophoretic motion of particles is proportional to the net charge of the nanoparticle (including any double-layer) and inversely proportional to the hydrodynamic (Stokes-Einstein) radius. It is independent of the core composition and the same mechanism that applies to all charged species, including salts, at these frequencies. Observed heat depends not only on the size and charge of the dissolved

species, but also on the surrounding medium. Notably, the permittivity (and conductivity) of the solution, which are influenced by solvent structuring and ionic strength, have large effects on the 'background heating' rates of samples of nanoparticles in RF. [22–24]

The heating rates of silica nanoparticles and gold nanoparticles in RF are similar,[25,26] indicating that the composition of the particles does not substantially affect the observed heating rate. Still, a quantitative understanding of the heating phenomena is lacking. Uncertainties in assigning particle net charge and Stokes-Einstein radius may confound comparisons between experimentally observed and calculated heating rates.

3.3 Methods

Herein, we quantify the net charge and Stokes-Einstein radius of $Au_{25}(SR)_{18}$ nanoclusters (figure 3.1), and measure the heating rate of solutions of variants of this nanocluster in a 13.56 MHz radiofrequency field. The net charge of $Au_{25}(SR)_{18}$ clusters arises from a combination of the charge on the core (which is stable in +1, 0 and -1 oxidation states) and any charge arising from ionizable functional groups in the 18 ligands comprising the ligand shell.

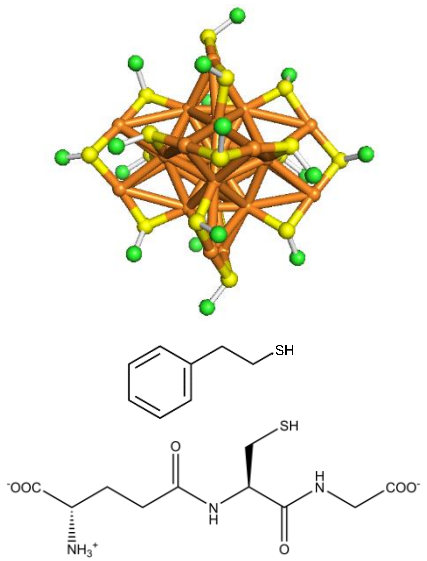

Figure 3.1. $Au_{25}(SR)_{18}$ crystal structure with gold atoms orange, sulfur in yellow and R groups in green. Below are the ligands PET and glutathione ligand used for organic and water solubility respectively.

Thus, net ionic charge of the cluster depends on the pKas of the ionizable groups and the pH of the surrounding solution, as well as any charge shielding arising from co-dissolved ions. The ligands protecting $Au_{25}(SR)_{18}$ in this study are either the tripeptide glutathione (γ-glutamyl cysteinyl glycine, abbreviated GSH) or phenylethanethiol (PET). Both ligands are shown schematically in figure 3.1. GSH ligation allows the quantification of ligand net charge on observed heat, whereas PET ligated clusters allow quantification of core net charge and any paramagnetic contributions to observed heat.

Each GSH ligand contains 3 ionizable functional groups: two carboxylic acids and the N-terminus of the peptide, with approximate pKas of pK1 = 2.12 (COOH), pK2 = 3.59 (COOH), pK3 = 8.75 (NH_2).[27] When ligated to a cluster, the dense packing of ionizable groups modifies their pKa.[28,29] For instance, the pKa of the carboxylic acid group of p-mercaptobenzoic acid increases by 2 pKa units when incorporated in the monolayer of $Au_{102}(pMBA)_{44}$.[29]

Because of the difficulty in predicting the magnitude of the effects of altered ligand pKa and any counterion shielding, we experimentally determined the net effective charge on the clusters as a function of pH. Experimentally, to ascertain the effective charge of the $Au_{25}(GSH)_{18}$ particles, we determined their electrophoretic mobility and Stokes-Einstein radius. These properties are related to effective charge by the Stokes-Einstein relation:

$$\mu_{EP} = \frac{q}{6\pi\eta a} \qquad (1)$$

Where μ_{EP} is the electrophoretic mobility in $m^2V^{-1}s^{-1}$ and a is the radius q is the particle charge and η is the viscosity of the solution.

3.4 Results and Discussion

We determined the electrophoretic mobility of $Au_{25}(GSH)_{18}$ as a function of pH by capillary electrophoresis. Figure 3.2, left panel, shows this at pH values 3.0, 4.0, 5.0, 6.0, 7.0, 8.0 and 9.0. In all cases, buffer concentrations were 10 mM. Different buffers were used to buffer at each pH, and this leads to differing values of ionic strength and conductivity (SI Table A.S1). The deviations in viscosity from deionized H_2O were assumed to be negligible for the different buffer conditions due to all of them being rather dilute (10 mM). Ferguson analysis of the mobility[30] of $Au_{25}(SG)_{18}$ clusters in polyacrylamide gel electrophoresis at pH 8.3 is similar to the high pH CE results at $2.2*10^{-4}$ in $cm^2\ V^{-1}s^{-1}$ (see SI Table S3).

We determined a hydrodynamic radius value of 1.65 nm by dynamic light scattering (Zetasizer Nano ZS, Malvern, see SI Figures A.S3 and A.S4). This value is in good agreement with literature values[31] and theoretical calculations using hydro pro and the theoretical structure of Akola.[32] We could not observe differences in hydrodynamic

diameter at different pH values within the resolution of this experiment. For particles with a larger or more compressible ligand shell, pH and ionic strength may underlie dramatic changes in observed Stoke-Einstein radius.[33] If the protecting ligand layer is a flexible polymer such as polyethelyne glycol (PEG), then the compression of the double layer can further change the hydrodynamic radius by allowing for compression or expansion of the ligand layer as well as the surrounding double layer. This can result in drastic changes in hydrodynamic radius for some particles. [34] For instance, in deionized H_2O, the Stokes-Einstein radius of particles may become much larger, and this effective increase in size may explain why gold nanoparticles show less heating in deionized water compared to solutions that are not rigorously deionized.

Using the measured electrophoretic mobilities and Stokes-Einstein radius, we calculate using equation 1 the charges on the clusters as -0.35, -5.87, -6.76, and -7.43 in units of electron charge for pHs 3, 5, 7, and 9 respectively. This is significantly less than the net charges assumed from estimates based on the pKa of the ligands at those pHs, where net charges ranging from -4.6 at pH 3 to -36 at pH 9 are expected (see SI Table S2). To ascertain the relationship between heat evolved by clusters in RF fields and the net charge on the cluster, we measured the heating rates of $Au_{25}(GSH)_{18}$ at the same pH / ionic strength as used in the experiments for charge determination in a custom-built RF generator. This instrument, operating at 13.56 MHz under 50W power is fully described in a prior publication.[19] We observe a clear dependence of heating rate on net charge, as shown in figure 3.2, right panel.

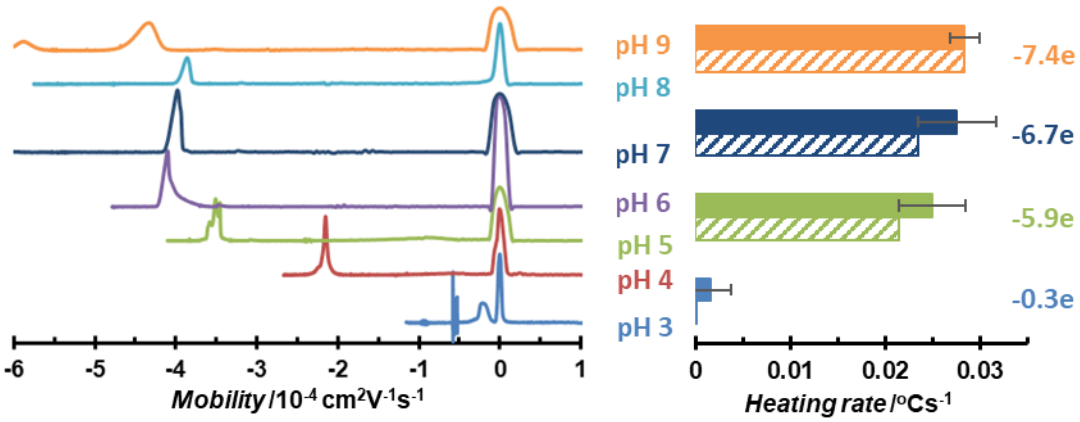

Figure 3.2. The left absorbance at 280nm from capillary electrophoresis plotted as mobility of the particles in buffers ranging from pH 9 to pH 3. The right is the background subtracted RF heating rates measured in the same buffers with pH 3, pH 5, pH 7 and pH 9. Calculated, normalized heating rates are shown as dashed columns next to the observed heating rates. The calculated charge on the cluster is shown next to each.

We found that modeling the heat produced by the $Au_{25}(SR)_{18}$ / counterion / buffer solutions in the electrophoretic heating model proposed by Sassaroli could account well for the observed heating rates.[14] In the Sassaroli model, the absorption of power as a result of electrophoretic movement is described by the imaginary component of the dielectric constant for the particles.[14] The power absorption due to dielectric loss is quantified by the following:

$$P = \frac{\phi}{\frac{4\pi}{3}a^3}\frac{E^2q^2}{\beta}\left(\frac{1}{1+\delta^2\omega^2}\right) \qquad (2)$$

Where $\delta = \frac{2\rho a^2}{3\eta}$ and $\beta = 6\pi\eta a$. Here q is the particle charge, a is the hydrodynamic radius of the particle, η is the dynamic shear viscosity of the solvent, E is the electric field strength, ρ is the particle density, and ϕ is the volume fraction of the particles.

The electric field strength needed in this equation is difficult to measure accurately. For instance, it is unclear whether a measured field strength in an 'empty

antenna' is representative of the field strength inside the solution/sample containing vessel that is inside the antenna.[15,22] (In other words, the shape of the sample container can modify the electric field strength in ways that are difficult to predict or measure.) Therefore, instead of attempting to measure 'specific absorption rates' (which would require a meaningful measurement of electric field strength) we instead compared normalized heating rates, relative to the highest power-absorbing sample. This makes the heating rate independent of the field strength. This approach is especially useful as it allows ratiometric comparison of experimental to calculated heating rates.

Figure 3.2, right panel, shows the theoretical heating rates for $Au_{25}(SG)_{18}$, measured at 4 different pH (i.e. particle charge) values. Theoretical heating rates are shown as hatched bars, just adjacent to the experimental heating rates (solid bars). We observe theoretical agreement within error, suggesting that observed, modest heating rates can be completely accounted for in these experiments by the Sassaroli proposed electrophoretic mechanisms. This mechanism is also in agreement with the results of Suchalkin in that they didn't observe any significant RF absorption until the surface charge of the particle was significantly increased via corona formation.[18] Additionally the mechanism shows a potential reason that groups observe attenuated RF heating after dialysis;[17,18] the hydrodynamic radius increases when ionic strength is reduced,[33] resulting in a lower charge to hydrodynamic volume ratio and attenuated electrophoretic motion.

In addition to studying the water-soluble $Au_{25}(SG)_{18}$ cluster, we also studied the organosoluble $Au_{25}(PET)_{18}$ cluster. This cluster is a useful point of study for examining the effects of not only charge, but also paramagnetism / diamagnetism and solvent

polarity. Solvent polarity is a useful parameter in understanding heating mechanisms, because nonpolar solvents such as toluene do not stabilize ions effectively and should quench heating mechanisms that depend on ionic movements. This is in comparison to polar organic solvents, such as dichloromethane (DCM) which, like water, promote ionization and facilitate ionic heating mechanisms.

Bulk electrolysis was used, as we have previously, to set the oxidation state of $Au_{25}(PET)_{18}$ to -1, 0 or +1 core charge states.[35–37] These oxidation states correspond to diamagnetic, paramagnetic and diamagnetic compounds (shown schematically in figure 3.3, right column), as we and others have previously reported.[37–42] We measured heating response for these cluster preparations in all three oxidation states and in polar and nonpolar solvents. Figure 3.3 shows heating rates of these preparations.

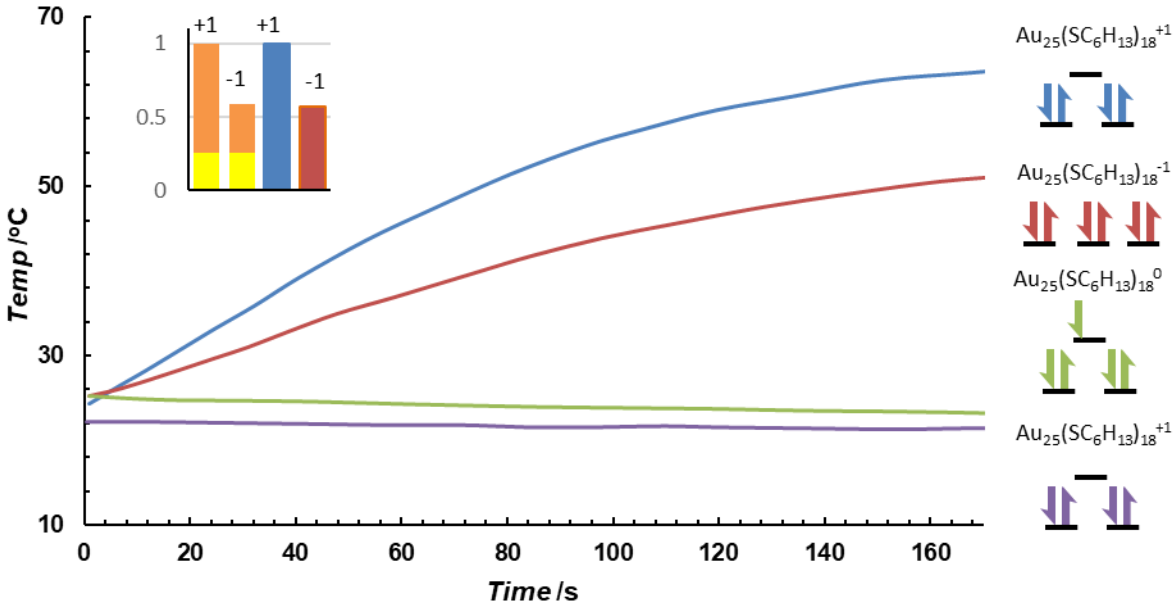

Figure 3.3. Heating rates as a function of charge state and solvent. Blue trace is +1 in DCM, red is -1 in DCM, green is 0 in DCM and purple is +1 in toluene. The inset shows normalized calculated heating rates of the +1 and -1 charge states next to the normalized measured heating rates in blue and red respectively. The orange color indicates heat from the counter ions, PF_6^- and TOA^+ and the yellow color indicates heat from the cluster's electrophoretic movement.

Essentially no thermal response is observed when the clusters are uncharged, but paramagnetic (green trace). Similarly, no thermal response is observed in the nonpolar solvent toluene, for both positively charged (purple trace), negatively charged, and uncharged clusters (data not shown). Conversely, a thermal response is observed for both positively and negatively charged clusters when dichloromethane is used as a solvent (blue trace, red trace).

The inset in figure 3.3 shows the theoretical fraction of observed heat attributable to the cluster (yellow bar) and the counterion (red orange bar) as calculated with equation 2. The observed heat from a cluster of unitary charge is identical, independent of whether the charge is +1 or -1. We attribute the difference in heating rates observed for the positive and negatively charged clusters entirely to the size of the counterion used in each experiment.

Previously, we studied the effect of the charge on the gold core of the $Au_{102}(SR)_{44}$ cluster, which may be a proxy for paramagnetism of the cluster.[19] For that cluster we observed heating that appeared to depend on whether the cluster was paramagnetic or not. Due to the technical difficulties of working in water, we could not assign an exact oxidation or spin state to these clusters. For the organosoluble preparations studied here, where we can assign an exact spin state, we see no evidence for a magnetic heating mechanism. For $Au_{25}(SR)_{18}$, heat is completely attributable to electrophoretic mechanisms.

3.5 Conclusions

In conclusion, heating mechanisms for inorganic nanoparticles in RF irradiation are a subject of current investigation. For the $Au_{25}(SR)_{18}$ cluster, which allows

mechanistic investigation through alteration of net charge, magnetic moment and solvation environment, we see only evidence for electrophoretic heating mechanisms. We modified the net charge of the particles by chemical modification of the ligand layer, changing the pH and bulk electrolysis to charge the metallic core of the particle. Overall, we conclude that in a variety of preparations, only electrophoretic mechanisms contribute to heat evolution from $Au_{25}(SR)_{18}$ clusters.

3.6 Experimental Methods

Particle synthesis: $Au_{25}(PET)_{18}$ particles were synthesized and purified by crystallization in the various charge states, exactly as previously reported.[37] The crystalized particles were thoroughly washed with toluene to remove excess salts. $Au_{25}(GS)_{18}$ was synthesized as previously reported.[43] Fractional precipitation was used to clean up the particles prior to purification by PAGE. This allowed more material to be loaded on each gel. After gel purification the particles were precipitated with 7:1 methanol to DI H_2O and washed 3x to rinse away any excess salt. The same batch of particles was used for all heating and electrophoresis studies to ensure that any additional salt remaining after washing would be consistent for all samples allowing for an accurate comparison between different pH buffers.

Ferguson analysis: Mobility of $Au_{25}(SG)_{18}$ in 1x TBE (pH is 8.3) was determined with gel electrophoresis by measuring the distance the band traveled (retention factor) as a function of gel percentage. To get a precise measurement of the distance, a gel imager was used to ensure precisely the same angle and height the picture was take from then imageJ was used and calibrated to the size of the gel. Distances of the bands were measured from the start of the well to the darkest part (highest intensity in imageJ) of

the band (corresponding to the most cluster), and band width was incorporated as error bars in the mobilities plotted. The linear fit of the cluster was then used to extrapolate the free mobility of the clusters. The mobility measured by gel is in good agreement with the mobility found using capillary electrophoresis.

Capillary electrophoresis: experiments were performed and an HP 61600AX 3DCE, using a 50 μm, 33 cm (24.5cm to the window) fused silica capillary treated with NaOH. It was run with positive polarity with an applied voltage of 15 kV and the temperature of the capillary was held constant at 25*C. Uv-vis absorption at 214, 254 and 280 nm was collected using chemstation software Rev A.08.03. Caffeine was used as a neutral electro osmotic flow indicator. Raw data from the absorbance at 280nm can be seen below bellow. Data was then converted to the mobility domain to better visualize the effect of the pH of the background electrolytes on the electrophoretic mobility of the clusters.

Radiofrequency heating experiments: 2mL samples were contained in 10mm NMR tube. They were heated in a custom constructed water cooled hollow copper solenoid powered by a 100W amplifier (ifi scx100) and a function generator (Philips PM5192) set to generate a sinusoidal current at 13.56 MHz. An impedance matching network was used and forward voltage from the amplifier was monitored and set at 50W. The temperature of the bulk solution was measure with a fiber optic temperature probe (Neoptix Nomad).

REFERENCES

1. Curley, S.; Cherukuri, P.; Briggs, K.; Patra, C.; Upton, M.; Dolson, E.; Mukherjee, P. Noninvasive Radiofrequency Field-Induced Hyperthermic Cytotoxicity in Human Cancer Cells Using Cetuximab-Targeted Gold Nanoparticles. *J Exp Ther Oncol* **2008**, *7*, 313–326.

2. Dutz, S.; Hergt, R. Magnetic Particle Hyperthermia—a Promising Tumour Therapy? *Nanotechnology* **2014**, *25*, 452001.

3. Hayashi, K.; Nakamura, M.; Miki, H.; Ozaki, S.; Abe, M.; Matsumoto, T.; Sakamoto, W.; Yogo, T.; Ishimura, K. Magnetically Responsive Smart Nanoparticles for Cancer Treatment with a Combination of Magnetic Hyperthermia and Remote-Control Drug Release. *Theranostics* **2014**, *4*, 834–844.

4. Haik, Y.; Mohite, V.; Chen, C.-J. Magnetic Nanoparticles for Self Controlled Hyperthermia Treatment of Tumors. Paper presented at 2005 NSTI Nanotechnology Conference and Trade Show: Bio Nano Materials*,* Anaheim California, **2005***, 300-303.*

5. Araya, E.; Olmedo, I.; Bastus, N. G.; Guerrero, S.; Puntes, V. F.; Giralt, E.; Kogan, M. J. Gold Nanoparticles and Microwave Irradiation Inhibit Beta-Amyloid Amyloidogenesis. *Nanoscale Res. Lett.* **2008**, *3*, 435–443.

6. Bastus, N. G.; Kogan, M. J.; Amigo, R.; Grillo-Bosch, D.; Araya, E.; Turiel, A.; Labarta, A.; Giralt, E.; Puntes, V. F. Gold Nanoparticles for Selective and Remote Heating of β-Amyloid Protein Aggregates. *Mater. Sci. Eng. C* **2007**, *27*, 1236–1240.

7. Taira, K.; Abe, K.; Ishibasi, T.; Sato, K.; Ikebukuro, K. Control of Aptamer Function Using Radiofrequency Magnetic Field. *J. Nucleic Acids* **2011**, *2011*, e103872.

8. Suzuki, M.; Aki, A.; Mizuki, T.; Maekawa, T.; Usami, R.; Morimoto, H. Encouragement of Enzyme Reaction Utilizing Heat Generation from Ferromagnetic Particles Subjected to an AC Magnetic Field. *Plos One* **2015**, *10*, 11.

9. Knecht, L. D.; Ali, N.; Wei, Y.; Hilt, J. Z.; Daunert, S. Nanoparticle-Mediated Remote Control of Enzymatic Activity. *ACS Nano* **2012**, *6*, 9079–9086.

10. Hamad-Schifferli, K.; Schwartz, J. J.; Santos, A. T.; Zhang, S.; Jacobson, J. M. Remote Electronic Control of DNA Hybridization through Inductive Coupling to an Attached Metal Nanocrystal Antenna. *Nature* **2002**, *415*, 152–155.

11. Kogan, M. J.; Bastus, N. G.; Amigo, R.; Grillo-Bosch, D.; Araya, E.; Turiel, A.; Labarta, A.; Giralt, E.; Puntes, V. F. Nanoparticle-Mediated Local and Remote Manipulation of Protein Aggregation. *Nano Lett.* **2006**, *6*, 110–115.

12. Moran, C. H.; Wainerdi, S. M.; Cherukuri, T. K.; Kittrell, C.; Wiley, B. J.; Nicholas, N. W.; Curley, S. A.; Kanzius, J. S.; Cherukuri, P. Size-Dependent Joule Heating of Gold Nanoparticles Using Capacitively Coupled Radiofrequency Fields. *Nano Res.* **2009**, *2*, 400–405.

13. Hanson, G. W.; Monreal, R. C.; Apell, S. P. Electromagnetic Absorption Mechanisms in Metal Nanospheres: Bulk and Surface Effects in Radiofrequency-Terahertz Heating of Nanoparticles. *J. Appl. Phys.* **2011**, *109*, 124306-124306–6.

14. Sassaroli, E.; Li, K. C. P.; O'Neill, B. E. Radio Frequency Absorption in Gold Nanoparticle Suspensions: A Phenomenological Study. *J. Phys. Appl. Phys.* **2012**, *45*, 075303.

15. Li, D.; Jung, Y. S.; Kim, H. K.; Chen, J.; Geller, D. A.; Shuba, M. V.; Maksimenko, S. A.; Patch, S.; Forati, E.; Hanson, G. W. The Effect of Sample Holder Geometry on

Electromagnetic Heating of Nanoparticle and NaCl Solutions at 13.56 MHz. *IEEE Trans. Biomed. Eng.* **2012**, *59*, 3468–3474.

16. Kim, H. K.; Hanson, G. W.; Geller, D. A. Are Gold Clusters in RF Fields Hot or Not? *Science* **2013**, *340*, 441–442.

17. Li, D.; Jung, Y. S.; Tan, S.; Kim, H. K.; Chory, E.; Geller, D. A. Negligible Absorption of Radiofrequency Radiation by Colloidal Gold Nanoparticles. *J. Colloid Interface Sci.* **2011**, *358*, 47–53.

18. Mironava, T.; Arachchilage, V. T.; Myers, K. J.; Suchalkin, S. Gold Nanoparticles and Radio Frequency Field Interactions: Effects of Nanoparticle Size, Charge, Aggregation, Radio Frequency, and Ionic Background. *Langmuir* **2017**, *33*, 13114–13124.

19. McCoy, R. S.; Choi, S.; Collins, G.; Ackerson, B. J.; Ackerson, C. J. Superatom Paramagnetism Enables Gold Nanocluster Heating in Applied Radiofrequency Fields. *ACS Nano* **2013**, *7*, 2610–2616.

20. Collins, C. B.; McCoy, R. S.; Ackerson, B. J.; Collins, G. J.; Ackerson, C. J. Radiofrequency Heating Pathways for Gold Nanoparticles. *Nanoscale* **2014**, *6*, 8459–8472.

21. Corr, S. J.; Raoof, M.; Mackeyev, Y.; Phounsavath, S.; Cheney, M. A.; Cisneros, B. T.; Shur, M.; Gozin, M.; McNally, P. J.; Wilson, L. J.; et al. Citrate-Capped Gold Nanoparticle Electrophoretic Heat Production in Response to a Time-Varying Radio-Frequency Electric Field. *J. Phys. Chem. C* **2012**, *116*, 24380–24389.

22. Corr, S. J.; Raoof, M.; Cisneros, B. T.; Orbaek, A. W.; Cheney, M. A.; Law, J. J.; Lara, N. C.; Barron, A. R.; Wilson, L. J.; Curley, S. A. Radiofrequency Electric-Field

Heating Behaviors of Highly Enriched Semiconducting and Metallic Single-Walled Carbon Nanotubes. *Nano Res.* **2015**, *8*, 2859–2870.

23. Lara, N. C.; Haider, A. A.; Ho, J. C.; Wilson, L. J.; Barron, A. R.; Curley, S. A.; Corr, S. J. Water-Structuring Molecules and Nanomaterials Enhance Radiofrequency Heating in Biologically Relevant Solutions. *Chem. Commun.* **2016**, *52*, 12630–12633.

24. Pantano, P.; Harrison, C. D.; Poulose, J.; Jr, D. U.; Norman, T. Q.; Braun, E. I.; Draper, R. K.; Overzet, L. J. Factors Affecting the 13.56-MHz Radio-Frequency-Mediated Heating of Gold Nanoparticles. *Appl. Spectrosc. Rev.* **2017**, *52*, 821–836.

25. Wosik, J.; Pande, R.; Xie, L.; Ketharnath, D.; Srinivasan, S.; Godin, B. Protein Adsorption Enhanced Radio-Frequency Heating of Silica Nanoparticles. *Appl. Phys. Lett.* **2013**, *103*.

26. Tamarov, K. P.; Osminkina, L. A.; Zinovyev, S. V.; Maximova, K. A.; Kargina, J. V.; Gongalsky, M. B.; Ryabchikov, Y.; Al-Kattan, A.; Sviridov, A. P.; Sentis, M.; et al. Radio Frequency Radiation-Induced Hyperthermia Using Si Nanoparticle-Based Sensitizers for Mild Cancer Therapy. *Sci. Rep.* **2014**, *4*, 7034.

27. Dawson, R. M. C.; Elliott, D. D.; Elliott W. H.; Jones, K.M.; *Data for Biochemical Research*, Third Edition.; Oxford University Press: Oxford, New York, 1989.

28. Templeton, A. C.; Chen, S.; Gross, S. M.; Murray, R. W. Water-Soluble, Isolable Gold Clusters Protected by Tiopronin and Coenzyme A Monolayers. *Langmuir* **1999**, *15*, 66–76.

29. Koivisto, J.; Chen, X.; Donnini, S.; Lahtinen, T.; Häkkinen, H.; Groenhof, G.; Pettersson, M. Acid–Base Properties and Surface Charge Distribution of the Water-Soluble Au102(pMBA)44 Nanocluster. *J. Phys. Chem. C* **2016**, *120*, 10041–10050.

30. Park, S.; Hamad-Schifferli, K. Evaluation of Hydrodynamic Size and Zeta-Potential of Surface-Modified Au Nanoparticle-DNA Conjugates via Ferguson Analysis. *J. Phys. Chem. C* **2008**, *112*, 7611–7616.

31. Hartje, L. F.; Munsky, B.; Ni, T. W.; Ackerson, C. J.; Snow, C. D. Adsorption-Coupled Diffusion of Gold Nanoclusters within a Large-Pore Protein Crystal Scaffold. *J. Phys. Chem. B* **2017**, *121*, 7652–7659.

32. Akola, J.; Walter, M.; Whetten, R. L.; Häkkinen, H.; Grönbeck, H. On the Structure of Thiolate-Protected Au25. *J. Am. Chem. Soc.* **2008**, *130*, 3756–3757.

33. Hill, R. J.; Li, F.; Doane, T. L.; Burda, C. Electrophoretic Interpretation of PEGylated NP Structure with and without Peripheral Charge. *Langmuir* **2015**, *31*, 10246–10253.

34. Li, F.; Allison, S. A.; Hill, R. J. Nanoparticle Gel Electrophoresis: Soft Spheres in Polyelectrolyte Hydrogels under the Debye–Hückel Approximation. *J. Colloid Interface Sci.* **2014**, *423*, 129–142.

35. Zhu, M.; Eckenhoff, W. T.; Pintauer, T.; Jin, R. Conversion of Anionic [Au25(SCH2CH2Ph)18]− Cluster to Charge Neutral Cluster via Air Oxidation. *J. Phys. Chem. C* **2008**, *112*, 14221–14224.

36. Tofanelli, M. A.; Ackerson, C. J. Superatom Electron Configuration Predicts Thermal Stability of Au25(SR)18 Nanoclusters. *J. Am. Chem. Soc.* **2012**, *134*, 16937–16940.

37. A. Tofanelli, M.; Salorinne, K.; W. Ni, T.; Malola, S.; Newell, B.; Phillips, B.; Häkkinen, H.; J. Ackerson, C. Jahn–Teller Effects in Au 25 (SR) 18. *Chem. Sci.* **2016**, *7*, 1882–1890.

38. Antonello, S.; Perera, N. V.; Ruzzi, M.; Gascón, J. A.; Maran, F. Interplay of Charge State, Lability, and Magnetism in the Molecule-like Au25(SR)18 Cluster. *J. Am. Chem. Soc.* **2013**, *135*, 15585–15594.

39. Venzo, A.; Antonello, S.; Gascón, J. A.; Guryanov, I.; Leapman, R. D.; Perera, N. V.; Sousa, A.; Zamuner, M.; Zanella, A.; Maran, F. Effect of the Charge State (Z = −1, 0, +1) on the Nuclear Magnetic Resonance of Monodisperse Au25[S(CH2)2Ph]18z Clusters. *Anal. Chem.* **2011**, *83*, 6355–6362.

40. Zhu, M.; Aikens, C. M.; Hendrich, M. P.; Gupta, R.; Qian, H.; Schatz, G. C.; Jin, R. Reversible Switching of Magnetism in Thiolate-Protected Au25 Superatoms. *J. Am. Chem. Soc.* **2009**, *131*, 2490–2492.

41. Kwak, K.; Choi, W.; Tang, Q.; Kim, M.; Lee, Y.; Jiang, D.; Lee, D. A Molecule-like $PtAu_{24}(SC_6H_{13})_{18}$ Nanocluster as an Electrocatalyst for Hydrogen Production. *Nat. Commun.* **2017**, *8*, 14723.

42. Kwak, K.; Tang, Q.; Kim, M.; Jiang, D.; Lee, D. Interconversion between Superatomic 6-Electron and 8-Electron Configurations of M@Au24(SR)18 Clusters (M = Pd, Pt). *J. Am. Chem. Soc.* **2015**, *137*, 10833–10840.

43. Dreier, T. A.; Compel, W. S.; Wong, O. A.; Ackerson, C. J. Oxygen's Role in Aqueous Gold Cluster Synthesis. *J. Phys. Chem. C* **2016**, *120*, 28288–28294.

CHAPTER 4: PRACTICAL STABILITY OF $Au_{25}(SR)_{18}^{-1/0/+1}$

4.1 Synopsis

Superatom electron shell and/or geometric shell filling underlies the thermodynamic stability of coinage and alkali metal clusters in both theoretical and experimental results. Factors beyond simple shell filling contribute substantially to the lifetime of ligated clusters in solution. Such factors include the nature of the solvent, the atmosphere and the steric size of the ligand shell. Here we systematically lay out a 'practical' stability model for ligated metal clusters, which includes both shell-closing aspects and colloidal stability aspects. Cluster decomposition may follow either fusion or fission pathways. Solvent polarity can be determinative of the decomposition pathway.

4.2 Introduction

Gas-phase and solution-phase (ligated) metal clusters comprised of alkali or coinage metals form in discrete, thermodynamically stable sizes for which a possible explanation of is found in superatom complex theory.[1] This describes molecule-like, discrete electronic states for the delocalized core metal electrons due to quantum confinement of gold nanoclusters with approximately 150 atoms or fewer. According to the superatom model, clusters with closed electronic shells are more stable than those with open electronic shells. Experimentally, we previously showed that superatomic electron configuration predicts the thermal stability of the clusters in differential scanning calorimetry experiments.[2] In this work, we observed that $Au_{25}(PET)_{18}^{-1}$ ($1S^21P^6$) was more thermally stable than $Au_{25}(PET)_{18}^{0}$ ($1S^21P^5$) or $Au_{25}(PET)_{18}^{+1}$ ($1S^21P^4$).

While superatom electron theory offers explanations for the discrete sizes[3–5] and thermal stability of the clusters, little investigation has been done into the practical, solution stability of the monolayer protected clusters.[6–8] This is an area that has been well studied for larger colloidal particles[9–12], but it is not clear whether the same principles apply to the smaller particles, and how colloidal descriptions of stability and superatomic descriptions of stability interact.

When a metal cluster or particle ‘decomposes’, that decomposition can be by fission/etching (breaking into smaller component pieces) or fusion (agglomerative growth of particles). Fission is an established pathway of decay for thiolate protected silver clusters.[7] Etching represents a type of fission that is widely used in synthesis of metal nanostructures and is highly dependent on oxygen in the case of thiol protected gold nanoparticles.[13–16] Instability through agglomerative growth pathways for nanoparticles is well established for water-soluble colloids[17] and also for organo-soluble colloids.[18,19] Theoretically, colloidal stability is attributed to a combination of van der Waals attraction, electrostatic double layer repulsion, and steric terms, described classically in DLVO and extended DLVO theory.[17,20] For water soluble nanoclusters, manipulation of ligand shell charge has been shown to improve solution stability.[8,21]

In this work, we endeavor to establish the “practical stability” of thiolate protected metal clusters, using $Au_{25}(SR)_{18}$ as a well-studied model system in which different oxidation states and ligand shells are easily accessible.[21–28] Such practical stability is important to establish as these clusters find their way into catalytic and imaging applications.[29,30] We find that practical stability appears to depend both on superatom stability concepts and on colloidal stability concepts.

4.3 Methods

Clusters were synthesized and purified as previously reported.[2] For air free decomposition studies, the dry cluster was suspended in solvent that was rigorously purged with argon and then transferred to a sealed Schlenk cuvette using Schlenk technique to avoid introduction of air. The cuvettes were sealed to avoid contamination by atmosphere and solvent evaporation. The in air samples were also put into the same Schlenk cuvette but balloons were used to ensure there was a constant atmosphere of air in the head space. UV-vis spectra were taken on an ocean optics usb4000 spectrometer using a DT-mini-2-GS deuterium light source at approximately 4 hour intervals throughout the day using the respective solvent in the same type of cuvette as a blank before each measurement. Concentration of the samples were found using the previously reported molar absorptivity at 680 nm of 8800 $cm^{-1}M^{-1}$. [31] Wavelengths at 680 and 605 nm were monitored so that the trough at 605 could be consistently set to zero and the feature at 680 nm could be compared between measurements. Then the starting concentration was normalized to one and the decrease in concentration was monitored as a decrease in the 680 nm feature. The concentrations were then plotted vs time to determine the reactant order in Au25 according to the integrated rate laws for zeroth, first and second order reactions. The best fit parameters were then used to determine the rate constant k and the half-life according to the integrated rate law for that given order.

4.4 Results and discussion

We observe that under some conditions, $Au_{25}(SR)_{18}$ cluster lifetime is extraordinarily longer than under other conditions, where the clusters degrade rapidly.

Figure 4.1, left panel illustrates this, showing $Au_{25}(SC_4H_9)_{18}^0$ in rigorously degassed THF, kept solvated under an argon atmosphere in the top set of traces. As judged by the $Au_{25}(SC_4H_9)_{18}^0$ optical absorbance spectrum, the cluster does not substantially decay over the course of 6 days (spectra are offset for clarity). By comparison, the spectrum of the same compound, when solvated in un-stabilized THF (bottom traces), loses the characteristic linear absorption features of $Au_{25}(SC_4H_9)_{18}^0$, evolving to a rather featureless spectrum typical of a heterogeneous mixture within the course of 3 days. Mechanistic information about decay pathways is extracted by examining the decrease in absorbance of the spectral feature at 680 nm, attributed to the HOMO-LUMO gap of the $Au_{25}(SR)_{18}$ cluster. Fitting the evolution of this peak to integrated kinetic rate laws (Table 1) produces information on the order of decay, rate constant, and half-life of the cluster in different environments. An example of this fitting is shown in figure 4.1, right panel.

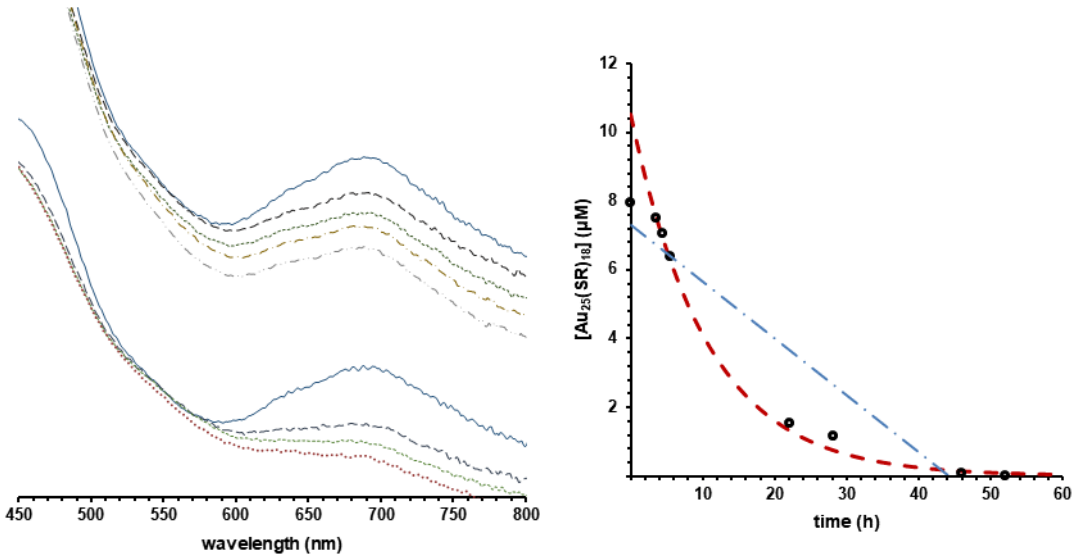

Figure 4.1. Left panel shows the optical spectrum of $Au_{25}(SC_4H_9)_{18}$ under argon as synthesized (solid blue trace), after approximately 1 day (purple-dashed trace), 2 days (green small-dash trace), 3 days (red dot-trace), 5 days (brown dash-dot trace), and 6 days (grey dash-dot-dot trace). The top set of traces show the evolution of the $Au_{25}(SC_4H_9)_{18}^{-1}$ spectrum in stabilized THF, while the bottom set of traces shows the

same experiment in unstabilized THF. The right panel plots the decay of $Au_{25}(PET)_{18}^0$ in acetone THF measuring concentration with 8800 $cm^{-1}M^{-1}$ extinction coefficient at 680 nm, black circles. Fits to this data by zeroth order decay and first order decay are shown as blue and red traces, respectively.

Many prior reports have noted informally that ligand steric size and/or net charge impacts the practical stability of thiolate protected gold clusters, suggesting that aspects of colloidal stability are important in overall practical stability of thiolate protected clusters.[32,33] The extent of the influence of ligand size on cluster stability, to our knowledge, has not previously been systematically investigated. To systematically establish the influence of ligand steric size on practical stability of $Au_{25}(SR)_{18}$, we investigated both the thermal and temporal stability of the compound with R groups ranging in size from (SCH_2CH_3, ethanethiol) to ($S(CH_2)_{11}CH_3$, dodecanethiol), as well as ($SCH_2CH_2C_6H_5$, phenylethanethiol, PET). To determine temporal stability of $Au_{25}(SR)_{18}$, optical spectra of the clusters were acquired at approximately 4 hour intervals over the length of the experiment. The temporal stability in air, shown as half-life of the cluster, for $Au_{25}(SR)_{18}^0$ in dichloromethane solvation,

Table 4.1 Integrated rate laws used to determine best fit and reactant order. The R^2 values here are shown for $Au_{25}(PET)_{18}^0$ in acetone data shown the right panel of figure 4.1.

Reactant order	**Integrated rate law fit**	**R^2 value**
Zero (red)	$[A] = [A]_0 - kt$	0.895
First (blue)	$[A] = [A]_0 e^{-kt}$	0.972
Second (not shown)	$\frac{1}{[A]} = \frac{1}{[A]_0} + kt$	0.0156

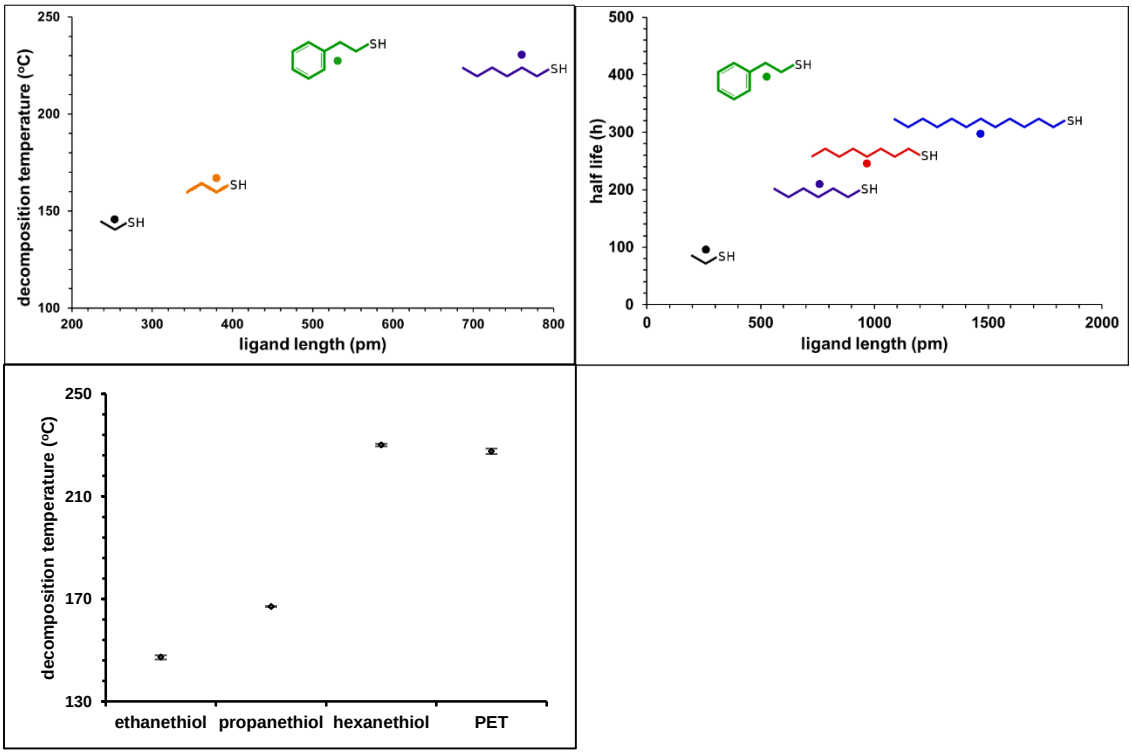

Figure 4.2. Left-hand panel shows the thermal stability of the clusters as it related to steric size of the protecting ligand. Right-hand panel shows the temporal stability of $Au_{25}(SR)_{18}^0$ as it relates to the steric size of the protecting ligand, air free in DCM. where SR= ethanethiol, hexanethiol, octanethiol, dodecanethiol and phenylethanethiol is shown in Figure 4.2, right panel. The thermal stability of a similar set of clusters was determined by differential scanning calorimetry (DSC). We previously used DSC to investigate the stability of $Au_{25}(PET)_{18}$ clusters as a function of oxidation state.[2] The raw DSC traces (supporting information p S17) show a large endotherm that we attribute to a decomposition temperature. The decomposition temperatures of clusters protected by ethanethiol, butanethiol, phenylethane thiol and hexanethiol are shown in the right panel of figure 4.2.

Overall, we observe a strong correlation with sterically larger ligands conferring greater thermal and temporal stability. The exception to this trend, phenylethanethiol, is easily rationalized as a more sterically demanding ligand which, by virtue of its branched nature, provides a larger 'cluster cone angle'[34] relative to its length, when compared to straight chain alkanethiols. We expect that branched alkanethiols may also show increased stability relative to absolute chain length.

We also examined the effect of cluster oxidation state on stability. Previously, we suggested that 'closed shell' superatom electron configurations are associated with greater thermal stability.[2] Here we expand this investigation to examine how the thermal stability of different oxidation states correlates to the steric size of the protecting ligand. Figure 4.3 shows the observed decomposition temperatures for Au_{25} clusters protected by ethanethiol (orange), propanethiol (purple), hexanethiol (blue), and phenylethanethiol(red) in the -1, and 0 oxidation states. As we observed before, increasing the oxidation state of the clusters, deviating from a full superatomic electron shell generally decreases their thermal stability. Figure 4.3 shows that when varied simultaneously, the steric size of the ligand provides a larger contribution than oxidation state to practical thermal stability.

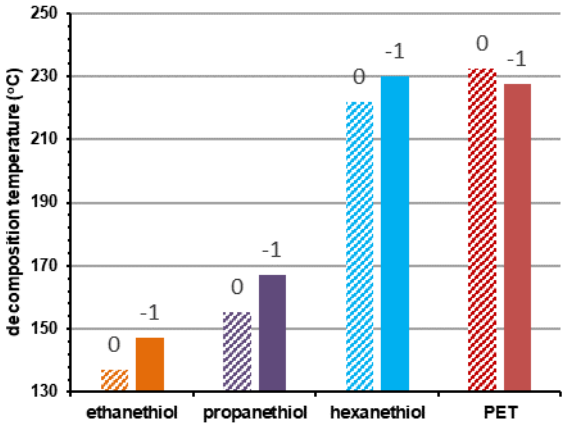

Figure 4.3 Oxidation state vs thermal decomposition temperature. Charge states are shown above each column.

In contrast to the influence of oxidation state on thermal stability of desolvated clusters, we observe a weaker correlation between oxidation state and lifetime in solution for solvated clusters. Instead, we observe that the nature of the solvent appears to dominate the lifetime of the clusters in solution (Figures 4.4 and 4.5).

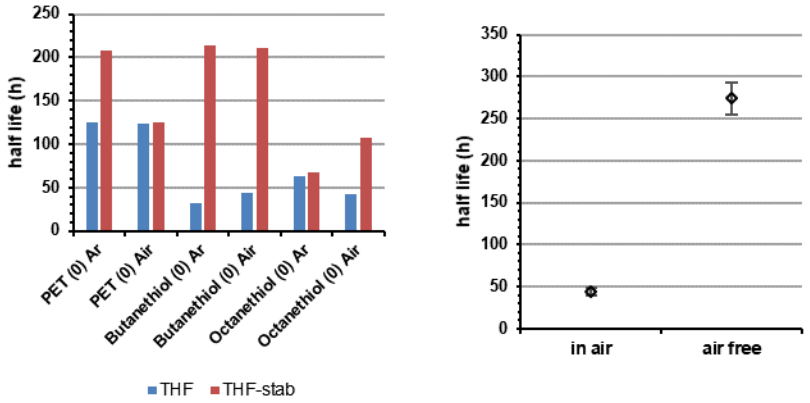

Figure 4.2. Left panel shows lifetimes of $Au_{25}(SR)_{18}^{0}$ in THF and stabilized THF. Generally, the inclusion of BHT increases observed half-life. The right panel shows inclusion vs. exclusion of ambient atmosphere for $Au_{25}(PET)_{18}^{-1}$ in dichloromethane, showing the lifetime of the cluster is substantially decreased by exposure to atmosphere.

We also examined the effect storage of $Au_{25}(SR)_{18}$ in solution under ambient atmosphere compared to in solution under argon. In general, we note that storage under argon preserves cluster integrity for longer periods of time than storage under atmosphere. Figure 4.4, right panel shows the lifetime of $Au_{25}(PET)_{18}$ in DCM under air and under argon. Here, storage under ambient atmosphere notably decreases the half life of the cluster. In the case of THF solvation, however, stabilized THF, which includes a radical inhibitor butylated hydroxytoluene (BHT) allows much longer half-lives, independent of the storage atmosphere. That argon atmospheres and BHT specifically both tend to enhance cluster lifetimes is suggestive of dissolved O_2 playing a role in the mechanism of cluster decomposition, potentially through an oxygen dependent etching process.[13]

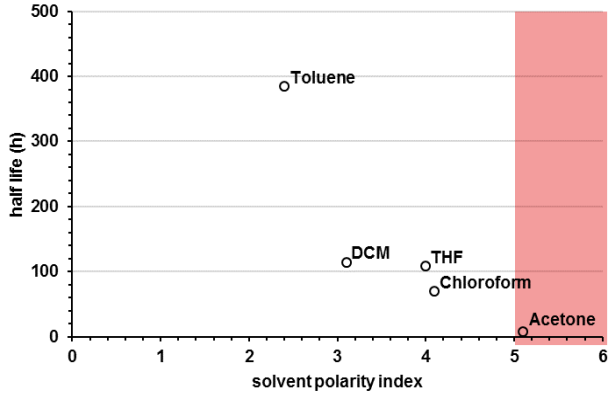

Figure 4.3 $Au_{25}(PET)_{18}^0$ half lives in Toluene, dichloromethane (DCM), Tetrahydrofuran, chloroform and acetone in air. The red-overlay represents regions of polarity solvent polarity where fusion mechanisms are (increasingly) observed.

In our preliminary observations, we noted that the nature of the solvent appeared to play a substantial role in the lifetime of solvated $Au_{25}(SR)_{18}$. We therefore made a systematic investigation of the effect of solvent on the lifetime of the clusters in solution. In testing several solvents used for organo-soluble clusters, we observed a strong correlation between solvent polarity and the lifetime of the cluster in solution, with more polar solvents promoting more rapid decomposition. Figure 4.5 shows the half lives of $Au_{25}(PET)_{18}^0$ in a selection of solvents arranged according to their polarity index.[35] The polarity index is a relative measure of the degree of interaction with a polar test solute, from Burdick & Jackson solvents.[35] In general we find that clusters are markedly more stable in toluene than many of the other solvents screened. Some combinations of ligand and solvent, such as butanethiol protected particles in toluene (supporting information B.S15) resulted in no measurable decay of the particles over 20 days.

This data provides insight into decay pathways. Decay of a suspended particle may arise from one of two either fusion of two particles or fission of a single particle into smaller components. These processes have distinct kinetics, with fission pathways following 0^{th} order kinetics and fusion pathways following 1^{st} order kinetics. An analysis

of the disappearance of characteristic peaks of Au_{25} and spectral evolution into something suggestive of a mixture suggests that the mechanism of decay is environment dependent.

We notice that solvent polarity appears not only determinative of half-life but also influences the mechanism of decay. Higher polarity solvents favor 0^{th} order decay (fission) pathways and lower polarity solvents favor 1^{st} order decay (fusion). Example fits of 0^{th} and 1^{st} order decay are shown the supporting information B.S12. This suggests that the higher polarity solvents may be driving aggregation of particles capped by non-polar ligands. We expect to observe the opposite trend for particles capped by polar ligands.

The trends shown are expected to be similar for other magic number sized monolayer protected noble metal clusters, but it's unknown if these trends will continue as clusters size increases into the range between cluster and colloidal particle.

4.5 Conclusions

Overall, this data allows us to suggest practical aspects of storage and handling that may preserve the integrity of $Au_{25}(SR)_{18}$ and by extension other thiolate protected clusters. In general, steric stabilization of the clusters appears to provide the greatest tunable variable for manipulating cluster half lives. The nature of the solvent also plays a large and unexpected role in the half-lives of the clusters. Less important but still appreciable contributions are made by oxidation state and relatedly the atmosphere under which clusters are stored. In some conditions, especially when dissolved in toluene with larger ligands the clusters appear to be very stable.

REFERENCES

1. Walter, M.; Akola, J.; Lopez-Acevedo, O.; Jadzinsky, P. D.; Calero, G.; Ackerson, C. J.; Whetten, R. L.; Grönbeck, H.; Häkkinen, H. A Unified View of Ligand-Protected Gold Clusters as Superatom Complexes. *Proc. Natl. Acad. Sci.* **2008**, *105*, 9157–9162.

2. Tofanelli, M. A.; Ackerson, C. J. Superatom Electron Configuration Predicts Thermal Stability of Au25(SR)18 Nanoclusters. *J. Am. Chem. Soc.* **2012**, *134*, 16937–16940.

3. Qian, H.; Eckenhoff, W. T.; Zhu, Y.; Pintauer, T.; Jin, R. Total Structure Determination of Thiolate-Protected Au38 Nanoparticles. *J. Am. Chem. Soc.* **2010**, *132*, 8280–8281.

4. Jadzinsky, P. D.; Calero, G.; Ackerson, C. J.; Bushnell, D. A.; Kornberg, R. D. Structure of a Thiol Monolayer-Protected Gold Nanoparticle at 1.1 Å Resolution. *Science* **2007**, *318*, 430–433.

5. Heaven, M. W.; Dass, A.; White, P. S.; Holt, K. M.; Murray, R. W. Crystal Structure of the Gold Nanoparticle [N(C8H17)4][Au25(SCH2CH2Ph)18]. *J. Am. Chem. Soc.* **2008**, *130*, 3754–3755.

6. Toikkanen, O.; Carlsson, S.; Dass, A.; Rönnholm, G.; Kalkkinen, N.; Quinn, B. M. Solvent-Dependent Stability of Monolayer-Protected Au38 Clusters. *J. Phys. Chem. Lett.* **2010**, *1*, 32–37.

7. Desireddy, A.; Kumar, S.; Guo, J.; Bolan, M. D.; Griffith, W. P.; Bigioni, T. P. Temporal Stability of Magic-Number Metal Clusters: Beyond the Shell Closing Model. *Nanoscale* **2013**, *5*, 2036–2044.

8. Yuan, X.; Goswami, N.; Mathews, I.; Yu, Y.; Xie, J. Enhancing Stability through Ligand-Shell Engineering: A Case Study with Au25(SR)18 Nanoclusters. *Nano Res.* **2015**, *8*, 3488–3495.

9. Moroi, Y. Stability of Colloidal Particles. In *Micelles*; Springer US, 1992; pp 131–148.

10. Zhou, J.; Ralston, J.; Sedev, R.; Beattie, D. A. Functionalized Gold Nanoparticles: Synthesis, Structure and Colloid Stability. *J. Colloid Interface Sci.* **2009**, *331*, 251–262.

11. Li, Y.; El-Sayed, M. A. The Effect of Stabilizers on the Catalytic Activity and Stability of Pd Colloidal Nanoparticles in the Suzuki Reactions in Aqueous Solution†. *J. Phys. Chem. B* **2001**, *105*, 8938–8943.

12. Laaksonen, T.; Ahonen, P.; Johans, C.; Kontturi, K. Stability and Electrostatics of Mercaptoundecanoic Acid-Capped Gold Nanoparticles with Varying Counterion Size. *ChemPhysChem* **2006**, *7*, 2143–2149.

13. Dreier, T. A.; Ackerson, C. J. Radicals Are Required for Thiol Etching of Gold Particles. *Angew. Chem. Int. Ed Engl.* **2015**, *54*, 9249–9252.

14. Prasad, B. L. V.; Stoeva, S. I.; Sorensen, C. M.; Klabunde, K. J. Digestive-Ripening Agents for Gold Nanoparticles: Alternatives to Thiols. *Chem. Mater.* **2003**, *15*, 935–942.

15. Schaaff, T. G.; Whetten, R. L. Controlled Etching of Au:SR Cluster Compounds. *J. Phys. Chem. B* **1999**, *103*, 9394–9396.

16. Brust, M.; Walker, M.; Bethell, D.; Schiffrin, D. J.; Whyman, R. Synthesis of Thiol-Derivatised Gold Nanoparticles in a Two-Phase Liquid–Liquid System. *J. Chem. Soc., Chem. Commun.* **1994**, No. 7, 801–802.

17. Zhang, W. Nanoparticle Aggregation: Principles and Modeling. In *Nanomaterial*; Capco, D. G., Chen, Y., Eds.; Advances in Experimental Medicine and Biology; Springer Netherlands, **2014**; pp 19–43.

18. Watzky, M. A.; Finke, R. G. Transition Metal Nanocluster Formation Kinetic and Mechanistic Studies. A New Mechanism When Hydrogen Is the Reductant: Slow, Continuous Nucleation and Fast Autocatalytic Surface Growth. *J. Am. Chem. Soc.* **1997**, *119*, 10382–10400.

19. Thanh, N. T. K.; Maclean, N.; Mahiddine, S. Mechanisms of Nucleation and Growth of Nanoparticles in Solution. *Chem. Rev.* **2014**, *114*, 7610–7630.

20. Hotze, E. M.; Phenrat, T.; Lowry, G. V. Nanoparticle Aggregation: Challenges to Understanding Transport and Reactivity in the Environment. *J. Environ. Qual.* **2010**, *39*, 1909–1924.

21. Shichibu, Y.; Negishi, Y.; Tsunoyama, H.; Kanehara, M.; Teranishi, T.; Tsukuda, T. Extremely High Stability of Glutathionate-Protected Au25 Clusters Against Core Etching. *Small* **2007**, *3*, 835–839.

22. Akola, J.; Walter, M.; Whetten, R. L.; Häkkinen, H.; Grönbeck, H. On the Structure of Thiolate-Protected Au25. *J. Am. Chem. Soc.* **2008**, *130*, 3756–3757.

23. Antonello, S.; Perera, N. V.; Ruzzi, M.; Gascón, J. A.; Maran, F. Interplay of Charge State, Lability, and Magnetism in the Molecule-like Au25(SR)18 Cluster. *J. Am. Chem. Soc.* **2013**, *135*, 15585–15594.

24. A. Tofanelli, M.; Salorinne, K.; W. Ni, T.; Malola, S.; Newell, B.; Phillips, B.; Häkkinen, H.; J. Ackerson, C. Jahn–Teller Effects in Au 25 (SR) 18. *Chem. Sci.* **2016**, *7*, 1882–1890.

25. Parker, J. F.; Fields-Zinna, C. A.; Murray, R. W. The Story of a Monodisperse Gold Nanoparticle: Au25L18. *Acc. Chem. Res.* **2010**, *43*, 1289–1296.

26. Negishi, Y.; Chaki, N. K.; Shichibu, Y.; Whetten, R. L.; Tsukuda, T. Origin of Magic Stability of Thiolated Gold Clusters: A Case Study on Au25(SC6H13)18. *J. Am. Chem. Soc.* **2007**, *129*, 11322–11323.

27. Venzo, A.; Antonello, S.; Gascón, J. A.; Guryanov, I.; Leapman, R. D.; Perera, N. V.; Sousa, A.; Zamuner, M.; Zanella, A.; Maran, F. Effect of the Charge State (z = −1, 0, +1) on the Nuclear Magnetic Resonance of Monodisperse Au25[S(CH2)2Ph]18z Clusters. *Anal. Chem.* **2011**, *83*, 6355–6362.

28. Zhu, M.; Aikens, C. M.; Hollander, F. J.; Schatz, G. C.; Jin, R. Correlating the Crystal Structure of A Thiol-Protected Au25 Cluster and Optical Properties. *J. Am. Chem. Soc.* **2008**, *130*, 5883–5885.

29. Chen, L.-Y.; Wang, C.-W.; Yuan, Z.; Chang, H.-T. Fluorescent Gold Nanoclusters: Recent Advances in Sensing and Imaging. *Anal. Chem.* **2015**, *87*, 216–229.

30. Li, G.; Jin, R. Atomically Precise Gold Nanoclusters as New Model Catalysts. *Acc. Chem. Res.* **2013**, *46*, 1749–1758.

31. Kawasaki, H.; Kumar, S.; Li, G.; Zeng, C.; Kauffman, D. R.; Yoshimoto, J.; Iwasaki, Y.; Jin, R. Generation of Singlet Oxygen by Photoexcited Au25(SR)18 Clusters. *Chem. Mater.* **2014**, *26*, 2777–2788.

32. Templeton, A. C.; Chen, S.; Gross, S. M.; Murray, R. W. Water-Soluble, Isolable Gold Clusters Protected by Tiopronin and Coenzyme A Monolayers. *Langmuir* **1999**, *15*, 66–76.

33. Ackerson, C. J.; Jadzinsky, P. D.; Kornberg, R. D. Thiolate Ligands for Synthesis of Water-Soluble Gold Clusters. *J. Am. Chem. Soc.* **2005**, *127*, 6550–6551.

34. Mingos, D. M. P. Steric Effects in Metal Cluster Compounds. *Inorg. Chem.* **1982**, *21*, 464–466.

35. Laboratories, B. & J. *Solvent Guide*; Burdick and Jackson Laboratories, **1984**.

CHAPTER 5: RADIOFREQUENCY REMOTE CONTROL OF THERMOLYSIN ACTIVITY

5.1 Synopsis

Nearly all biological processes are regulated by enzymes, precise control over specific enzymes could create the potential for controlling cellular processes remotely. We have successfully shown that the thermophilic enzyme thermolysin can be remotely activated in 17.76 MHz radiofrequency (RF) fields when covalently attached to 6.1 nm gold coated magnetite nanoparticles. Without raising the bulk solution temperature, we observe enzyme activity as if the solution was 16 ± 2 °C warmer in RF fields, or an increase in enzymatic rate of 56 ± 8%. Kinetics studies show that the activity increase of the enzyme is consistent with the induced fit of a hot enzyme with cold substrate.

5.2 Introduction

The use of temperature changes to modulate biological processes is ubiquitous. Well known examples include cooking to neutralize foodborne pathogens, the polymerase chain reaction (PCR),[1–5] thermal cancer treatment,[6–10] and thermal deactivation of enzymes (e.g., restriction endonucleases).[11–13] These processes all rely on bulk(macro)-scale heating.

The routine use of thermal manipulation of biological processes is ‘bulk heating’ – heating the entire sample. However, the possibility of heating discrete and defined local regions within a sample offers the potential to extend the paradigm of thermal manipulation of biological samples to allow targeting of discrete molecules with minimal collateral heating.

The advent of nanoparticles that convert external stimuli to heat gives rise to the possibility that thermal modulation of biological processes could be spatially targeted with high resolution. Indeed, inorganic particles that heat upon thermal stimuli have been used to modulate biological activity. Gold nanoparticles conjugated to DNA can thermally modulate DNA hybridization.[14] Micron-sized ferromagnetic iron oxides can thermally control the activity of amylase under 0.34 MHz RF irradiation.[15] Dehalogenase enzymes immobilized in a gel matrix with iron oxide particles of unknown size could be thermally controlled using the nanoparticles to heat the entire hydrogel.[16] Gold nanorods that heat upon NIR, 800 nm laser stimulation can modulate the activity of glucokinase.[17]

Prior examples of particle mediated influence of enzyme activity are done with particles of widely varying size, from micron sized iron oxides to 30 x 10 nm nanorod.[17] The different sizes of particle could imply different spatial resolutions to which heat can be delivered. For instance, micron and 100+ nm sized particles could be effective at cellular resolution—heating nearby cells but not far away cells,[18,19] while sub-10nm sized particles may heat at molecular resolution—heating nearby molecules but not far-away molecules. We used smaller particles (6.1 nm) for improved heat resolution and an increase in surface area to volume ratio, allowing for a more area for labeling with heating targets and heat transfer. Figure 5.1 summarizes the differences in surface area to volume ratio and shows the striking difference for a fixed volume fraction of particles.

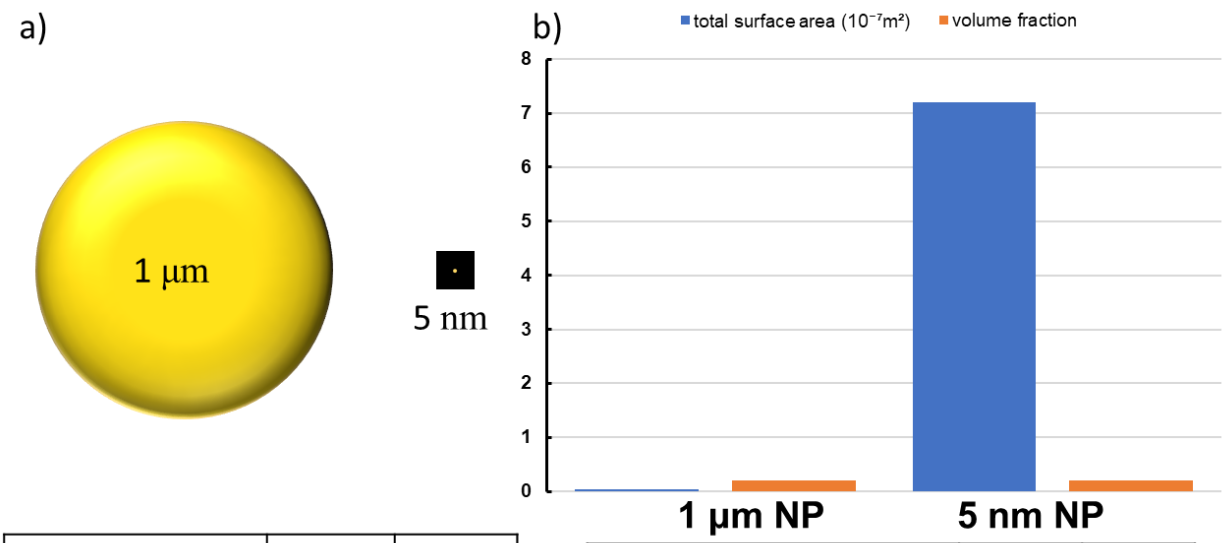

	1 µm	5 nm
Volume (m^3)	$5.236*10^{-19}$	$6.54*10^{-26}$
Surface Area (m^2)	$3.14*10^{-12}$	$7.85*10^{-17}$
Ratio SA:V	$2.5*10^{7}$	$1.2*10^{9}$
Ratio of SA:V ratios	1	48

	1 µm	5 nm
Volume Fraction in 3000 μm^3 cell	0.2	0.2
Number of Particles	1145	$9.17*10^{9}$
Total Surface Area (m^2)	$3.6*10^{-9}$	$7.2*10^{-7}$
Ratio	1	200

Figure 5.1. a) Comparison of surface area to volume of 1 micrometer and 5 nanometer diameter particles, pictures of particles are to scale. b) comparison of total surface area (in 10-7 m2 units) from a constant volume fraction of 1 micrometer and 5 nanometer diameter particles.

Herein, we demonstrate the first thermal manipulation of enzymatic activity by 'hot' nanoparticles at molecular resolution. We use 6.1 nm gold coated magnetite particles *covalently linked* to the thermostable protease enzyme, thermolysin. The superparamagnetic 4.5 nm magnetite cores heat under radiofrequency (RF) irradiation at 17.76 MHz, as the magnetic field torques the magnetic moments and the particles relax via Neel relaxation mechanisms.[20–24]

We observe an increase of thermolysin activity that is proportional to the applied RF power (and B field strength), without increasing the bulk temperature of the solution. The effective temperature of thermolysin can be correlated to different power inputs. We observe unique enzyme kinetics, consistent with a hot enzyme and cold substrate.

5.3 Results and Discussion

We investigated the activity of Thermolysin covalently conjugated to 6.1 nm diameter gold coated magnetite particles under RF irradiation. Thermolysin is a 34.6 kDa metalloprotease from thermophilic bacteria Bacillus thermoproteolyticus.[25–27] It is active in the hydrolysis of peptide bond with a preference for peptide bonds between hydrophobic residues. Its activity is maximized at pH 8 and increases with temperature until 70°C at which point it denatures. As a thermostable enzyme in bioconjugation methods, it is preferred over many others because there are no disulfide bonds, which many thermophilic enzymes have for improved stability at high temperatures. Such disulfide bonds, however, could potentially break under reducing conditions in favor of formation of a bond with the gold particle surface.

Magnetite particles were used because they are the superparamagnetic particles most frequently used in the literature for RF heating experiments. We gold coated the particles to stabilize the particles and allow for a robust covalent attachment of the conjugates through gold thiolate bonds, without negatively impacting the magnetic properties.[28–30] The optimal size magnetite cores were found for our system (17.7 MHz) to be 4 nm diameter.[20] We then coated the particles with the minimal amount of gold that would still allow for phase transferring and full ligand exchange without etching away and destroying the particle stability. For complete details of the synthesis and phase transfer see appendix C1 pg 140.

Thermolysin was attached to the gold coated iron-oxide particles through peptide bond formation using the carboxylic acid terminated ligands on the particles and the solvent accessible free lysine residues on thermolysin.[31,32] To significantly improve yield

and decrease reaction time, a novel procedure was developed using HATU as a coupling reagent in buffer without any organic solvents (for details see appendix C2 pg 143). This coupling procedure can be universally applied to enzymes, including those with very poor water solubility, a weak affinity for the ligand coating of the particle and high sensitivity to organic solvents like thermolysin.

To monitor activity of the thermolysin conjugates a colorimetric assay was used. As the succinylated casein substrate is digested by thermolysin, hydrolyzed peptide bonds create primary amines which react with the colorimetric reagent, 2,4,6-trinitrobenzene sulfonic acid (TNBSA) to form an orange colored product that is monitored with uv-Vis spectrometer at 430 nm (appendix C3). To obtain the velocity (i.e., activity) of the conjugates in the various environments, the absorbance at 430 nm of 0, 1, 2, and 3 minutes aliquots (time points) were graphed vs time and the slope of the linear relationship is the velocity in units of min^{-1}.

The 17.76 MHz RF field was generated using a homemade water-cooled copper solenoid. A function generator was used to make a sinusoidal 17.76 MHz signal that was amplified and sent to the coil. An oscilloscope was used to monitor the output of the amplifier and an impedance matching box was used to ensure that the applied power was not reflected back into the power amplifier, see figure 5.2 for an illustration of the heating system. The temperature of the solution was measured using a fiber optic temperature probe. The water cooling system was made so that heat from the coil did not increase the temperature of the sample, even after doing multiple experiments in a row. For complete system details see appendix C4.

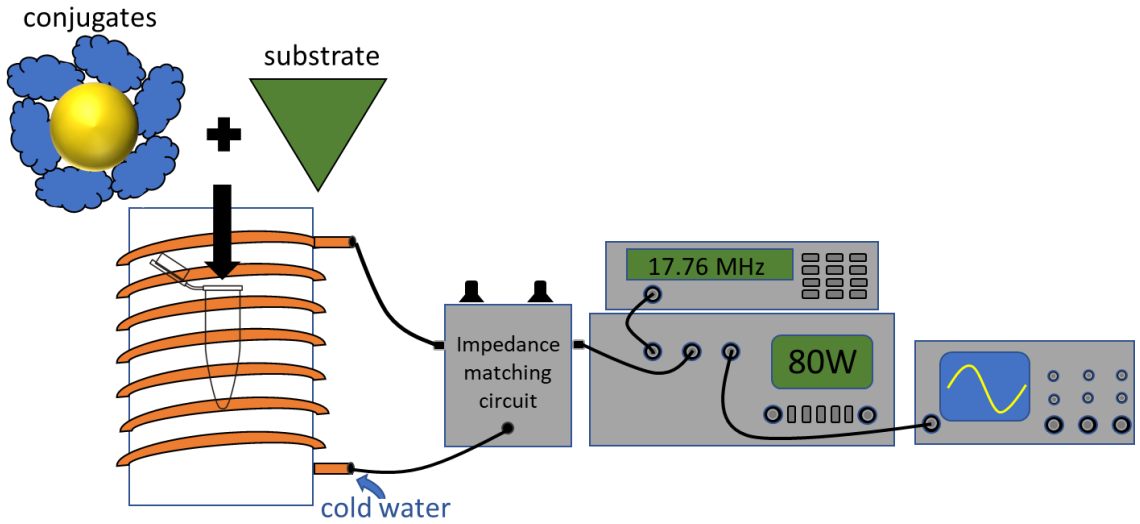

Figure 5.2. Illustration of radiofrequency heating system. A function generator is used to create a sinusoidal 17.76 MHz signal which is sent to a power amplifier. The signal is then sent through an impedance matching circuit and into the water cooled solenoid. For details see appendix C4 pg 150.

Preliminary experiments suggested higher power and higher frequency both increased the activity of enzyme/particle conjugates. The reported experiments were executed at 17.76 MHz and 80 W incident power, as these were the highest values of incident power and frequency that we could accomplish with our equipment.

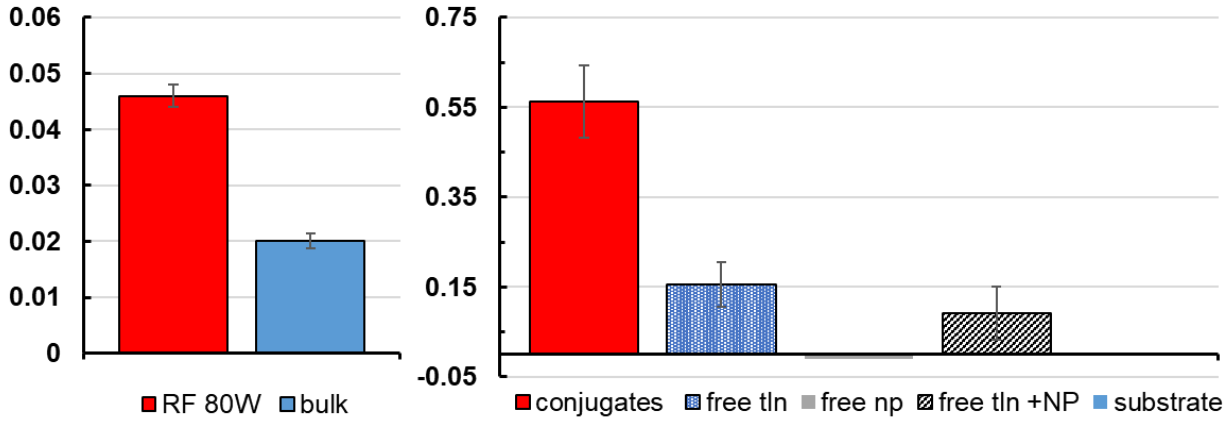

Figure 5.3. Left side shows RF at 80w vs bulk activity at the same temperature without RF field. Error bars represent standard deviation of four replicates. Right side shows control experiment with y axis representing activity increase over bulk in RF. Error bars represent triplicate measurements.

Figure 5.3, left panel, illustrates the increase in observed thermolysin/NP activity by colorimetric assay that occurs under these RF conditions. Overall, we observe that the thermolsyin/NP conjugate activity is increased by 56 ± 8% under the 80 W, 17.76MHz RF irradiation when compared to a control reaction at the same solution temperature (as measured with a fiber optic (i.e., metal-free) temperature probe). Figure 5.3, right panel shows the activity of each component of the thermolysin/NP conjugates (e.g., thermolsyin alone, NP alone) as well as the activity of thermolysin in the presence of unconjugated NP. Overall, we see a clear increase in activity of the enzyme relative to the controls. The measured maximum solution temperature in the RF fields was 17ºC, indicating that the increase in enzyme activity observed is a local effect, and does not extend to heating the bulk solution. Overall, we interpret this set of control experiments as validating that the observed increase in activity under RF is attributable primarily to local temperature increase around the nanoparticle that increases the effective operating temperature of covalently attached enzymes.

The data in figure 5.3 were all collected at 17°C solution temperature, which is far from the optimal thermolysin temperature of 70°C. By comparing the activity of thermolysin at various RF incident power values to the activity of thermolysin at various solution temperatures, we can propose effective ‘local’ temperature values for RF heated enzymes.

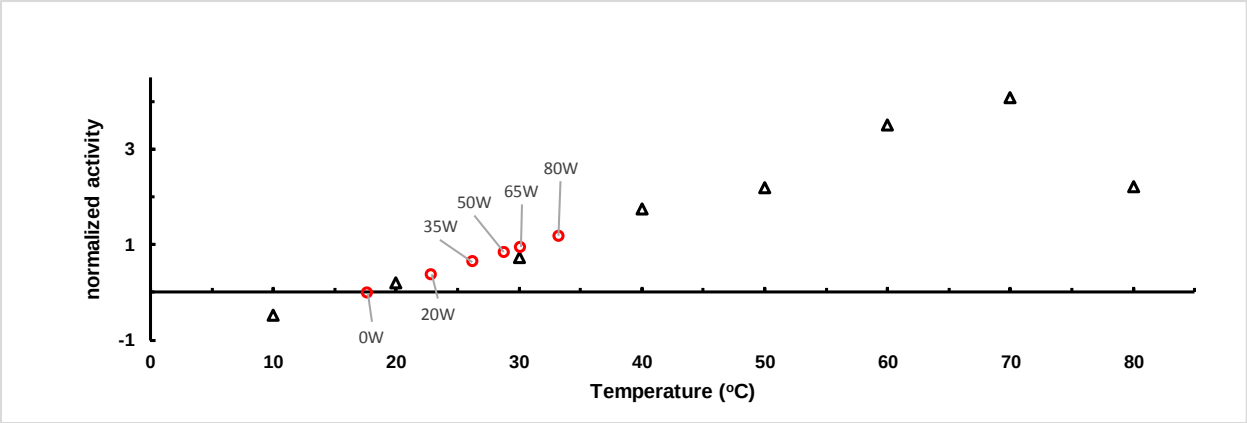

Figure 5.4. Plot of normalized activity of thermolysin as a function of temperature (black triangles) vs applied power (red circles). The zero point on the activity axis was set to the temperature of the solenoid without an RF field on.

Figure 5.4 plots the activity of thermolysin as a function of solution temperature. We observe the expected Arrhenius relationship between temperature and enzyme rate (k), from 10°C to 70°C. At 80°C, the enzyme rate decreases, which we attribute to partial thermal denaturation (Figure 5.4, black triangles). We observe a strikingly similar relationship for activity as a function of incident power (Figure 5.4, red circles). At 80 W the in 17°C solution temperature conjugates perform as if they are in ~16°C warmer solution temperature.

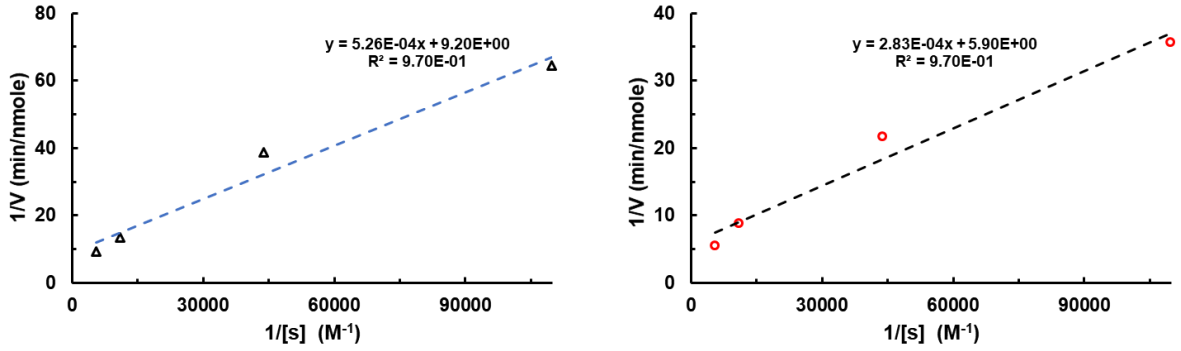

Figure 5.5. Double reciprocal plot of kinetics data, RF heated sample at 50W is in red circles (right), without RF at the same temperature is the black triangles (left). From the intercept and slope we determined K_m and V_{max} and k_{cat}.

We further investigated the enzyme kinetics of RF irradiated thermolysin/NP conjugates with concurrent controls identical in experimental setup except for the RF irradiation. Velocities were measured for various substrate concentrations. The results were analyzed with the Michaelis-Menten model of enzyme kinetics.[33–36] Figure 5.5 shows a double-reciprocal (e.g. Lineweaver-Burke plot, see appendix C6 pg 155). Analysis through equation 5.1 of this data produces the values for maximum enzyme velocity (V_{max}), Michaelis constant (K_M), and K_{cat}.

$$\frac{1}{v} = \frac{K_M}{V_{max}\,[s]} + \frac{1}{V_{max}} \tag{5.1}$$

These values are tabulated in Table 5.1. Under RF irradiation, the V_{max} of thermolsyin/NP conjugates increase relative to the same sample in the absence of RF. We rationalize this by considering that transition states will be more stable (higher thermal energy results in lower activation energy barriers which speeds any reaction up.[37] More curiously, we observe a decrease in K_M in radiofrequency fields. This may be understood through an examination of the thermolysin mechanism. Thermolysin most likely utilizes an induced fit mechanism of activity in which substrate molecules induces conformational changes in thermolysin that help it stabilize transition states.[38] Under typical heating conditions, global temperature increases the floppiness of the enzyme and substrate resulting in a smearing of states of the enzyme and substrate from the ideal state, but allows for more sampling of states.

	RF	control
V_{max} (nmole/min)	0.169 ± 0.059	0.109 ± 0.044
K_m (μM)	48.0 ± 6.0	57.2 ± 6.8
k_{cat} (min^{-1})	$2.1*10^{-4}$	$1.4*10^{-4}$

Table 5.1. Summary of kinetics data for Michaelis Menten kinetics model.

The decrease in K_M (e.g., increase in substrate affinity) that occurs as a result of RF heating can be rationalized in terms of the enzymatic mechanism. Thermolysin active site structure is modified by the substrate – an induced fit.[38,39] The substrate induced conformational changes in thermolysin structure stabilize the proteolytic transition state. Higher temperatures increase the rate of conformational sampling that the enzyme does in making an induced fit.[37,40,41] However, higher temperatures also increase the conformational sampling of the substrate, making induced fit less likely. In terms of the Michaelis-Menten model (equation 5.2), higher temperatures increase both k_1 and k_{-1}. In bulk heating experiments K_M is temperature independent because increased temperatures influence the forward and backward rates equally.

$$E + S \underset{k_{-1}}{\overset{k_1}{\rightleftharpoons}} ES \xrightarrow{k_{cat}} E + P \qquad (5.2)$$

In the radio frequency fields, the enzyme is closer to the heat source than the substrate. Thus, the enzyme is sampling conformational space at a faster rate than the more rigid substrate. We suggest that this situation of 'hot enzyme, cold substrate' allows for a more rapid induced fit the enzyme is being heated results in additional floppiness of the enzyme, allowing for an easier induced fit of the substrate molecule. This results in higher k_1 because the substrate is docking with a floppier enzyme

(allowing for best confirmation more easily) and then lower k_{-1} because the substrate is held more firmly once its attached because of this same improvement in induced fit through enzyme floppiness.

5.4 Conclusions

We have successfully shown that thermolysin can be remotely activated in 17.76 MHz RF fields when covalently attached to magnetic nanoparticles. Without raising the bulk solution temperature, under RF irradiation we observed enzyme activity as if the solution was 16 $\pm$ 2 °C warmer, or an increase in enzymatic rate of 56 $\pm$ 8%. Further studies will be performed with higher field strengths to maximize the level of activation in RF fields. A preliminary investigation of the kinetics in and outside of the RF fields showed an increase in activity consistent with a hot enzyme interacting with a cold substrate. Our approach for remote control of enzyme activity seems to be universally applicable to any enzyme that has an induced fit mechanism of activity, but more investigation into the scope of this process is necessary.

REFERENCES

1. Clark, D. P.; Pazdernik, N. J. Chapter E6 - Polymerase Chain Reaction. In *Molecular Biology (Second Edition)*; Academic Press: Boston, 2013; pp e55–e61.

2. Sun, W. Chapter 4 - Nucleic Extraction and Amplification. In *Molecular Diagnostics*; Grody, C. W., Nakamura, R. M., Strom, C. M., Kiechle, F. L., Eds.; Academic Press: San Diego, 2010; pp 35–47.

3. Butler, J. M. Chapter 4 - PCR Amplification: Capabilities and Cautions. In *Advanced Topics in Forensic DNA Typing: Methodology*; Academic Press: San Diego, 2012; pp 69–97.

4. Arya, M.; Shergill, I. S.; Williamson, M.; Gommersall, L.; Arya, N.; Patel, H. R. Basic Principles of Real-Time Quantitative PCR. *Expert Rev. Mol. Diagn.* **2005**, *5* , 209–219.

5. Najafov, A.; Hoxhaj, G. Chapter 1 - Introduction. In *PCR Guru*; Academic Press, 2017; pp 1–6.

6. van der Zee, J. Heating the Patient: A Promising Approach? *Ann. Oncol. Off. J. Eur. Soc. Med. Oncol.* **2002**, *13*, 1173–1184.

7. Hildebrandt, B.; Wust, P.; Ahlers, O.; Dieing, A.; Sreenivasa, G.; Kerner, T.; Felix, R.; Riess, H. The Cellular and Molecular Basis of Hyperthermia. *Crit. Rev. Oncol. Hematol.* **2002**, *43*, 33–56.

8. Wust, P.; Hildebrandt, B.; Sreenivasa, G.; Rau, B.; Gellermann, J.; Riess, H.; Felix, R.; Schlag, P. M. Hyperthermia in Combined Treatment of Cancer. *Lancet Oncol.* **2002**, *3*, 487–497.

9. Falk, M. H.; Issels, R. D. Hyperthermia in Oncology. *Int. J. Hyperth. Off. J. Eur. Soc. Hyperthermic Oncol. North Am. Hyperth. Group* **2001**, *17*, 1–18.

10. Glazer, E. S.; Curley, S. A. The Ongoing History of Thermal Therapy for Cancer. *Surg. Oncol. Clin. N. Am.* **2011**, *20*, 229–235.

11. Meselson, M.; Yuan, R. DNA Restriction Enzyme from E. Coli. *Nature* **1968**, *217*, 1110–1114.

12. Stephenson, F. H. Chapter 10 - Recombinant DNA. In *Calculations for Molecular Biology and Biotechnology (Third Edition)*; Academic Press: Boston, 2016; pp 321–373.

13. Pelley, J. W. 18 - Recombinant DNA and Biotechnology. In *Elsevier's Integrated Biochemistry*; Mosby: Philadelphia, 2007; pp 159–167.

14. Hamad-Schifferli, K.; Schwartz, J. J.; Santos, A. T.; Zhang, S.; Jacobson, J. M. Remote Electronic Control of DNA Hybridization through Inductive Coupling to an Attached Metal Nanocrystal Antenna. *Nature* **2002**, *415*, 152–155.

15. Suzuki, M.; Aki, A.; Mizuki, T.; Maekawa, T.; Usami, R.; Morimoto, H. Encouragement of Enzyme Reaction Utilizing Heat Generation from Ferromagnetic Particles Subjected to an AC Magnetic Field. *Plos One* **2015**, *10*, 11.

16. Knecht, L. D.; Ali, N.; Wei, Y.; Hilt, J. Z.; Daunert, S. Nanoparticle-Mediated Remote Control of Enzymatic Activity. *ACS Nano* **2012**, *6*, 9079–9086.

17. Blankschien, M. D.; Pretzer, L. A.; Huschka, R.; Halas, N. J.; Gonzalez, R.; Wong, M. S. Light-Triggered Biocatalysis Using Thermophilic Enzyme–Gold Nanoparticle Complexes. *ACS Nano* **2013**, *7*, 654–663.

18. Dutz, S.; Hergt, R. Magnetic Nanoparticle Heating and Heat Transfer on a Microscale: Basic Principles, Realities and Physical Limitations of Hyperthermia for Tumour Therapy. *Int. J. Hyperthermia* **2013**, 1–11.

19. Merabia, S.; Shenogin, S.; Joly, L.; Keblinski, P.; Barrat, J.-L. Heat Transfer from Nanoparticles: A Corresponding State Analysis. *Proc. Natl. Acad. Sci.* **2009**, *106*, 15113–15118.

20. Rosensweig, R. E. Heating Magnetic Fluid with Alternating Magnetic Field. *J. Magn. Magn. Mater.* **2002**, *252*, 370–374.

21. Adhikary, K.; Banerjee, M. A Thermofluid Analysis of the Magnetic Nanoparticles Enhanced Heating Effects in Tissues Embedded with Large Blood Vessel during Magnetic Fluid Hyperthermia. *J. Nanoparticles* **2016**, *2016*, e6309231.

22. Armijo, L. M.; Brandt, Y. I.; Mathew, D.; Yadav, S.; Maestas, S.; Rivera, A. C.; Cook, N. C.; Withers, N. J.; Smolyakov, G. A.; Adolphi, N. L.; et al. Iron Oxide Nanocrystals for Magnetic Hyperthermia Applications. *Nanomaterials* **2012**, *2* (4), 134–146.

23. Bakoglidis, K. D.; Simeonidis, K.; Sakellari, D.; Stefanou, G.; Angelakeris, M. Size-Dependent Mechanisms in AC Magnetic Hyperthermia Response of Iron-Oxide Nanoparticles. *IEEE Trans. Magn.* **2012**, *48*, 1320–1323.

24. Deatsch, A. E.; Evans, B. A. Heating Efficiency in Magnetic Nanoparticle Hyperthermia. *J. Magn. Magn. Mater.* **2014**, *354*, 163–172.

25. Dahlquist, F. W.; Long, J. W.; Bigbee, W. L. Role of Calcium in the Thermal Stability of Thermolysin. *Biochemistry (Mosc.)* **1976**, *15*, 1103–1111.

26. Matsubara, H. Observations on the Specificity of Thermolysin with Synthetic Peptides. *Biochem. Biophys. Res. Commun.* **1966**, *24*, 427–430.

27. Blumberg, S.; Holmquist, B.; Vallee, B. L. Reversible Inactivation and Superactivation by Covalent Modification of Thermolysin. *Biochem. Biophys. Res. Commun.* **1973**, *51*, 987–992.

28. Ackerson, C. J.; Jadzinsky, P. D.; Kornberg, R. D. Thiolate Ligands for Synthesis of Water-Soluble Gold Clusters. *J. Am. Chem. Soc.* **2005**, *127*, 6550–6551.

29. Robinson, I.; Tung, L. D.; Maenosono, S.; Wälti, C.; Thanh, N. T. K. Synthesis of Core-Shell Gold Coated Magnetic Nanoparticles and Their Interaction with Thiolated DNA. *Nanoscale* **2010**, *2*, 2624–2630.

30. WangWang; Luo, J.; Fan, Q.; Suzuki, M.; Suzuki, I. S.; Engelhard, M. H.; Lin, Y.; Kim, N.; Wang, J. Q.; Zhong, C.-J. Monodispersed Core−Shell Fe3O4@Au Nanoparticles. *J. Phys. Chem. B* **2005**, *109*, 21593–21601.

31. Ackerson, C. J.; Jadzinsky, P. D.; Sexton, J. Z.; Bushnell, D. A.; Kornberg, R. D. Synthesis and Bioconjugation of 2 and 3 Nm-Diameter Gold Nanoparticles. *Bioconjug. Chem.* **2010**, *21*, 214–218.

32. Heinecke, C.; Ackerson, C. Preparation of Gold Nanocluster Bioconjugates for Electron Microscopy. In *Nanoimaging*; Sousa, A. A., Kruhlak, M. J., Eds.; Methods in Molecular Biology; Humana Press, 2013; pp 293–311.

33. Cornish-Bowden, A. One Hundred Years of Michaelis–Menten Kinetics. *Perspect. Sci.* **2015**, *4*, 3–9.

34. Bhagavan, N. V.; Ha, C.-E. Chapter 6 - Enzymes and Enzyme Regulation. In *Essentials of Medical Biochemistry*; Academic Press: San Diego, 2011; pp 47–58.

35. Jia, H.; Zhu, G.; Wang, P. Catalytic Behaviors of Enzymes Attached to Nanoparticles: The Effect of Particle Mobility. *Biotechnol. Bioeng.* **2003**, *84*, 406–414.

36. Wong, J. F.; Simmons, C. A.; Young, E. W. K. Chapter 3 - Modeling and Measurement of Biomolecular Transport and Sensing in Microfluidic Cell Culture and Analysis Systems. In *Modeling of Microscale Transport in Biological Processes*; Becker, S. M., Ed.; Academic Press, 2017; pp 41–75.

37. Elias, M.; Wieczorek, G.; Rosenne, S.; Tawfik, D. S. The Universality of Enzymatic Rate–temperature Dependency. *Trends Biochem. Sci.* **2014**, *39*, 1–7.

38. Murray, C. W.; Baxter, C. A.; Frenkel, A. D. The Sensitivity of the Results of Molecular Docking to Induced Fit Effects: Application to Thrombin, Thermolysin and Neuraminidase. *J. Comput. Aided Mol. Des.* **1999**, *13*, 547–562.

39. Inouye, K.; Lee, S.-B.; Nambu, K.; Tonomura, B. Effects of PH, Temperature, and Alcohols on the Remarkable Activation of Thermolysin by Salts. *J. Biochem. (Tokyo)* **1997**, *122*, 358–364.

40. Arcus, V. L.; Prentice, E. J.; Hobbs, J. K.; Mulholland, A. J.; Van der Kamp, M. W.; Pudney, C. R.; Parker, E. J.; Schipper, L. A. On the Temperature Dependence of Enzyme-Catalyzed Rates. *Biochemistry (Mosc.)* **2016**, *55*, 1681–1688.

41. Siddiqui, K. S. Some like It Hot, Some like It Cold: Temperature Dependent Biotechnological Applications and Improvements in Extremophilic Enzymes. *Biotechnol. Adv.* **2015**, *33*, 1912–1922.

APPENDIX A: SUPPLEMENTAL TO CHAPTER 3

A.1 Buffer Conditions for CE and RF heating:

Table A.S1. Buffer information for capillary electrophoresis and radiofrequency heating experiments

pH	Acid (10 mM)	Tris [mM]	ionic strength	conductivity
3	citric	3.3	4.523	$5.88*10^{-2}$ S/m
5	glutamic	8.4	8.358	$4.10*10^{-2}$ S/m
7	HEPES	2.7	2.501	$1.20*10^{-2}$ S/m
9	CHES	21	2.319	$1.16*10^{-2}$ S/m

*These conductivities, ionic strength and amounts were all calculated using the program peak master.

Table A.S2. Glutathione pka based on acid base properties (free glutathione data used for this):

		pH 3	pH 5	pH 7	pH 9	pKa
Charge per cluster	COO^- 1	18	18	18	18	2.12
	COO^- 2	4.626	18	18	18	3.59
	NH_4^+	18	17.996	17.680	0	8.75
	total	4.626	18.003	18.320	36	

A.2 Ferguson analysis:

Mobility of $Au_{25}(SG)_{18}$ in 1x TBE (pH is 8.3) was determined with gel electrophoresis by measuring the distance the band traveled (retention factor) as a function of gel percentage. To get a precise measurement of the distance image J was used and calibrated to the size of the get mobilities from the start of the well to the darkest part of the band (corresponding to the most cluster). The linear fit of the cluster was then used to extrapolate the free mobility of the clusters. The mobility measured by gel is in good agreement with the mobility found using capillary electrophoresis.

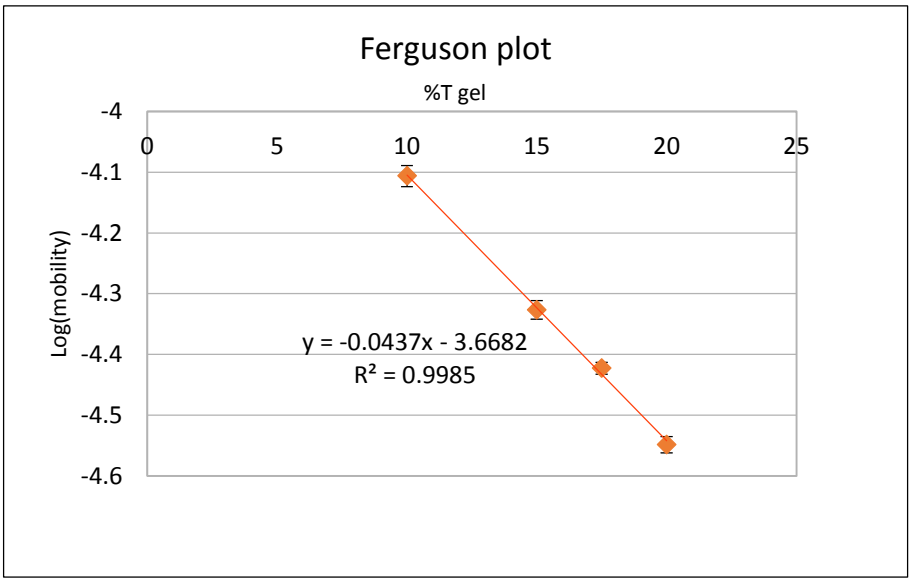

Figure A.S1. Ferguson plot of gel mobilities

From line fit log(M) = log(m0) -kT

Mobility for $Au_{25}(SG)_{18}$ is $10^{-3.6682}$= 0.000215 ± 0.000009 in $cm^2/(Vs)$ (error in intercept is 0.0180)

Capillary electrophoresis gives mobility of $3.86*10^{-4}$ for Au25 at pH 8 and $3.91*10^{-4}$ at pH 8.5 The higher mobility in the gel can be attributed to the increased ionic strength of the 1x TBE the gels are run in, which shrinks the hydrodynamic radius.

Table A.S3. Analysis of Ferguson Plot

	10% acrylamide	**15% acrylamide**	**17.5% acrylamide**	**20% acrylamide**
	Distances measured in imagej			
bottom well (Pixel)	14	8	14.7	12.4
band (most intense) (pixel)	437	267	374.8	277.4
bottom gel (pixel)	719	723	730.4	720
bottom/bottom dist (pixel)	705	715	715.7	707.6
pixles/cm	115.57377	117.213115	117.327869	116
distance band (cm)	3.78±0.15	2.27±0.15	3.19±0.15	2.39±0.15
time (s)	3600	3600	6300	6300
cm/s	0.00105032	0.00063275	0.00050706	0.00037958
field strength V/cm	13.4	13.4	13.4	13.4
Mobility (velocity/field)	7.83E-05± 3.1E-06	4.72E-05± 1.6E-06	3.78E-05± 8.6E-07	2.83E-05± 8.7E-07
Log(mobility)	-4.11±0.069	-4.33±0.015	-4.45±0.010	-4.55±0.014

Gel pictures used to calculate mobilities shown above are seen below: The first two lanes with particles are Au102 and the third lane with particles is the $Au_{25}(SG)_{18}$ sample.

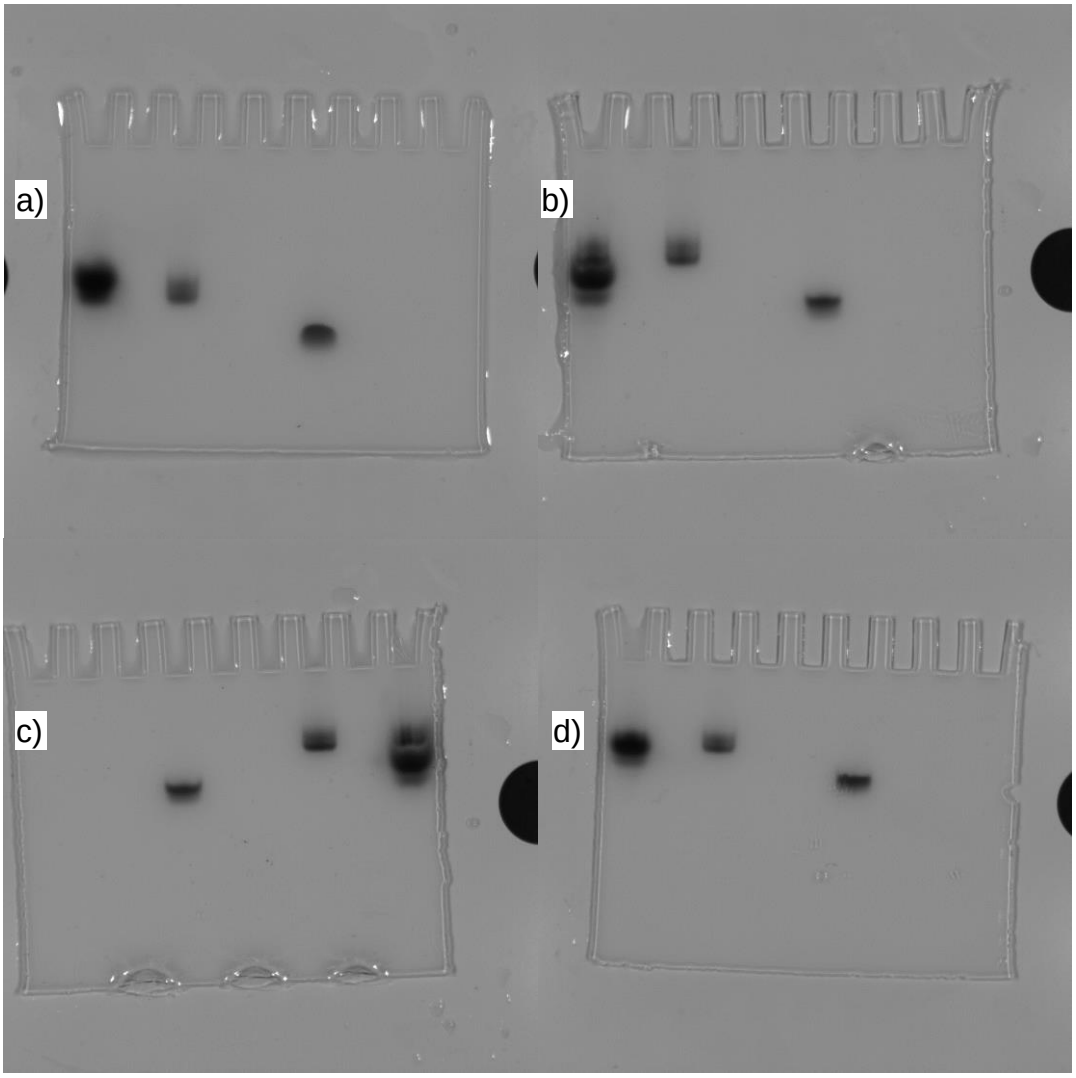

Figure A.S2. Gel images used for Furgeson analysis, a) is 10% gel b) is15% c) is 17.5% and d) is 20%

A.3 DLS of $Au_{25}(SG)_{18}$

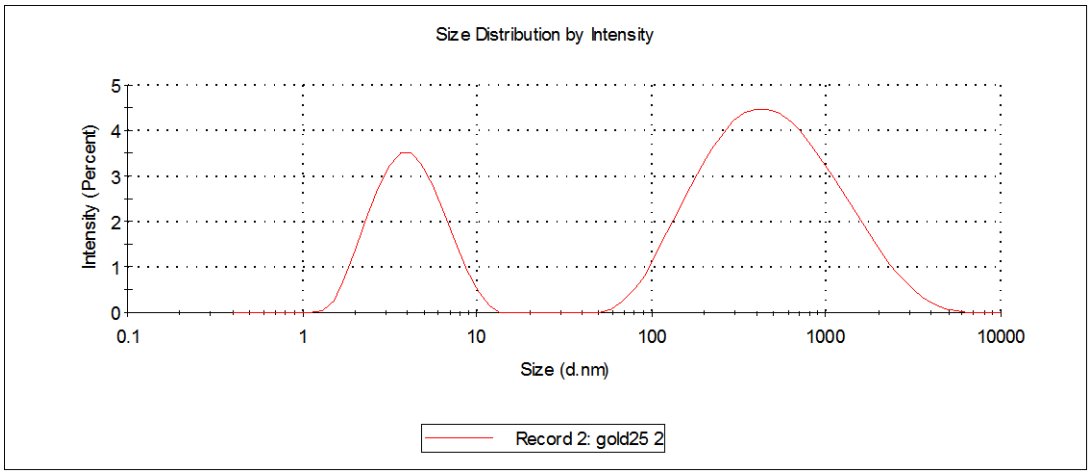

Figure A.S3. Intensity DLS results for $Au_{25}(GS)_{18}$ in pH 5 buffer

By intensity there appears to be something larger in solution as well as the clusters, which at first seemed to be aggregates, but the particles are centrifuged for 40 mins at max speed and filtered before DLS to ensure no aggregates.

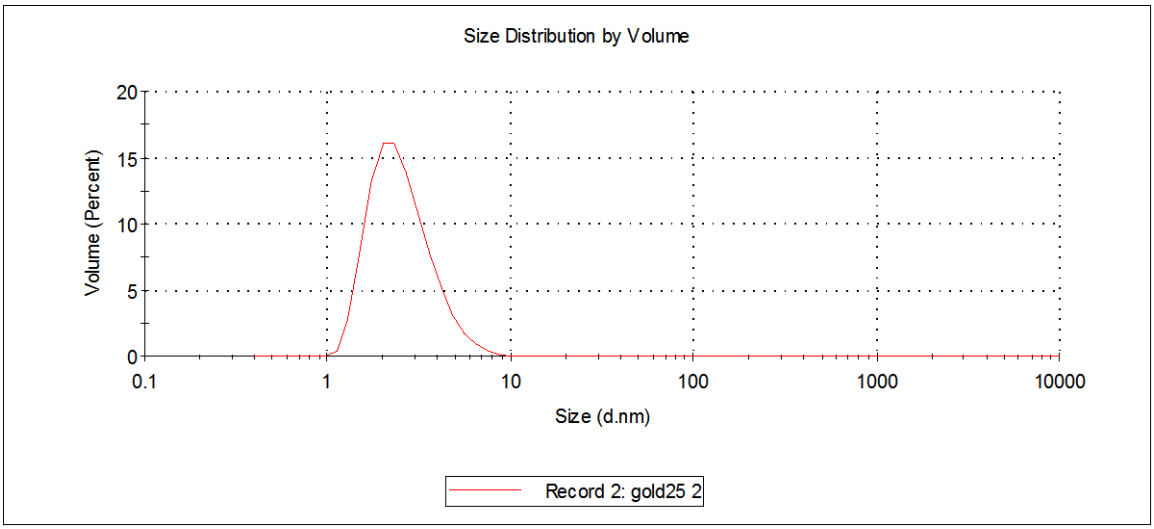

Figure A.S4. volume DLS results for $Au_{25}(GS)_{18}$ in pH 5 buffer

Looking at this in terms of volume or mass shows a relatively monodisperse sample with an average hydrodynamic radius of 1.65 nm with no evidence of the larger peak seen in the intensity plot. If it were an aggregate the size distribution by volume would be very much skewed towards the larger species. This appears to be an artifact

and has been observed previously by another group performing DLS on similarly sized clusters.[1]

A.4 Calculated heating rates:

Calculating water soluble glutathione cluster heating rate using percent of acid deionization based on electrophoretic mobility

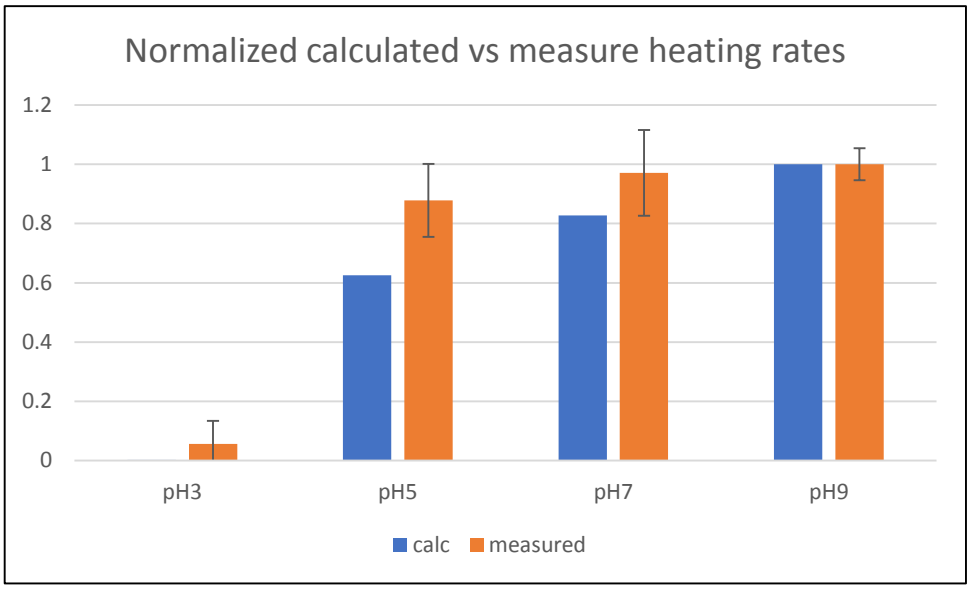

Figure A.S5. Calculated heating rates of glutathione protected cluster using electrophoretic mobility and Sassaroli model of heating, error bars are shown for triplicate measurements

Comparison of normalized calculated heating rate to measured: note they are normalized to the highest calculated and measured value separately. The same radii are assumed for all pH values.

A.5 Capillary electrophoresis data, raw:

Capillary electrophoresis experiments were performed and an HP 61600AX 3DCE, using a 50 μm, 33 cm (24.5cm to the window) fused silica capillary treated with NaOH. It was run with positive polarity with an applied voltage of 15 kV and the temperature of the capillary was held constant at 25*C. Uv-vis absorption at 214, 254

and 280 nm was collected using chemstation software Rev A.08.03. Caffeine was used as a neutral electro osmotic flow indicator. Raw data from the absorbance at 280nm can be seen below. Data was then converted to the mobility domain to better visualize the effect of the pH of the background electrolytes on the electrophoretic mobility of the clusters.

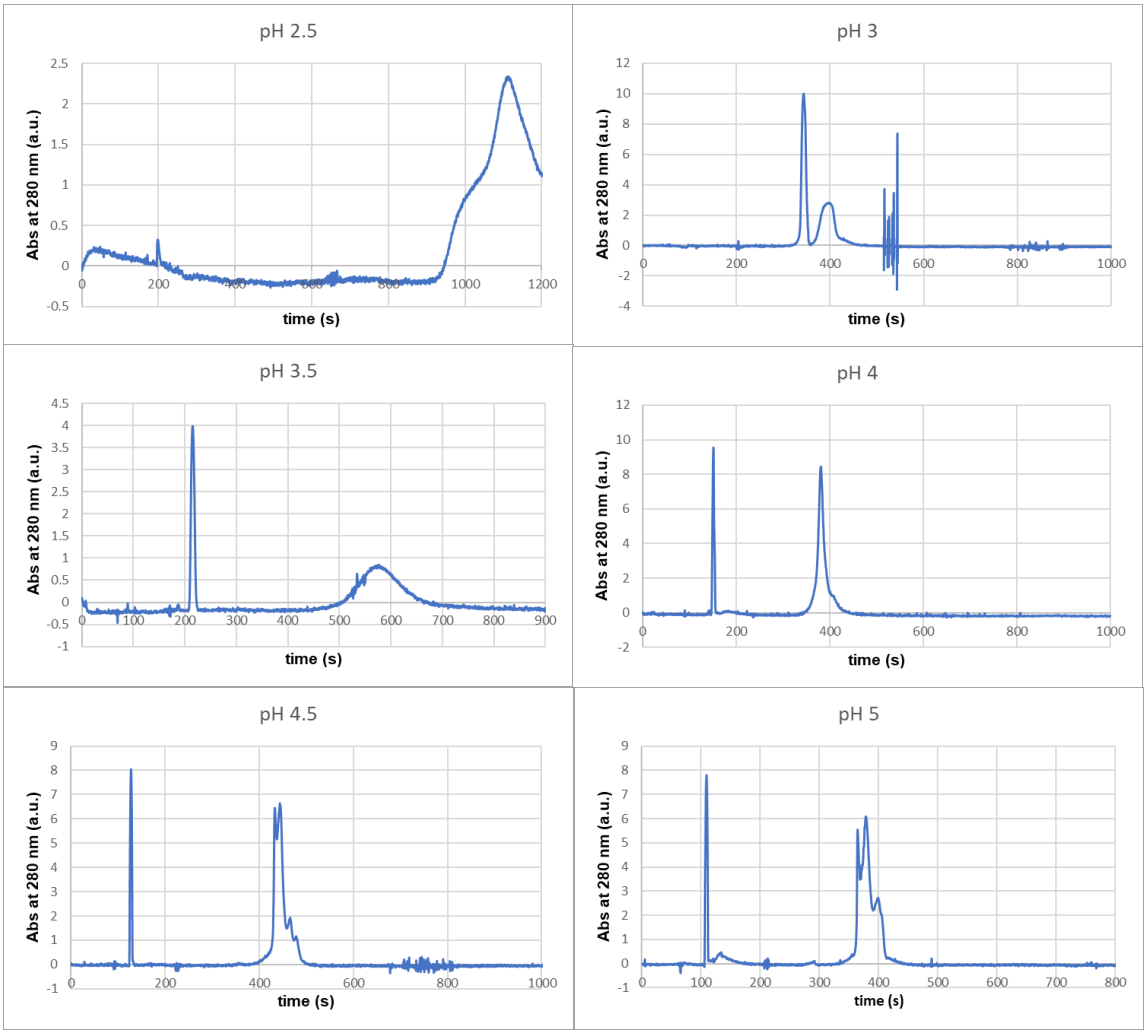

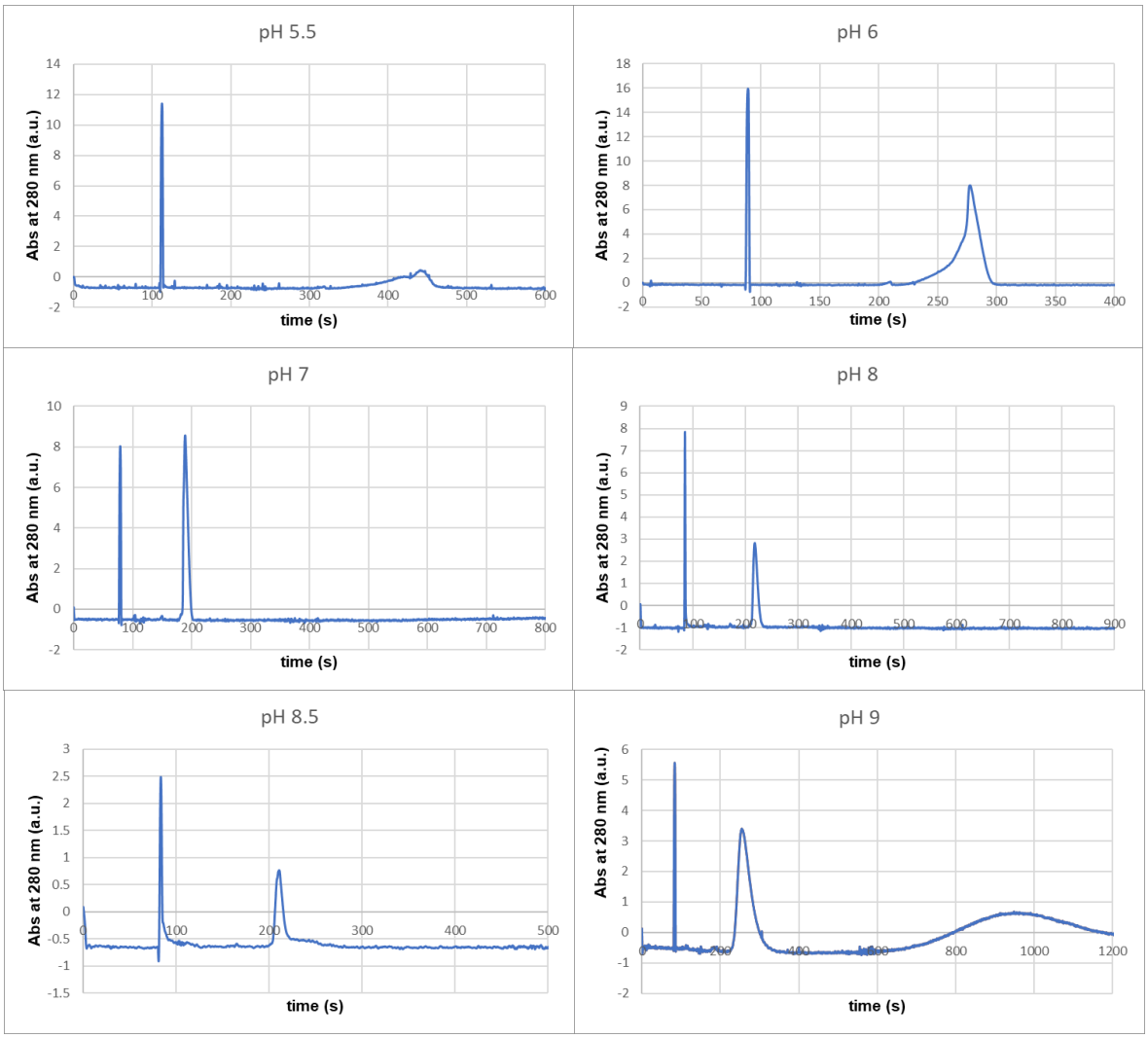

Figure A.S6: Raw capillary electrophoresis data, pH for each run is labeled on the spectrum itself

A.6 Combined CE data in mobility domain:

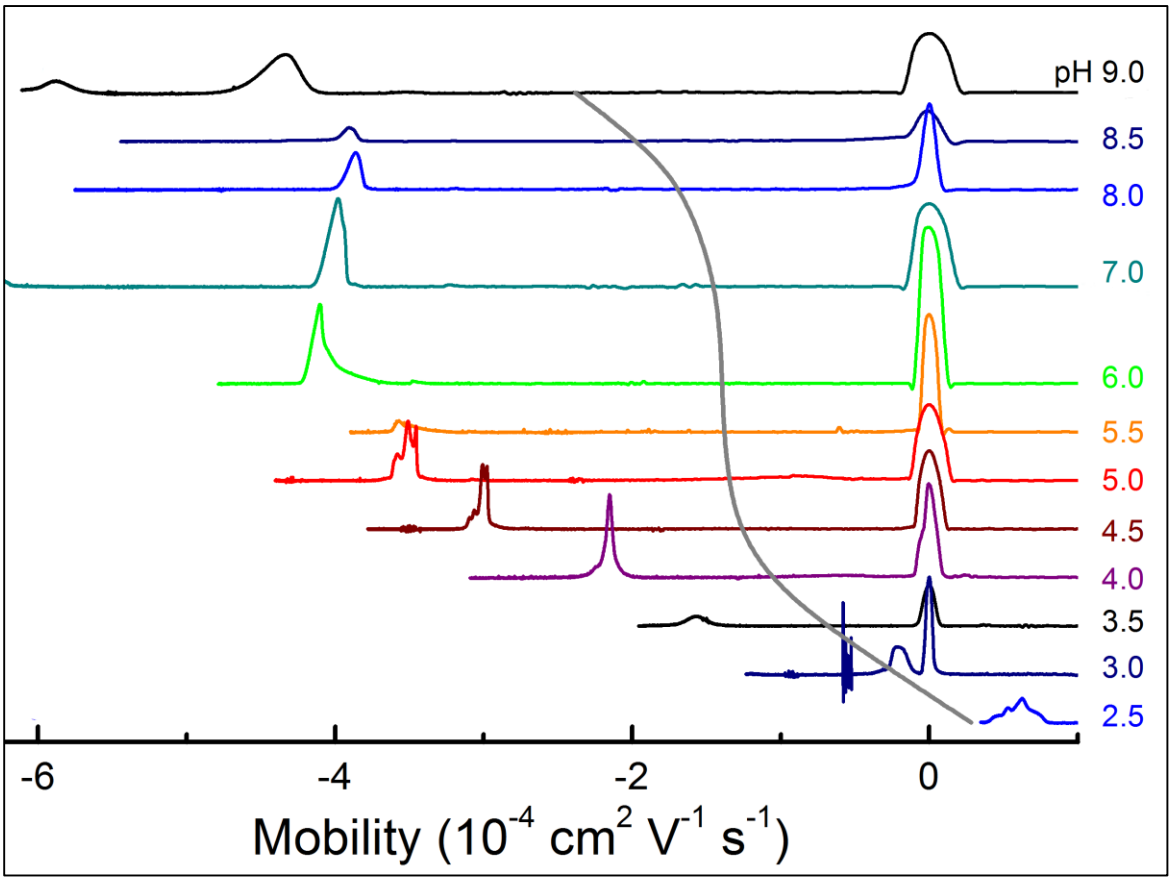

Figure A.S7. Combined electrophoresis data plotted in mobility domain, with grey trace indicating free glutathione mobility (calculated)

A.7 Radiofrequency heating experiments:

2mL Samples were contained in 10mm NMR tube. They were heated in a custom constructed water cooled hollow copper solenoid powered by a 100W amplifier (ifi scx100) and a function generator (Philips PM5192) set to generate a sinusoidal current at 13.56 MHz. An impedance matching network was used and forward voltage from the amplifier was monitored and set at 50W. The temperature of the bullk solution was measure with a fiber optic temperature probe (Neoptix Nomad).

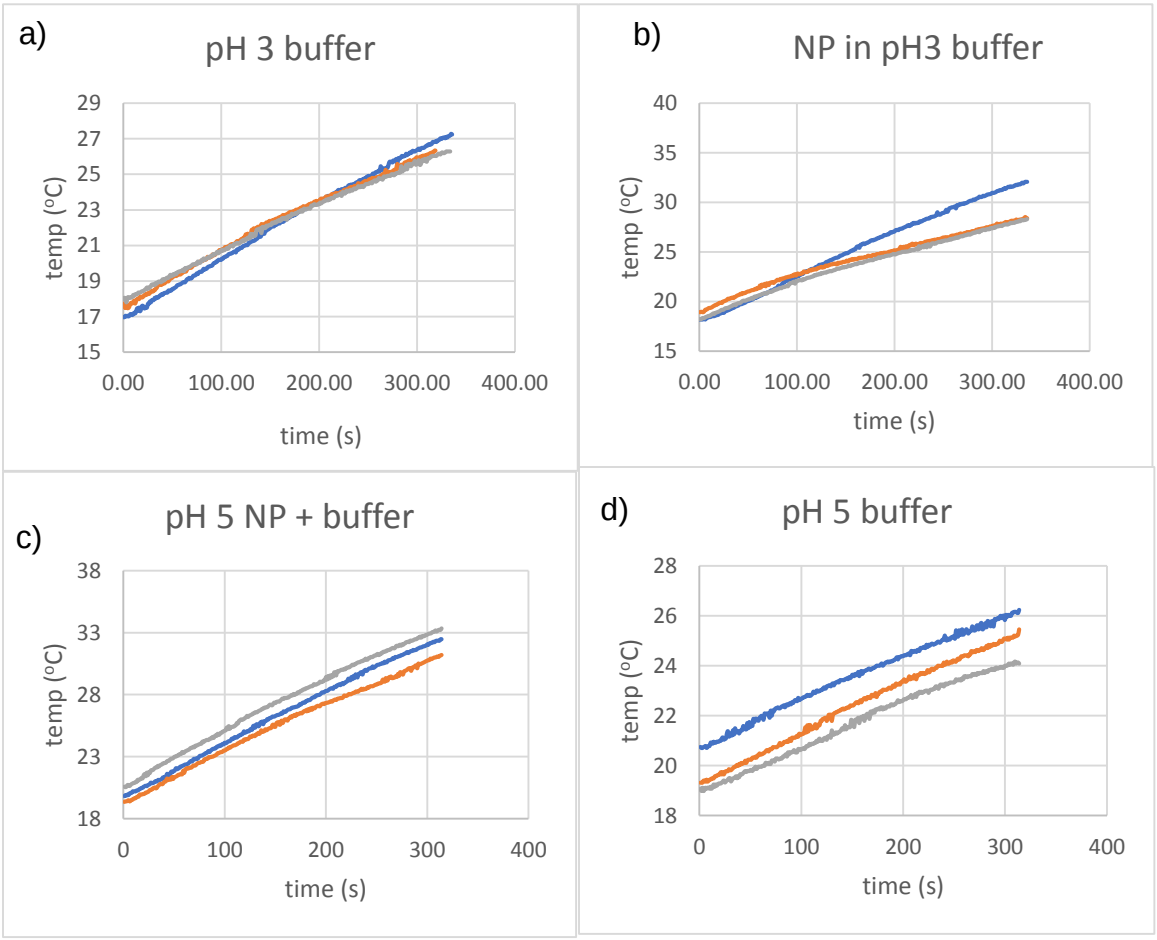

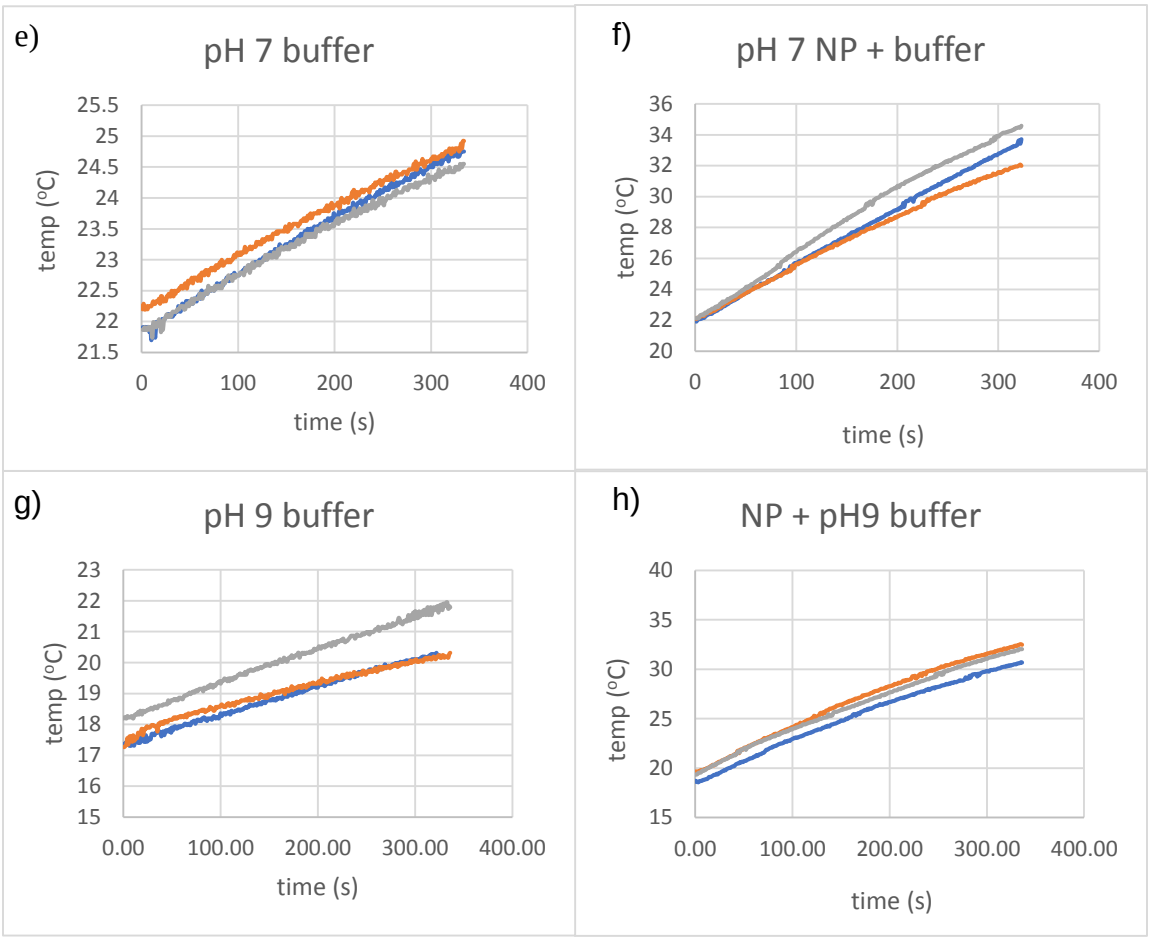

Figure A.S8. Measured heating rates of background buffers and particle solutions

A.8 Concentration study

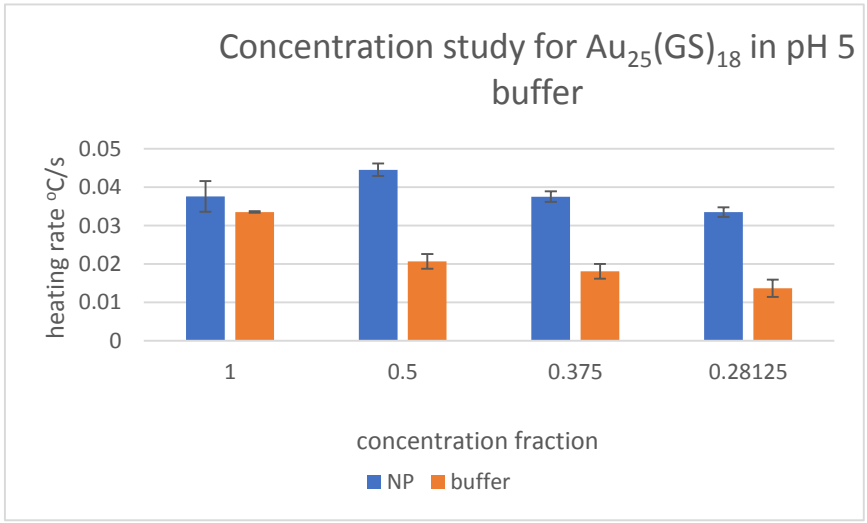

Figure A.S9. Average heating rates for different concentrations of $Au_{25}(GS)_{18}$, error bars represent measurements in triplicate

A.9 Experimental Section

Particle synthesis: $Au_{25}(PET)_{18}$ particles were synthesized in the various charge states, exactly as previously reported.[2] UV-vis spectra for each cluster after purification is seen in figure A.S10. $Au_{25}(GS)_{18}$ was synthesized as previously report.[3] Fractional precipitation was used to clean up the particles prior to purification by PAGE. This allowed more material to be loaded on each gel.

Ferguson analysis: Mobility of $Au_{25}(SG)_{18}$ in 1x TBE (pH is 8.3) was determined with gel electrophoresis by measuring the distance the band traveled (retention factor) as a function of gel percentage. To get a precise measurement of the distance image J was used and calibrated to the size of the get mobilities from the start of the well to the darkest part of the band (corresponding to the most cluster). The linear fit of the cluster was then used to extrapolate the free mobility of the clusters. The mobility measured by gel is in good agreement with the mobility found using capillary electrophoresis.

Capillary electrophoresis: experiments were performed and an HP 61600AX 3DCE, using a 50 μm, 33 cm (24.5 cm to the window) fused silica capillary treated with NaOH. It was run with positive polarity with an applied voltage of 15 kV and the temperature of the capillary was held constant at 25^{o}C. Uv-vis absorption at 214, 254 and 280 nm was collected using chemstation software Rev A.08.03. Caffeine was used as a neutral electro osmotic flow indicator. Raw data from the absorbance at 280nm can be seen below bellow. Data was then converted to the mobility domain to better visualize the effect of the pH of the background electrolytes on the electrophoretic mobility of the clusters.

Radiofrequency heating experiments:

2 mL samples were contained in 10 mm NMR tube. They were heated in a custom constructed water cooled hollow copper solenoid powered by a 100W amplifier (ifi scx100) and a function generator (Philips PM5192) set to generate a sinusoidal current at 13.56 MHz. An impedance matching network was used and forward voltage from the amplifier was monitored and set at 50W. The temperature of the bulk solution was measure with a fiber optic temperature probe (Neoptix Nomad).

A.10 uv-Vis spectra of synthesized gold clusters

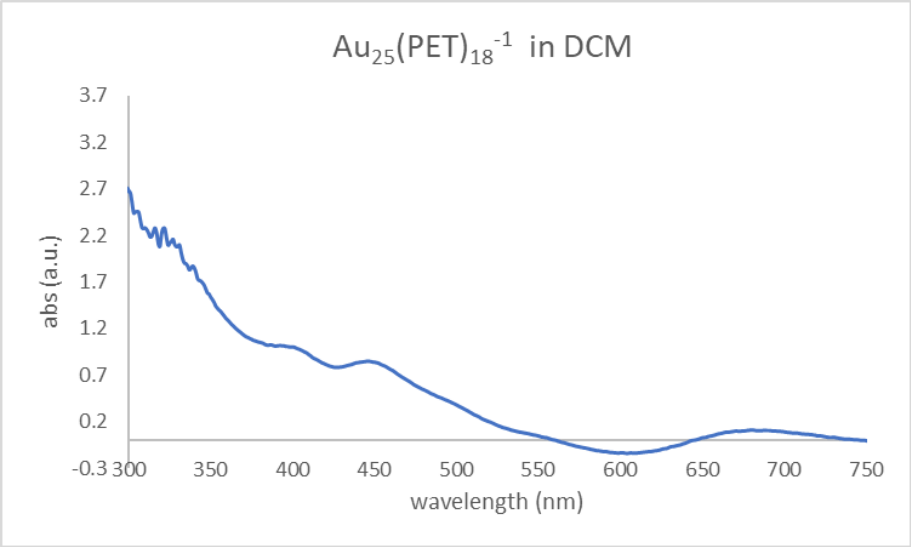

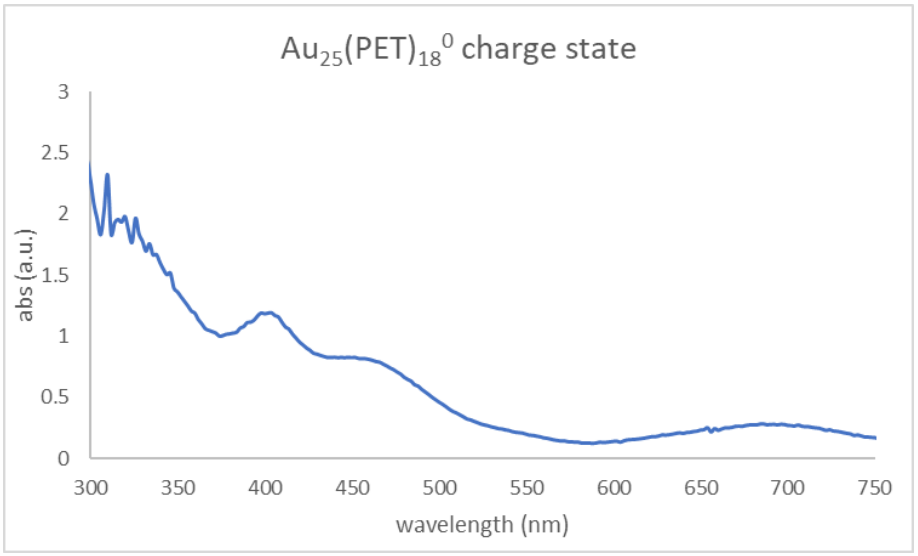

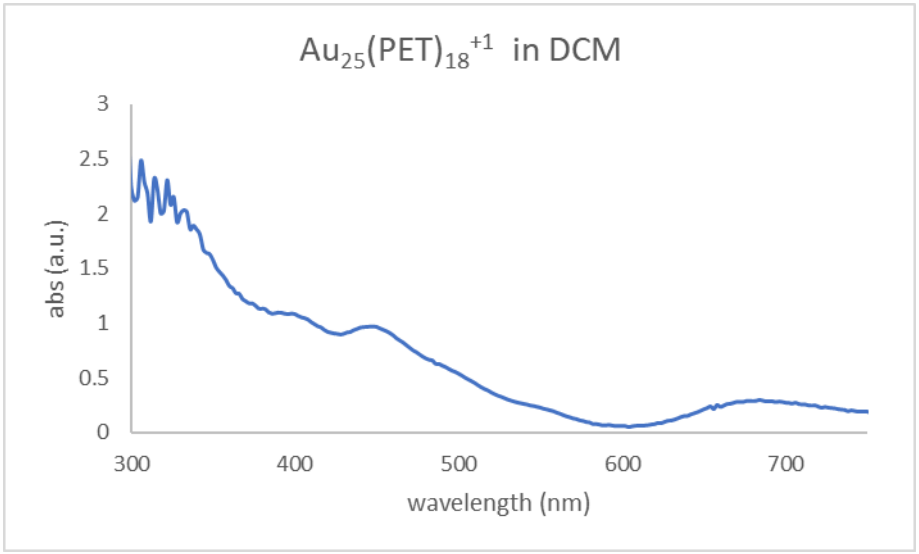

Figure A.S10. Uv-vis spectra of $Au_{25}(PET)_{18}$ clusters in -1,0,+1 charge state

REFERENCES

(1) Hartje, L. F.; Munsky, B.; Ni, T. W.; Ackerson, C. J.; Snow, C. D. Adsorption-Coupled Diffusion of Gold Nanoclusters within a Large-Pore Protein Crystal Scaffold. *J. Phys. Chem. B* **2017**, *121*, 7652–7659.

(2) A. Tofanelli, M.; Salorinne, K.; W. Ni, T.; Malola, S.; Newell, B.; Phillips, B.; Häkkinen, H.; J. Ackerson, C. Jahn–Teller Effects in Au 25 (SR) 18. *Chem. Sci.* **2016**, *7*, 1882–1890.

(3) Dreier, T. A.; Compel, W. S.; Wong, O. A.; Ackerson, C. J. Oxygen's Role in Aqueous Gold Cluster Synthesis. *J. Phys. Chem. C* **2016**, *120*, 28288–28294.

APPENDIX B: SUPPLEMENTAL TO CHAPTER 4

B.1 uv-Vis Spectra for decomposition study

UV/Vis spectra were collected on an HP 8452A Diode Array Spectrophotometer, a ThermoFisher NanoDrop spectrophotometer in all other cases. Data were analyzed using Microsoft Excel.

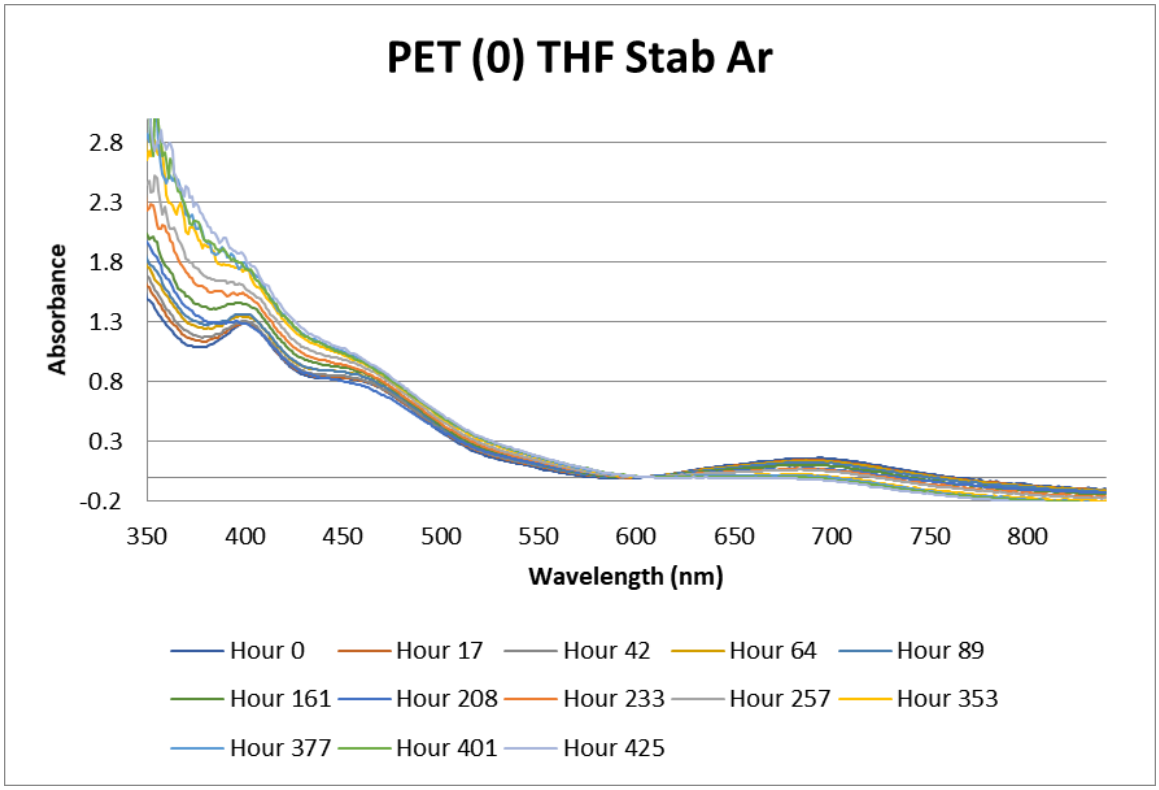

B.1.1 Decomposition in stabilized and unstabilized THF under argon and air

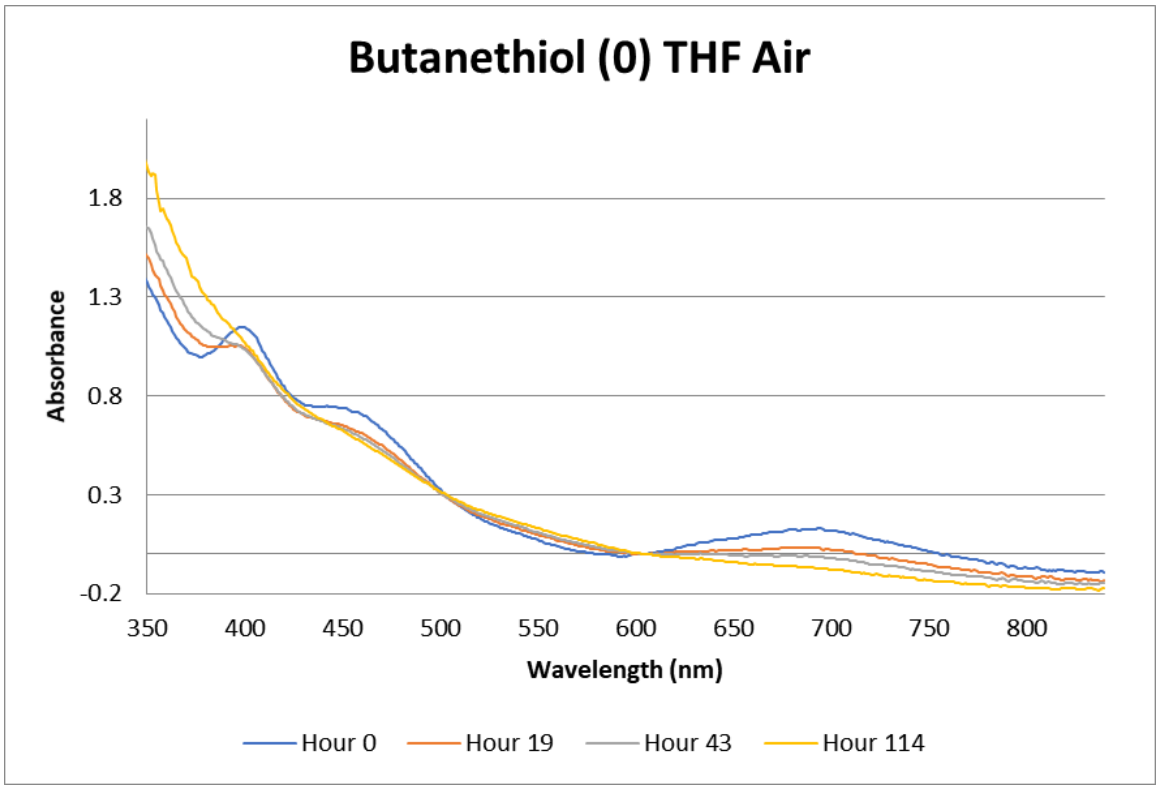
Butanethiol (0) THF Air
Absorbance
1.8
1.3
0.8
0.3
-0.2
350
400
450
500
550
600
650
700
750
800
Wavelength (nm)
Hour 0
Hour 19
Hour 43
Hour 114

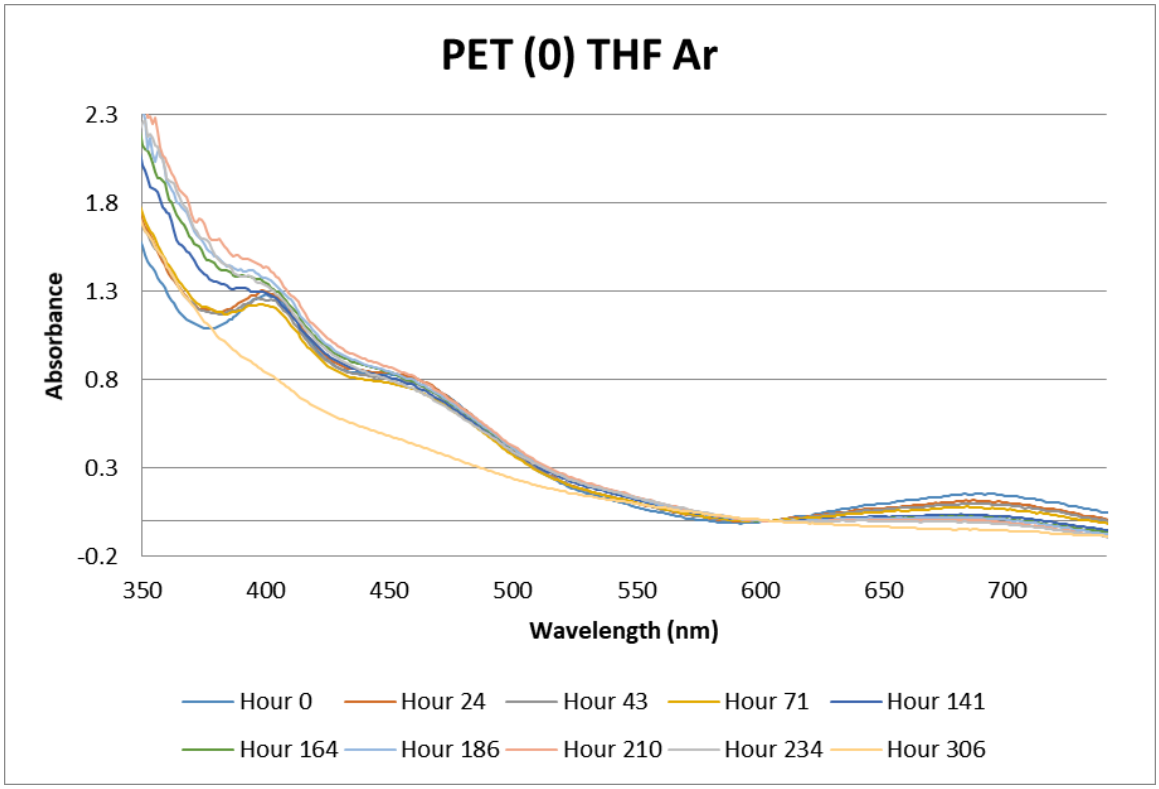
PET (0) THF Ar
Absorbance
2.3
1.8
1.3
0.8
0.3
-0.2
350
400
450
500
550
600
650
700
Wavelength (nm)
Hour 0
Hour 24
Hour 43
Hour 71
Hour 141
Hour 164
Hour 186
Hour 210
Hour 234
Hour 306

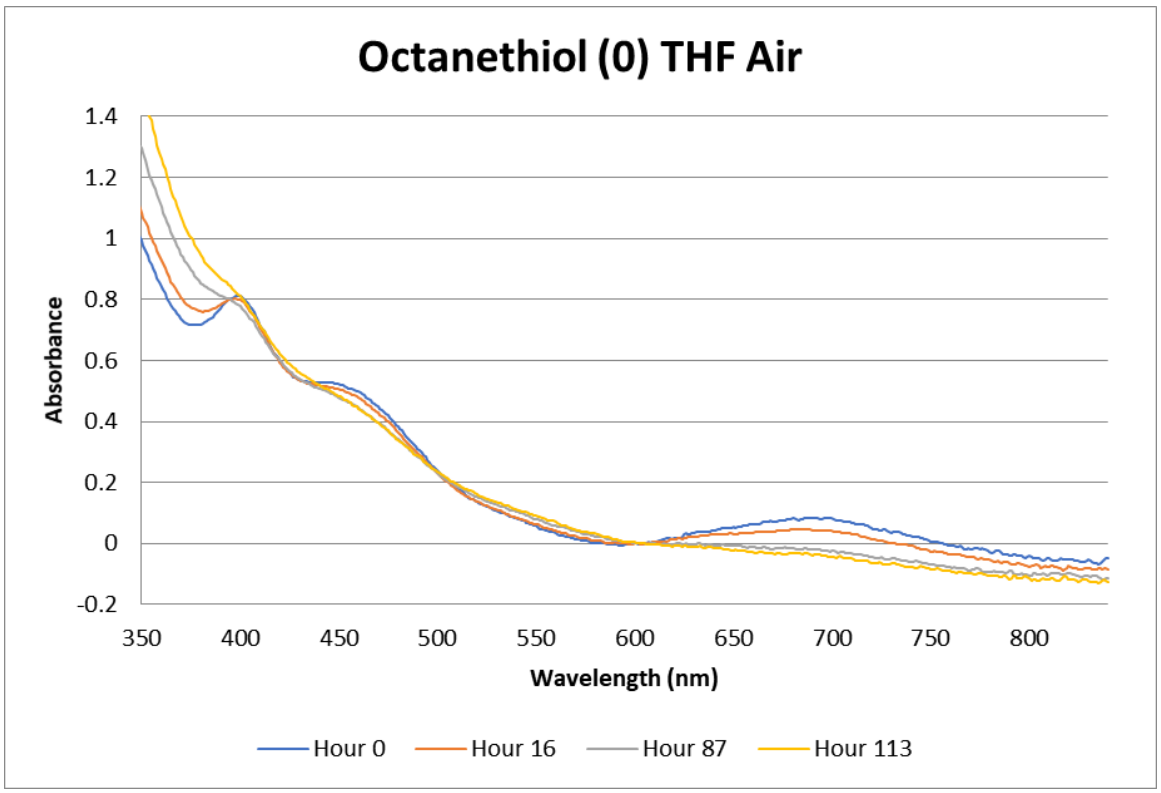
Octanethiol (0) THF Air
Absorbance
1.4
1.2
1
0.8
0.6
0.4
0.2
0
-0.2
350
400
450
500
550
600
650
700
750
800
Wavelength (nm)
Hour 0
Hour 16
Hour 87
Hour 113

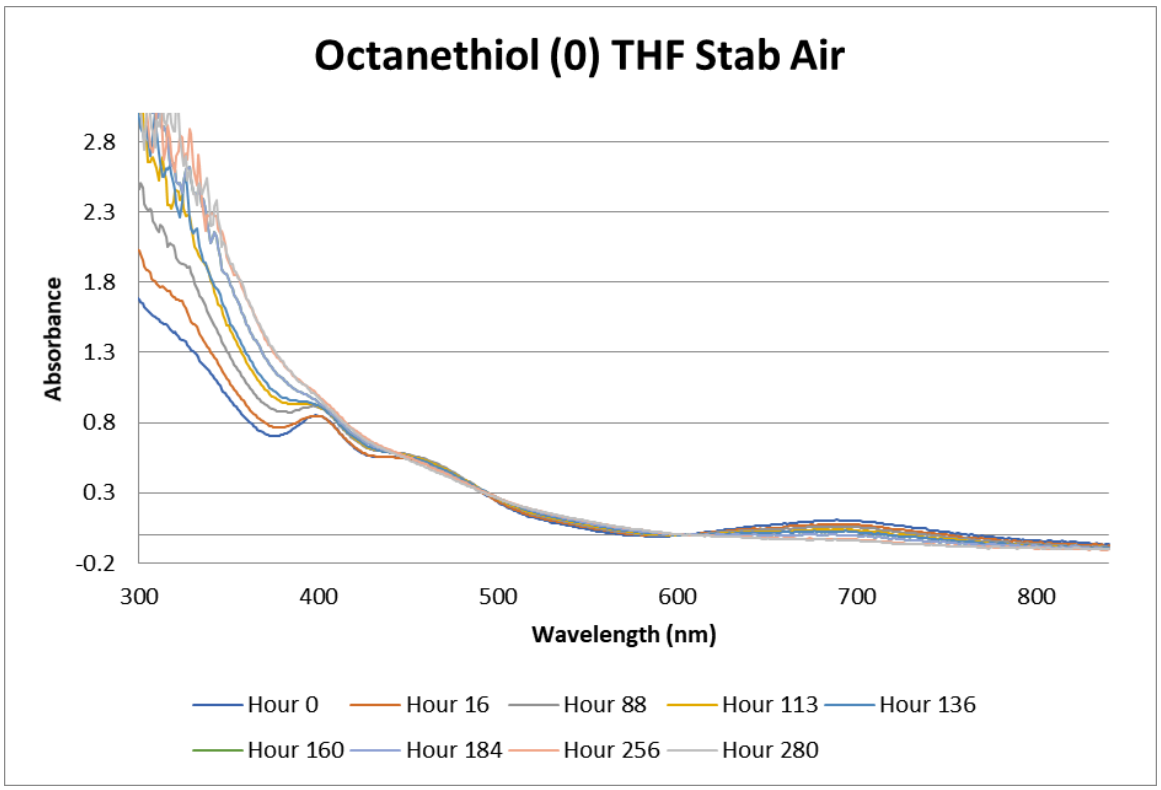
Octanethiol (0) THF Stab Air
Absorbance
2.8
2.3
1.8
1.3
0.8
0.3
-0.2
300
400
500
600
700
800
Wavelength (nm)
Hour 0
Hour 16
Hour 88
Hour 113
Hour 136
Hour 160
Hour 184
Hour 256
Hour 280

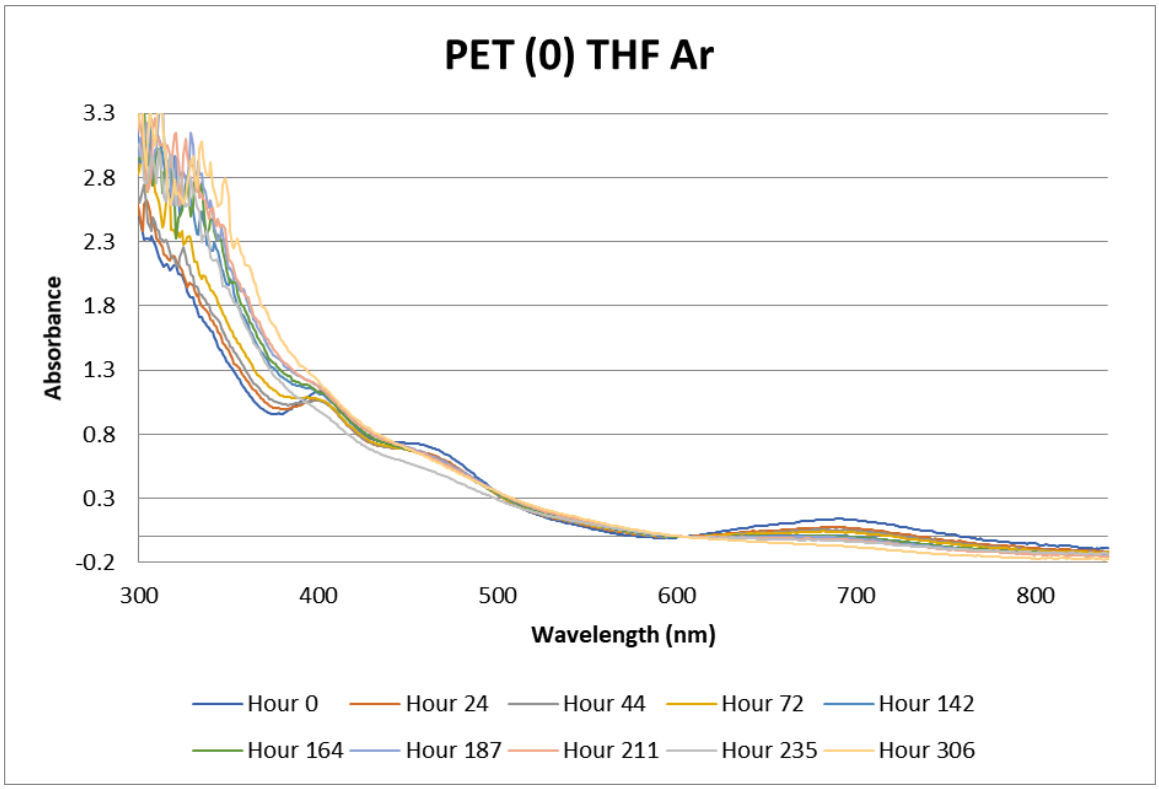
PET (0) THF Ar
Absorbance
3.3
2.8
2.3
1.8
1.3
0.8
0.3
-0.2
300
400
500
600
700
800
Wavelength (nm)
Hour 0
Hour 24
Hour 44
Hour 72
Hour 142
Hour 164
Hour 187
Hour 211
Hour 235
Hour 306

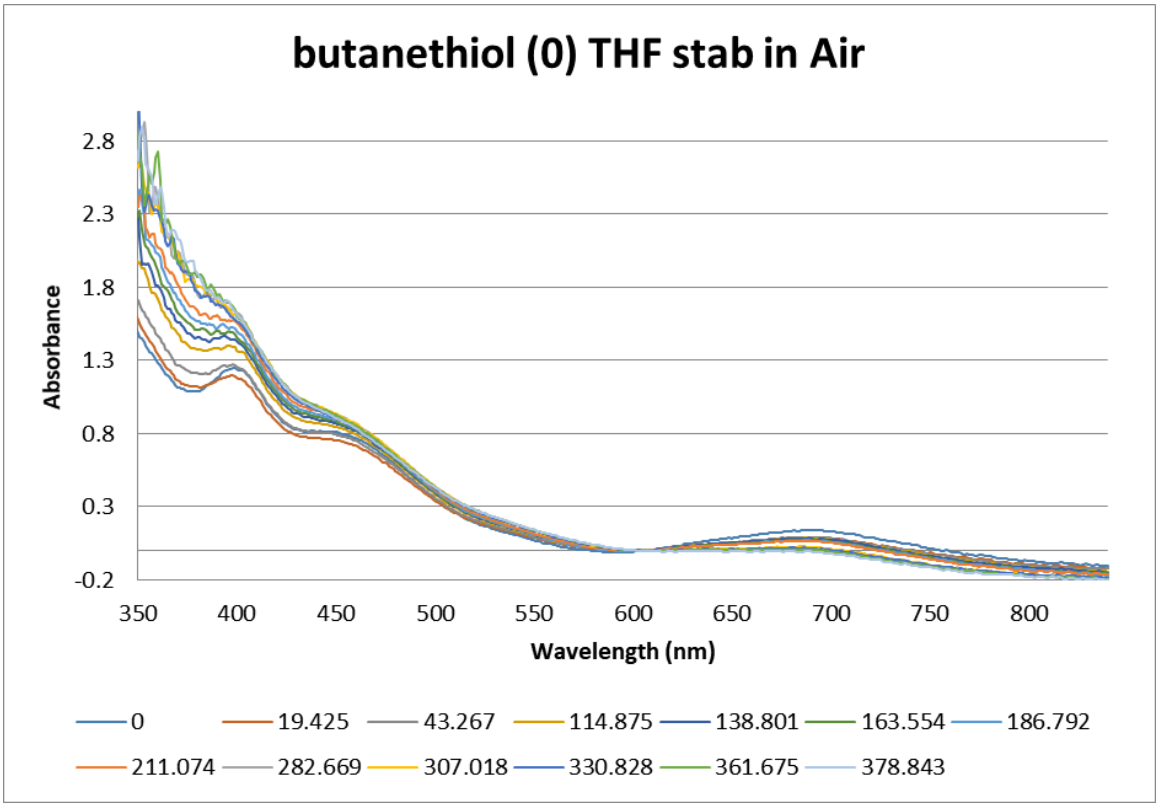
butanethiol (0) THF stab in Air
Absorbance
2.8
2.3
1.8
1.3
0.8
0.3
-0.2
350
400
450
500
550
600
650
700
750
800
Wavelength (nm)
0
19.425
43.267
114.875
138.801
163.554
186.792
211.074
282.669
307.018
330.828
361.675
378.843

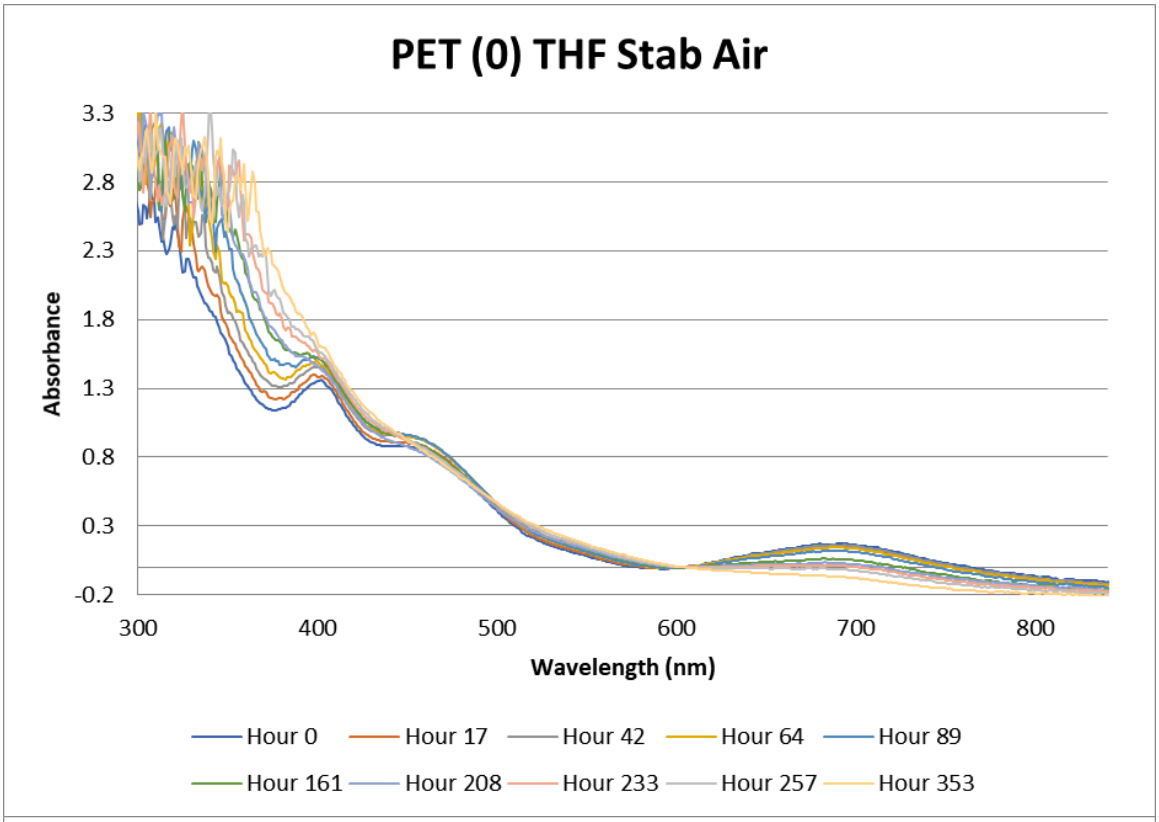
PET (0) THF Stab Air
Absorbance
3.3
2.8
2.3
1.8
1.3
0.8
0.3
-0.2
300
400
500
600
700
800
Wavelength (nm)
Hour 0
Hour 17
Hour 42
Hour 64
Hour 89
Hour 161
Hour 208
Hour 233
Hour 257
Hour 353

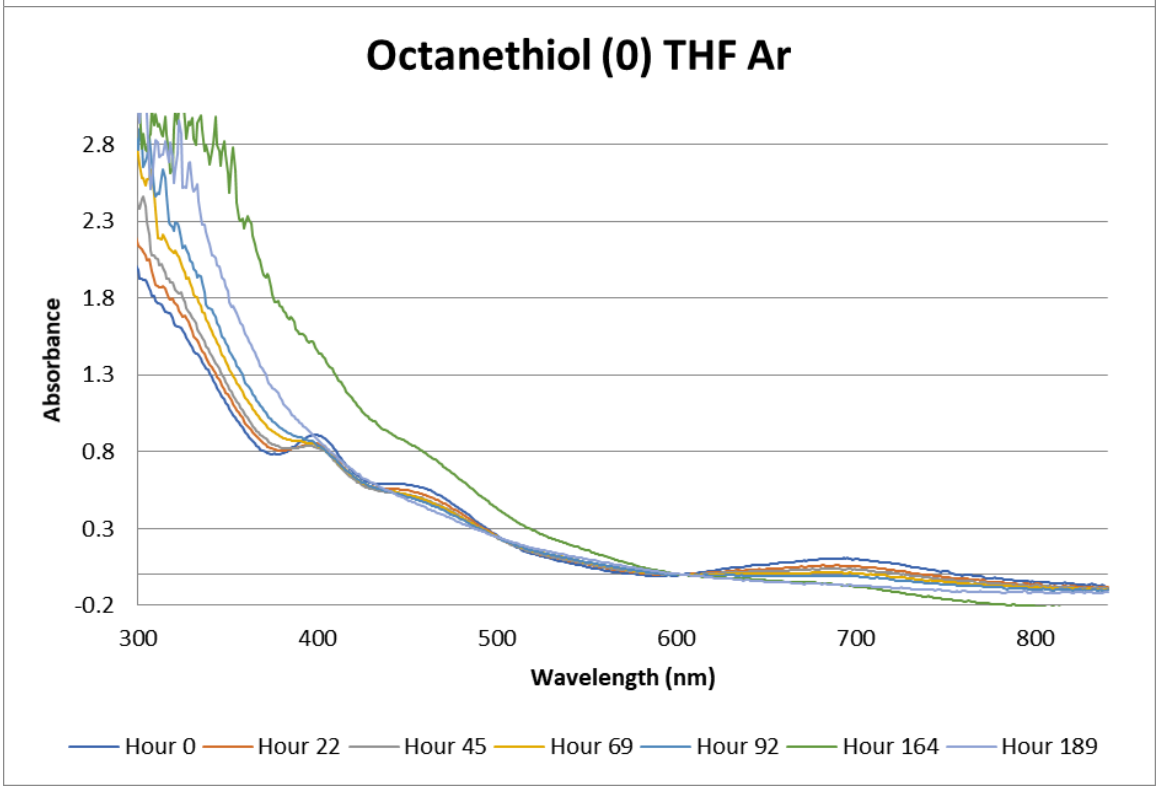
Octanethiol (0) THF Ar
Absorbance
2.8
2.3
1.8
1.3
0.8
0.3
-0.2
300
400
500
600
700
800
Wavelength (nm)
Hour 0
Hour 22
Hour 45
Hour 69
Hour 92
Hour 164
Hour 189

B.1.2 Decomposition in various solvents of the 0 charge state in air

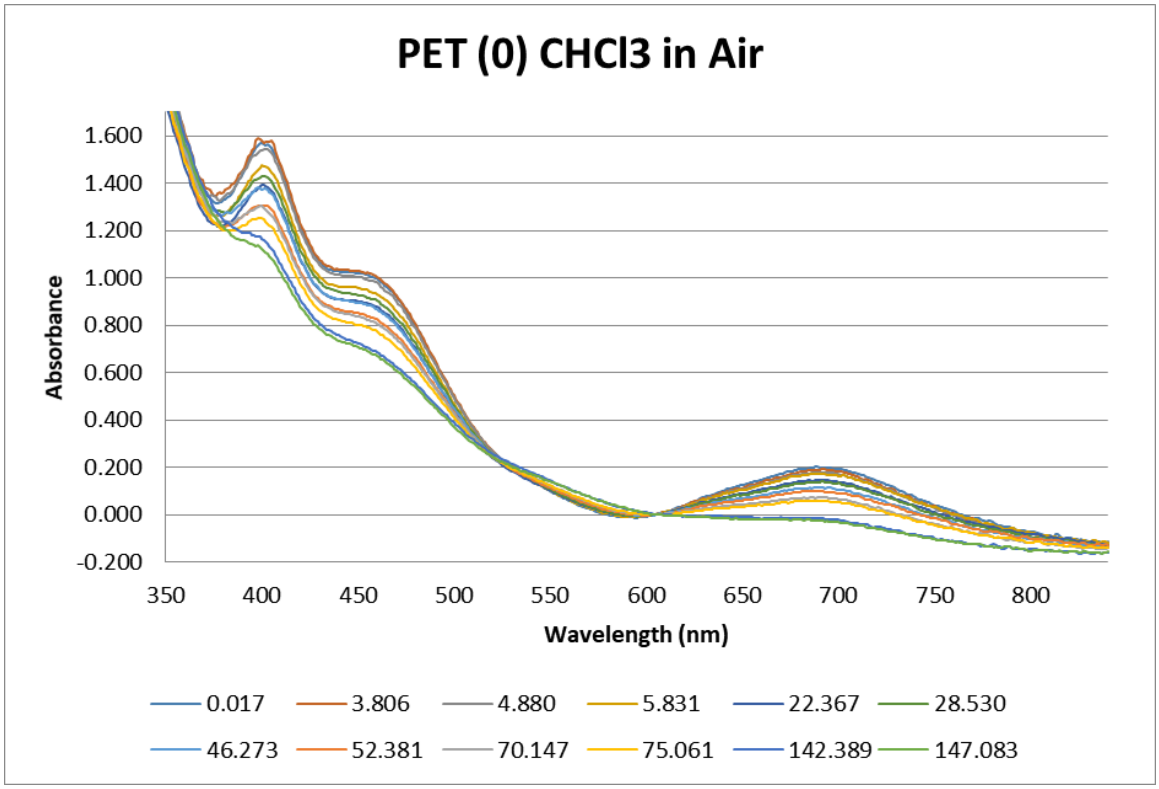

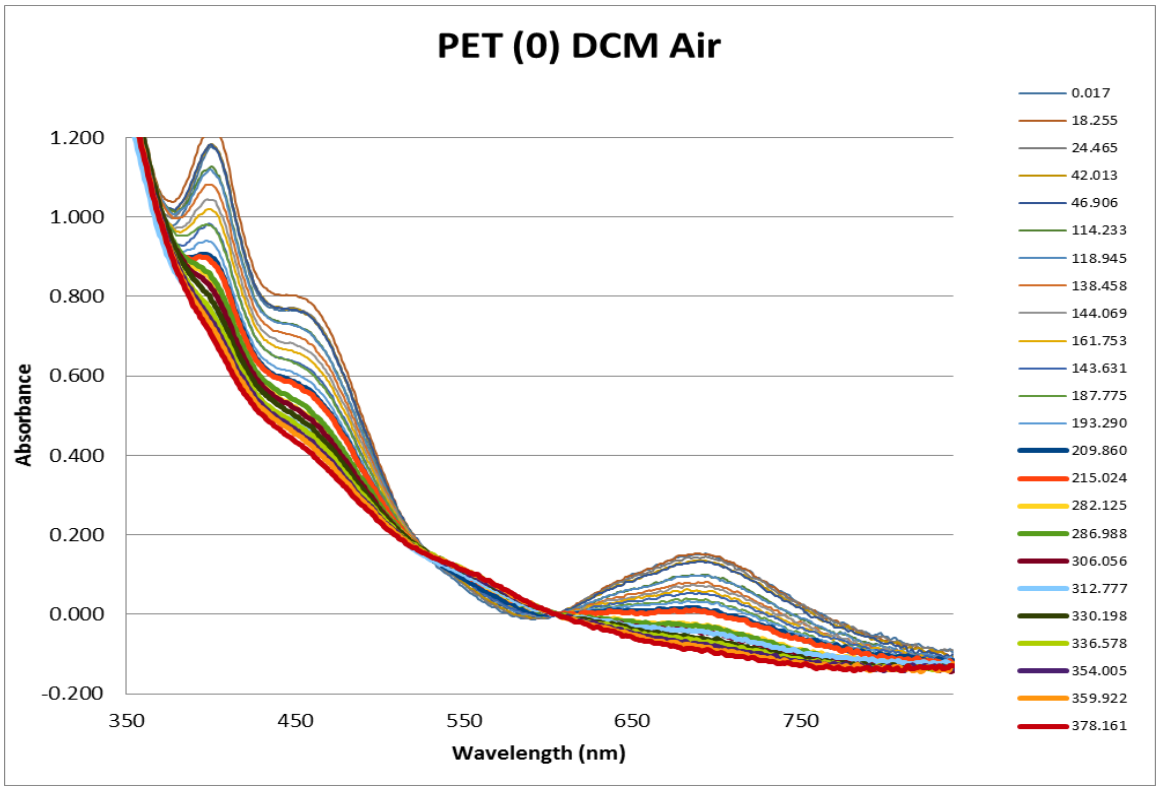

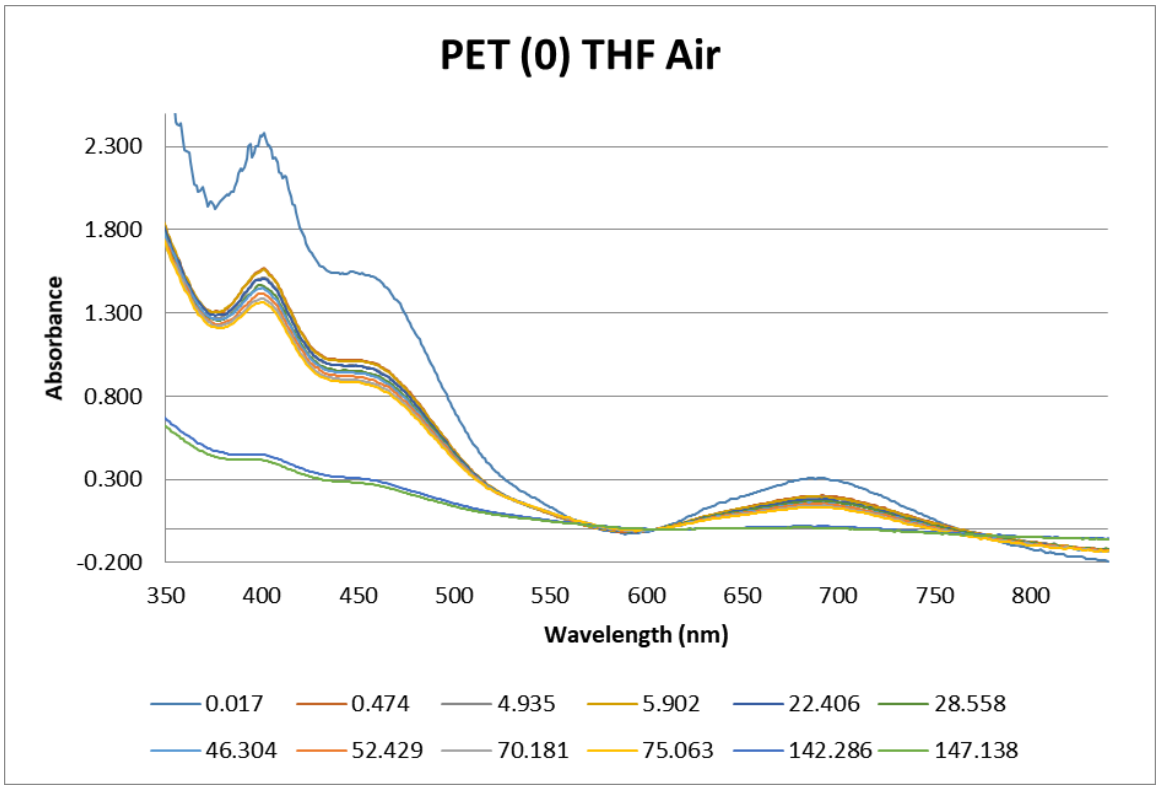
PET (0) THF Air
Absorbance
2.300
1.800
1.300
0.800
0.300
-0.200
350
400
450
500
550
600
650
700
750
800
Wavelength (nm)
0.017
0.474
4.935
5.902
22.406
28.558
46.304
52.429
70.181
75.063
142.286
147.138

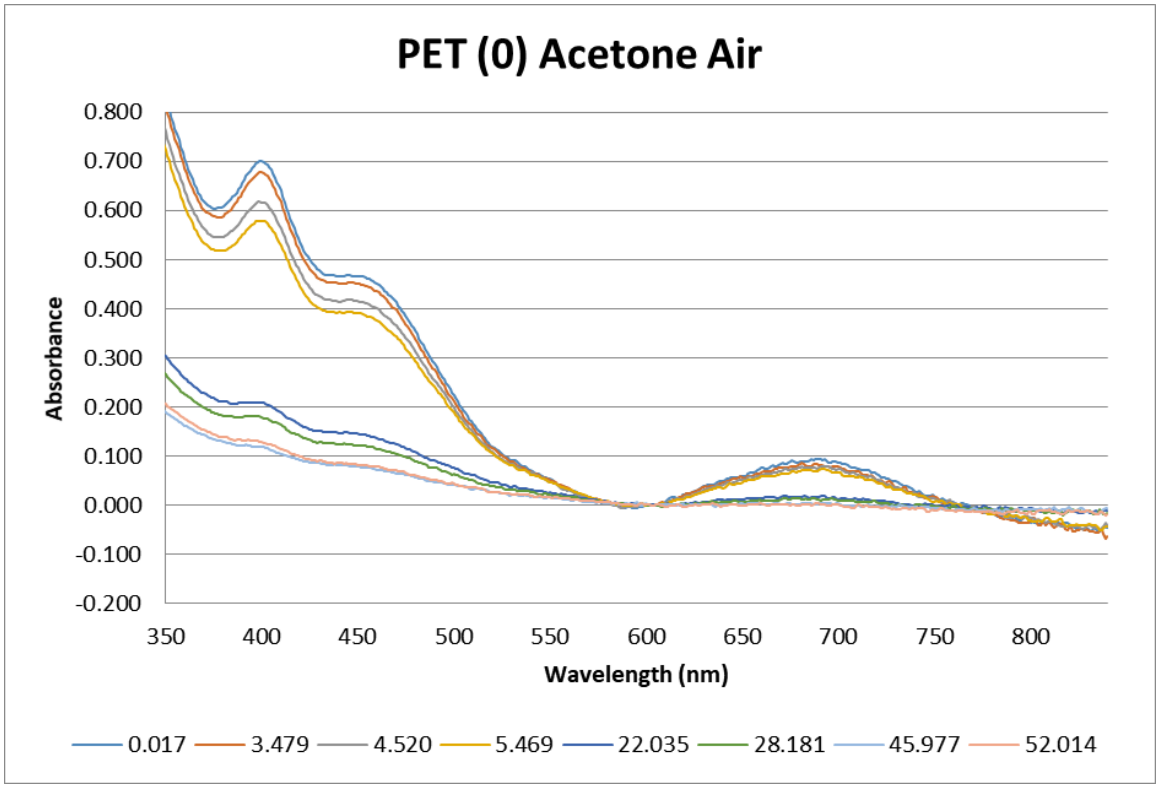
PET (0) Acetone Air
Absorbance
0.800
0.700
0.600
0.500
0.400
0.300
0.200
0.100
0.000
-0.100
-0.200
350
400
450
500
550
600
650
700
750
800
Wavelength (nm)
0.017
3.479
4.520
5.469
22.035
28.181
45.977
52.014

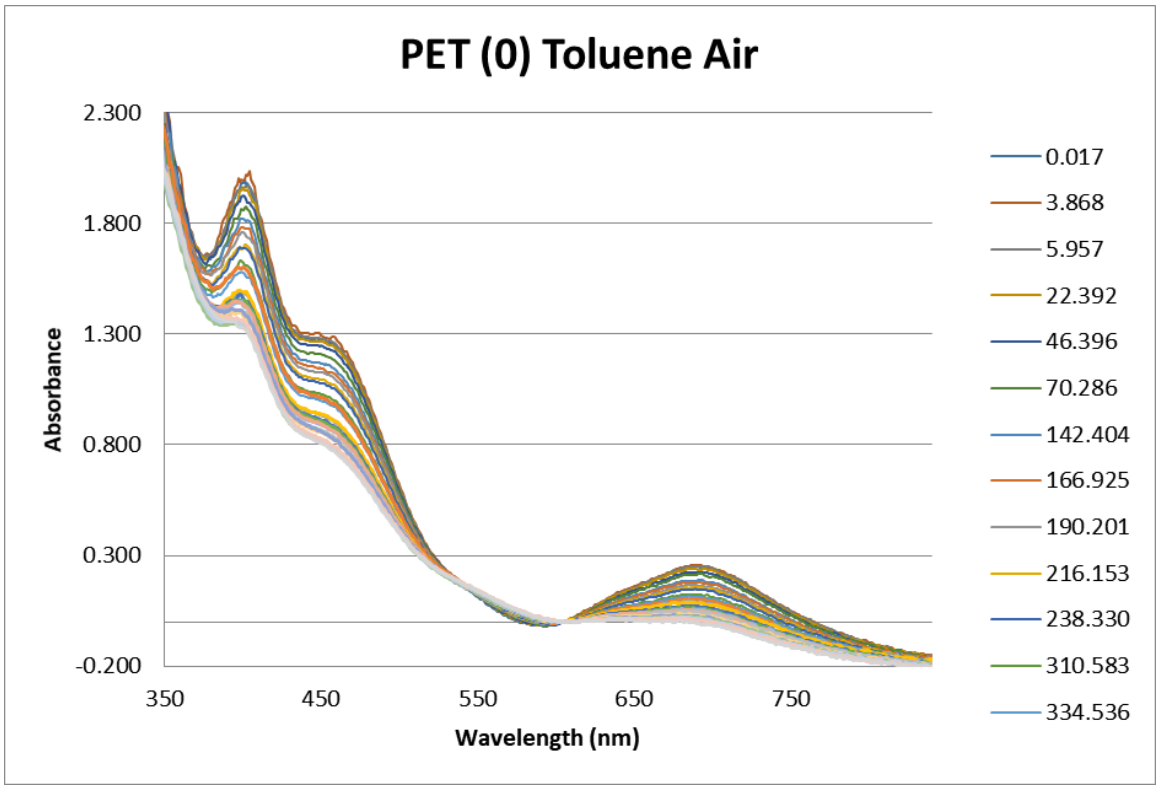
PET (0) Toluene Air
2.300
1.800
1.300
0.800
0.300
-0.200
Absorbance
350
450
550
650
750
Wavelength (nm)
0.017
3.868
5.957
22.392
46.396
70.286
142.404
166.925
190.201
216.153
238.330
310.583
334.536

B.1.3 DECOMPOSITION OF 0 CHARGE STATE WITH DIFFERENT LIGAND IN DCM

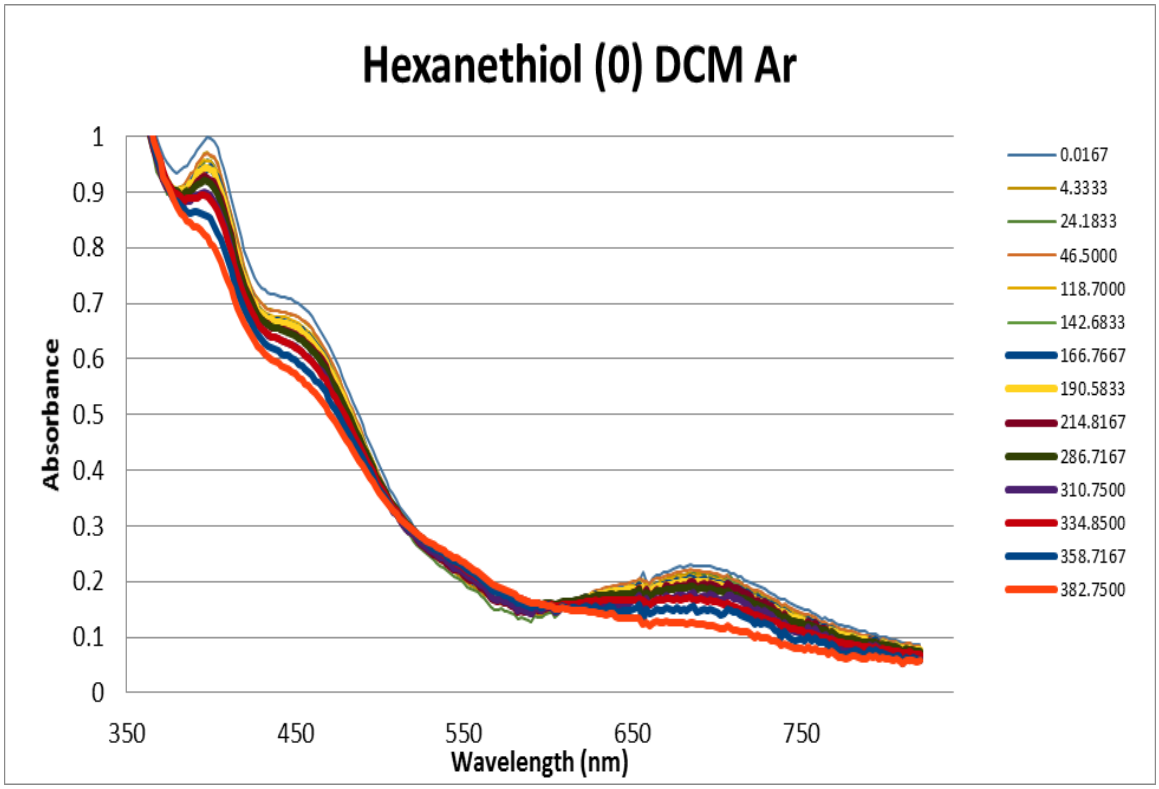

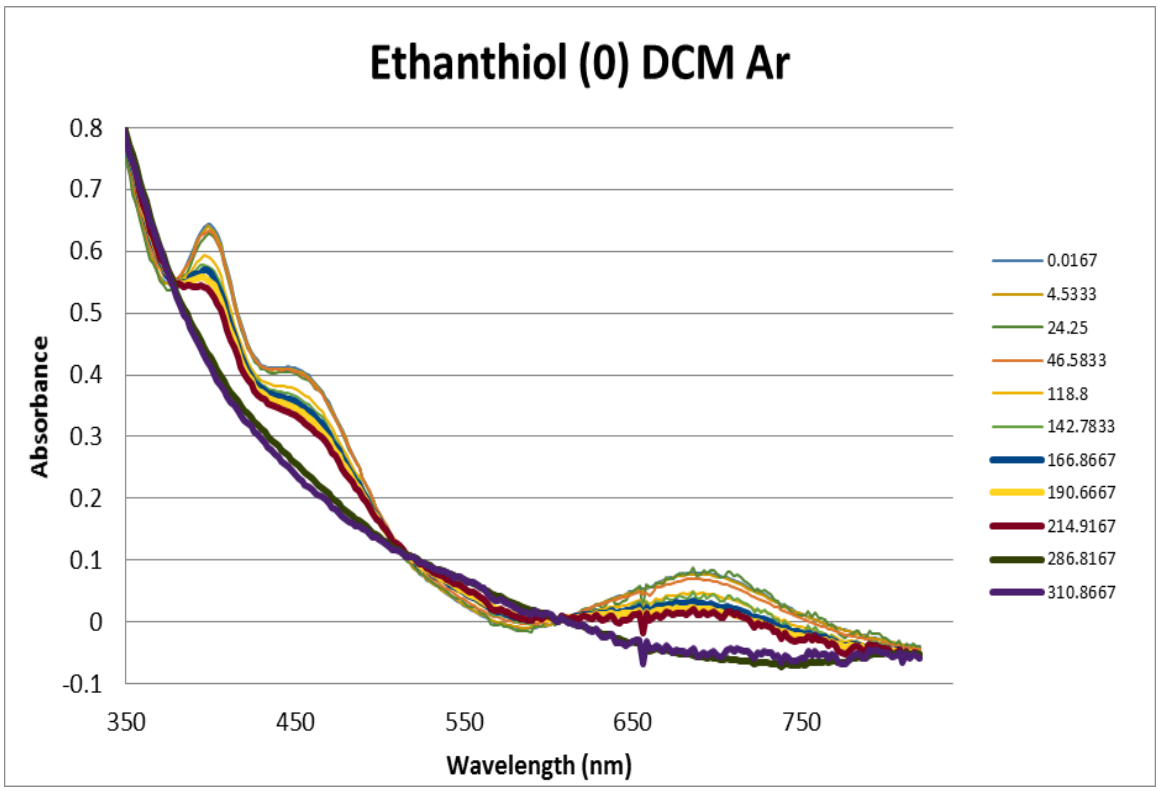

UNDER ARGON

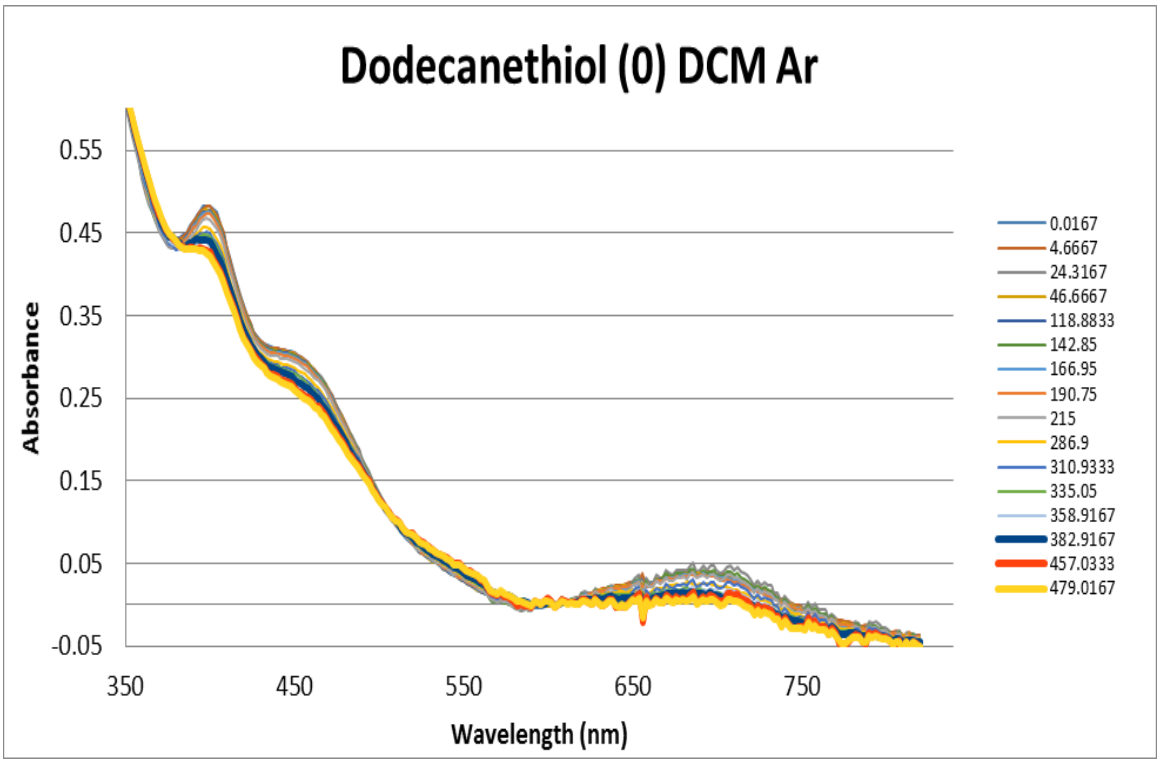
Dodecanethiol (0) DCM Ar
Absorbance
0.55
0.45
0.35
0.25
0.15
0.05
-0.05
350
450
550
650
750
Wavelength (nm)
0.0167
4.6667
24.3167
46.6667
118.8833
142.85
166.95
190.75
215
286.9
310.9333
335.05
358.9167
382.9167
457.0333
479.0167

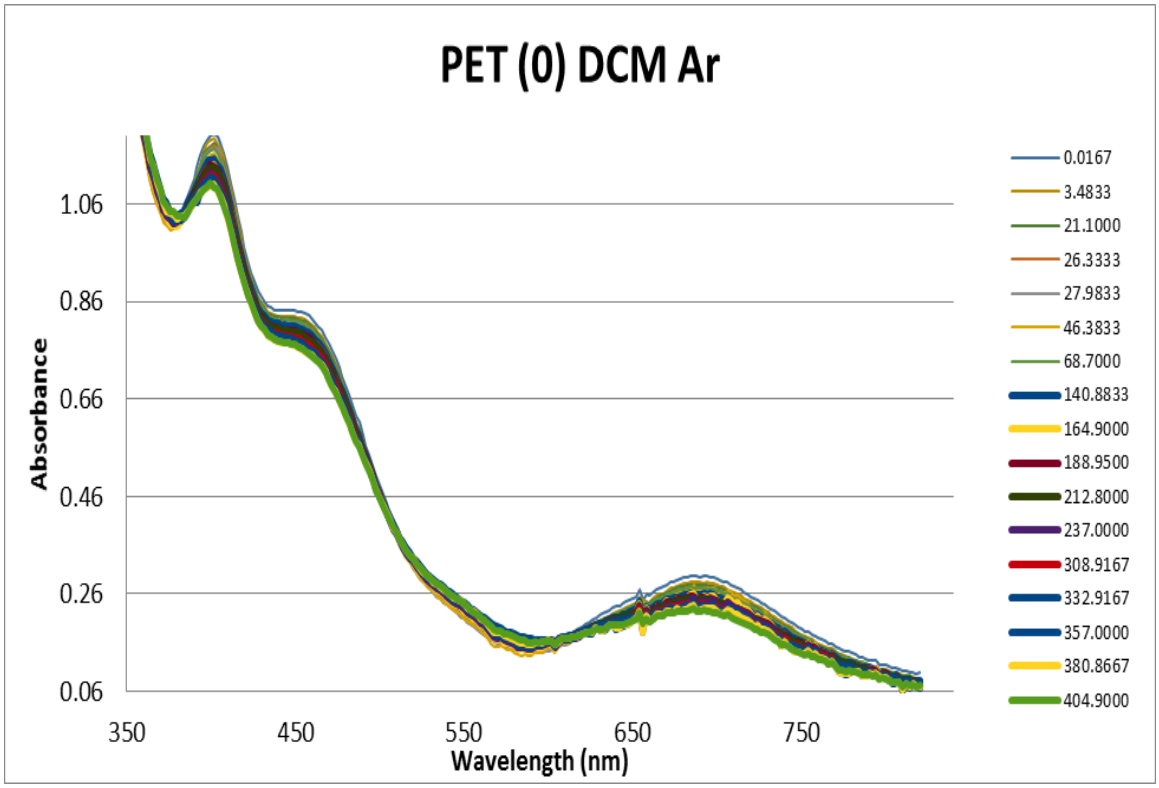
PET (0) DCM Ar
Absorbance
1.06
0.86
0.66
0.46
0.26
0.06
350
450
550
650
750
Wavelength (nm)
0.0167
3.4833
21.1000
26.3333
27.9833
46.3833
68.7000
140.8833
164.9000
188.9500
212.8000
237.0000
308.9167
332.9167
357.0000
380.8667
404.9000

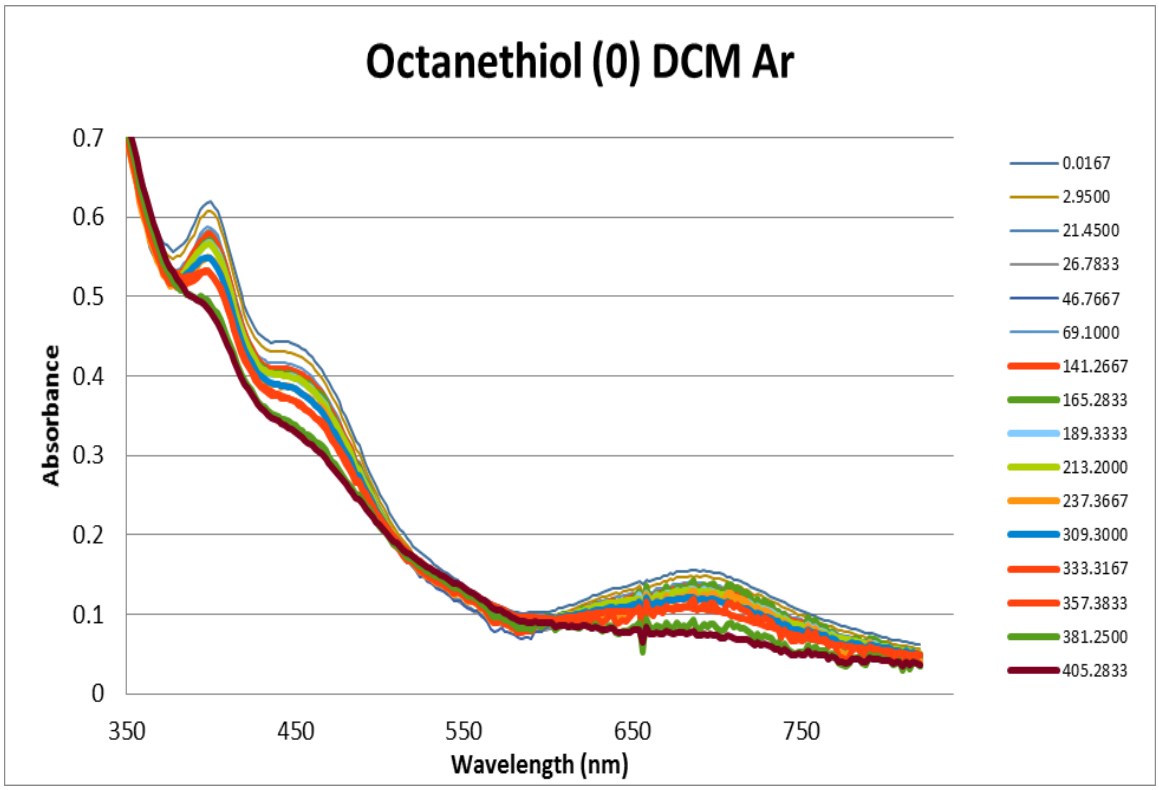

B.2 Linear fits of rate laws to the absorbance data

Concentration was calculated using the molar absorptivity of 8800 $cm^{-1}M^{-1}$ at 680nm. This concentration data was then fit to integrated rate laws using Microsoft Excel and the best fits were chosen to report the reactant order of gold for that set of conditions. The graphs are labeled with the ligand layer charge state solvent then atmosphere.

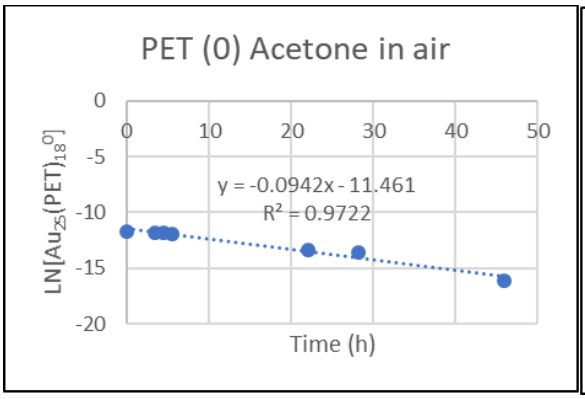

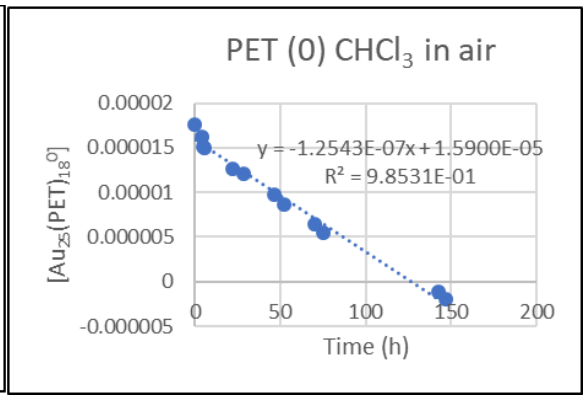

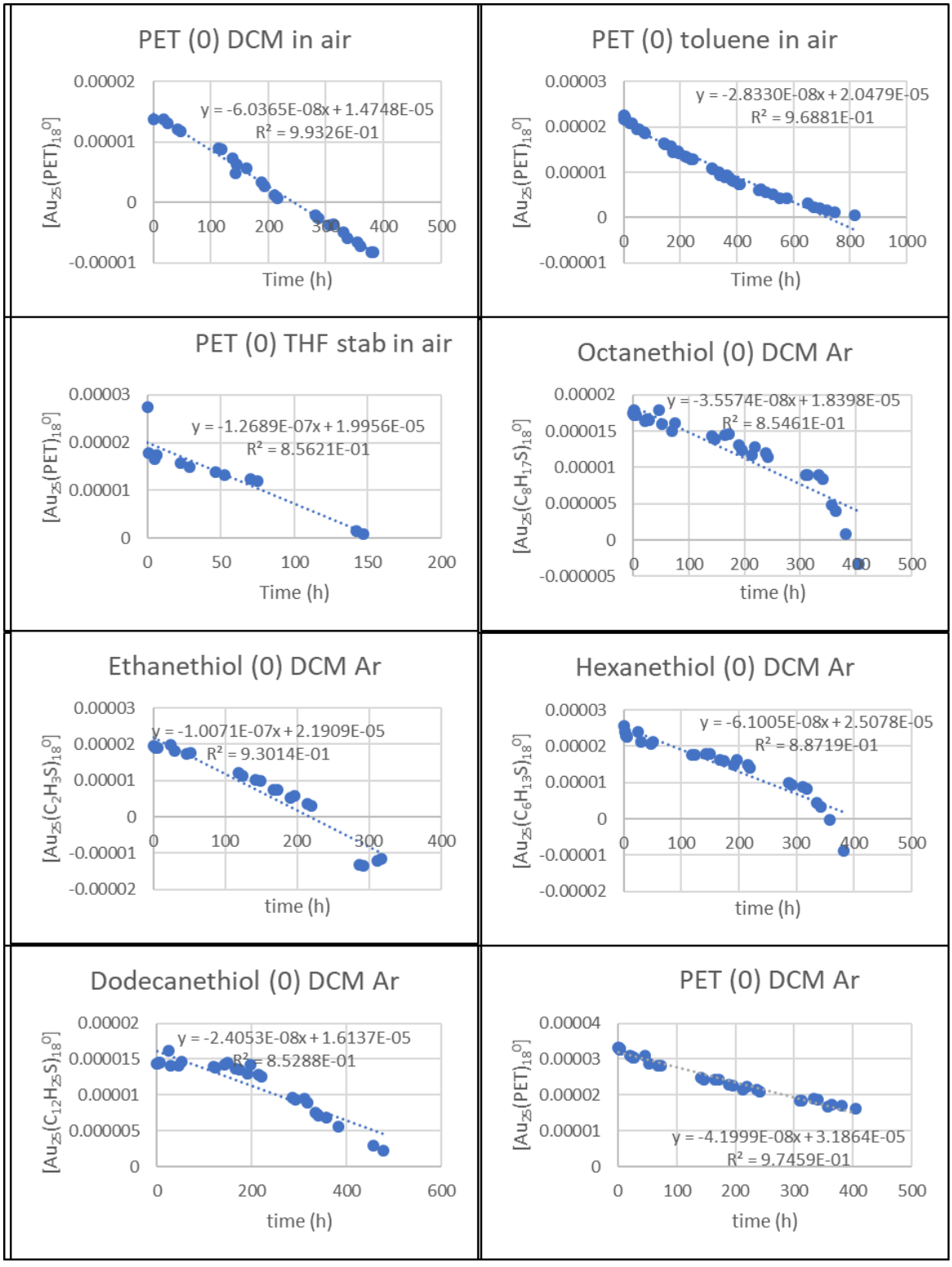
PET (0) DCM in air
y = -6.0365E-08x + 1.4748E-05
R² = 9.9326E-01
[Au25(PET)18 0]
Time (h)
PET (0) toluene in air
y = -2.8330E-08x + 2.0479E-05
R² = 9.6881E-01
[Au25(PET)18 0]
Time (h)
PET (0) THF stab in air
y = -1.2689E-07x + 1.9956E-05
R² = 8.5621E-01
[Au25(PET)18 0]
Time (h)
Octanethiol (0) DCM Ar
y = -3.5574E-08x + 1.8398E-05
R² = 8.5461E-01
[Au25(C8H17S)18 0]
time (h)
Ethanethiol (0) DCM Ar
y = -1.0071E-07x + 2.1909E-05
R² = 9.3014E-01
[Au25(C2H5S)18 0]
time (h)
Hexanethiol (0) DCM Ar
y = -6.1005E-08x + 2.5078E-05
R² = 8.8719E-01
[Au25(C6H13S)18 0]
time (h)
Dodecanethiol (0) DCM Ar
y = -2.4053E-08x + 1.6137E-05
R² = 8.5288E-01
[Au25(C12H25S)18 0]
time (h)
PET (0) DCM Ar
y = -4.1999E-08x + 3.1864E-05
R² = 9.7459E-01
[Au25(PET)18 0]
time (h)

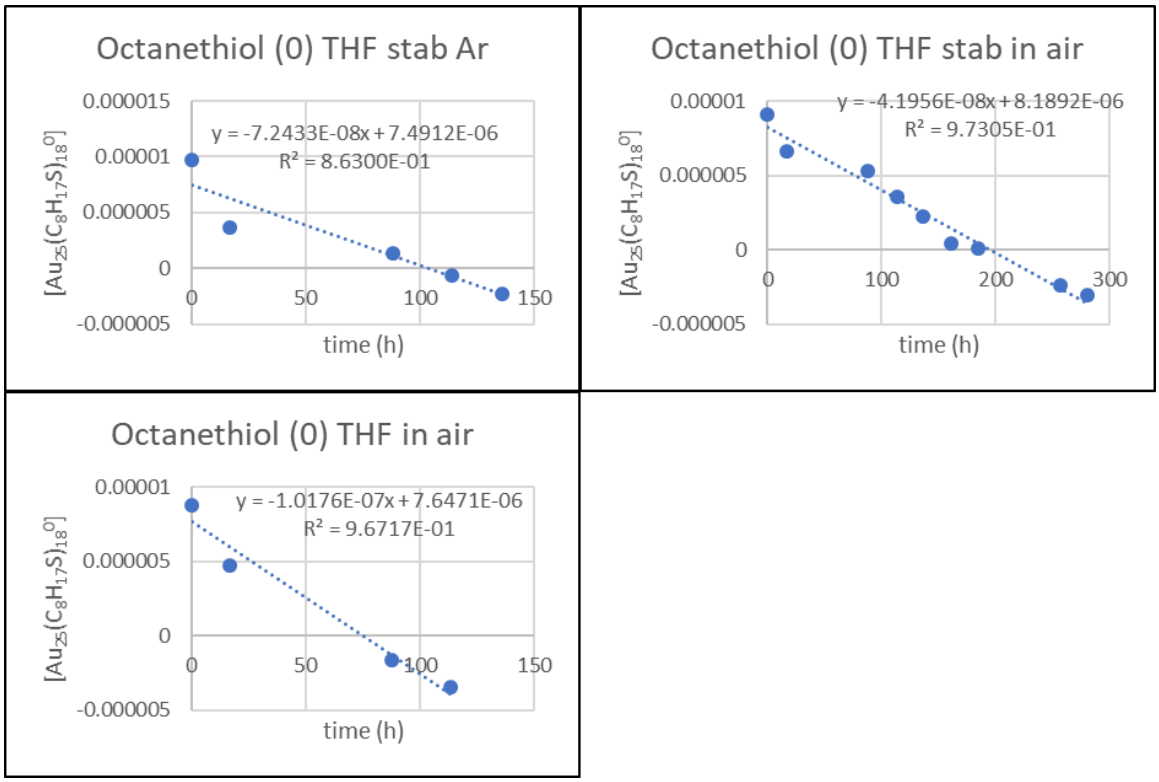

B.3 CONDITIONS RESULTING IN LITTLE TO NO DECAY OVER ~20 DAYS

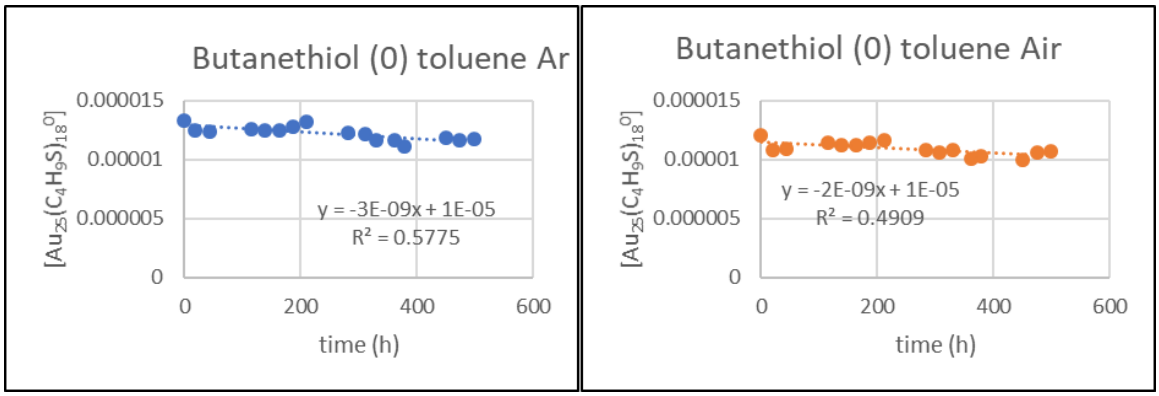

OBSERVED

B.4 Summary of reactant order determination

Ligand	Atm	Charge	solvent	order for cluster	rate constant k	[A]0 (M)	Half life (h)
PET	air	0	Acetone	1st	0.0942	8E-06	7.36
PET	air	0	CHCl3	0th	1.254E-07	1.8E-05	69.9
PET	air	0	DCM	0th	6.04E-08	1.4E-05	114.5
PET	air	0	THF	0th	1.27E-07	2.7E-05	107.8
PET	air	0	Toluene	0th	2.83E-08	2.2E-05	384.4
Ethanethiol	Ar	0	DCM	0th	1.0071E-07	2E-05	97.4
hexanethiol	Ar	0	DCM	0th	6.1005E-08	2.6E-05	210.3
octanethiol	Ar	0	DCM	0th	3.5574E-08	1.8E-05	246.5
dodecanethiol	Ar	0	DCM	0th	2.4053E-08	1.4E-05	297.6
PET	Ar	0	DCM	0th	4.20E-08	3.33E-05	396.7
hexanethiol	Ar	-1	DCM	0th	1.1223E-07	2.5E-05	110.6
PET	Ar	-1	DCM	0th	3.42E-08	3.5E-05	511.8
PET	air	-1	Acetone	1st	0.0147	1.6E-05	47.2
PET	air	-1	CHCl3	0th	9.96E-08	1.6E-05	81.5
PET	air	-1	DCM	0th	1.48E-07	1.9E-05	63.2
PET	air	-1	MeCN	1st	0.0591	1.7E-05	11.7
PET	air	-1	THF stab	0th	2.14E-08	1.6E-05	365.6
PET	air	-1	Toluene	0th	7.48E-08	1.3E-05	86.6

B.5 Differential Scanning calorimetry data

All differential calorimetry scanning measurements (DSC) were taken using TA Instrument's 2920 modulated DSC. All products were re-dissolved in a minimal amount of DCM and then deposited into an aluminum hermetic DSC pan and allowed to air dry in order to achieve uniform coverage of the pan. Once the products were dry enough to stick to the DSC pan they were put under vacuum for 10 min to ensure the complete removal of the solvent.

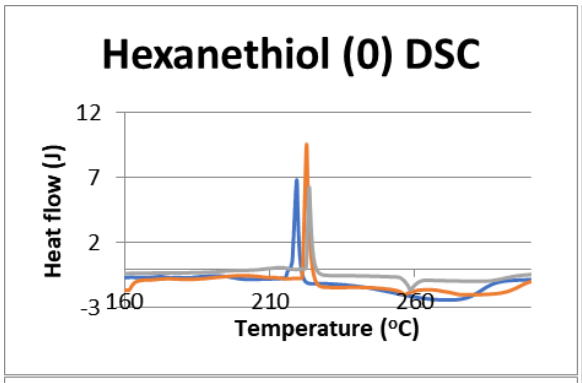
Hexanethiol (0) DSC
Heat flow (J)
12
7
2
-3
160
210
260
Temperature (°C)

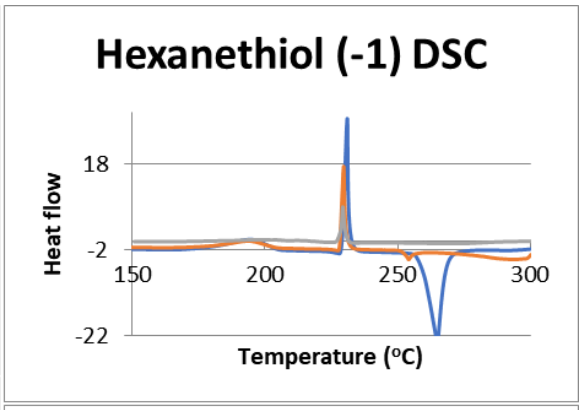
Hexanethiol (-1) DSC
Heat flow
18
-2
-22
150
200
250
300
Temperature (°C)

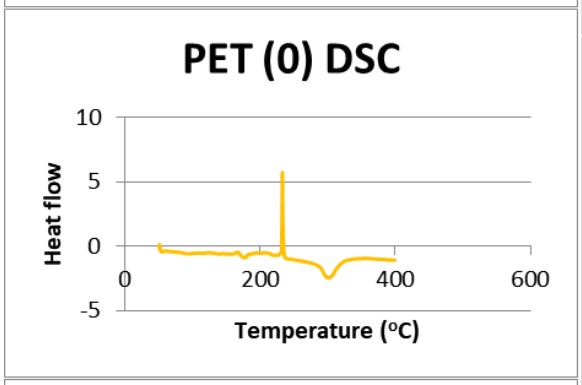
PET (0) DSC
Heat flow
10
5
0
-5
0
200
400
600
Temperature (°C)

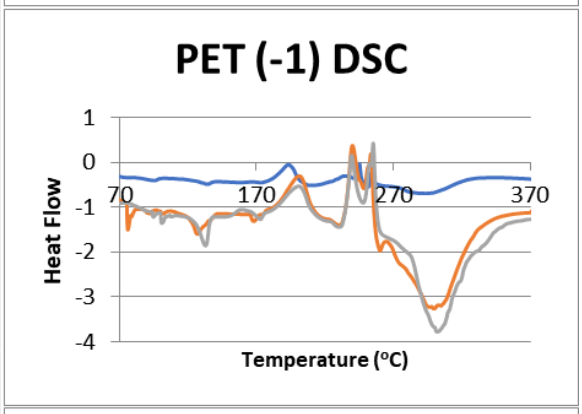
PET (-1) DSC
Heat Flow
1
0
-1
-2
-3
-4
70
170
270
370
Temperature (°C)

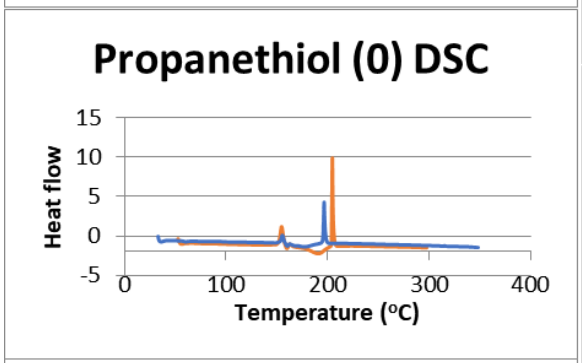
Propanethiol (0) DSC
Heat flow
15
10
5
0
-5
0
100
200
300
400
Temperature (°C)

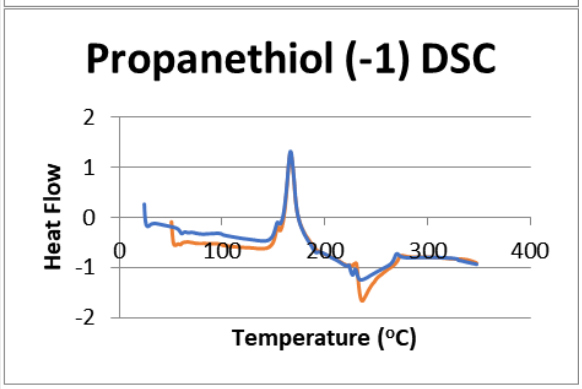
Propanethiol (-1) DSC
Heat Flow
2
1
0
-1
-2
0
100
200
300
400
Temperature (°C)

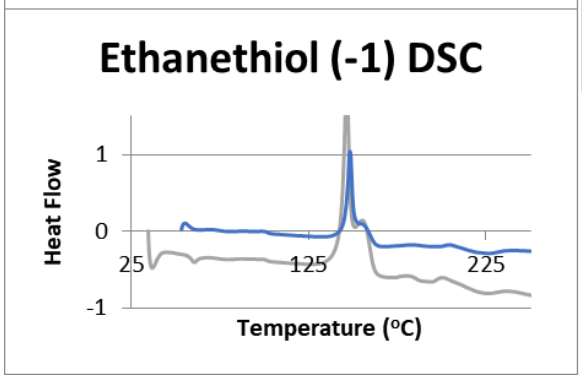
Ethanethiol (-1) DSC
Heat Flow
1
0
-1
25
125
225
Temperature (°C)

APPENDIX C: SUPPLEMENTAL TO CHAPTER 5

C.1 Synthesis of particles:

C.1.1 Magnetite Fe_3O_4 Core synthesis procedure

Magnetite cores were synthesized by thermal decomposition in diphenyl ether following a published method.[1] Briefly, in a 100 mL 3 neck round bottom flask; 10 mmol 1,2 hexadecane diol and 2 mmol iron (III) acytlacetonate was mixed in 20 mL of diphenyl ether. The solution was then purged and flushed with argon. Then 6 mmol oleylamine (90%) and 6 mmol oleic acid was added via syringe. The solution was then heated to 200^{o}C for 30 minutes to boil off impurities. Then it was heated to 265^{o}C and refluxed for 1 hour then cooled to 30^{o}C, and transferred into storage containers.

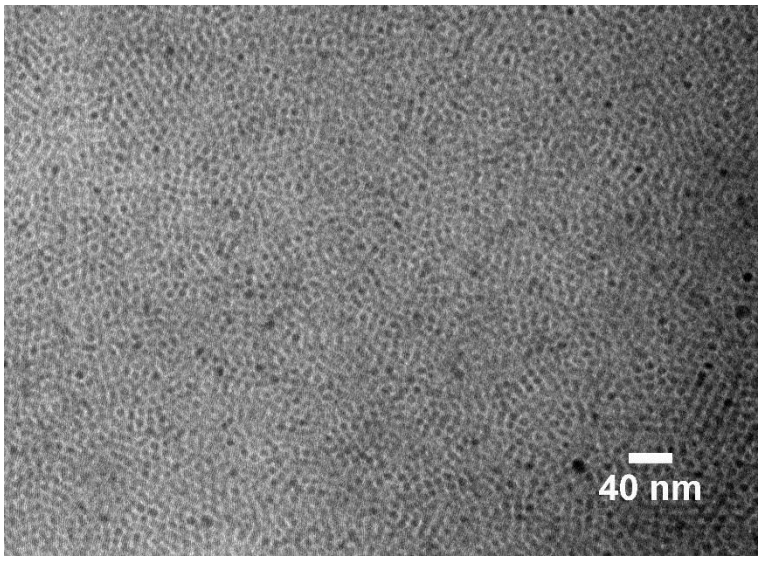

Figure C.S1. TEM of iron oxide cores, particle size measure by hand in imageJ. Average particle size is 4.5 nm diameter with standard deviation of 0.3 nm. TEM images were taken on a JEOL JEM-1400 Transmission Electron Microscope with an accelerating voltage of 100 kV.

C.1.2 Gold Coating Procedure

The magnetite cores were coated using another published procedure.[2] Briefly, 5 mL of the magnetite cores solution from above, without any rinsing or work up was added to a 100 mL, 2 neck, round bottom flask. To that solution, 1.1 mmol gold (III) acetate, 6 mmol of 1,2-hexadecanediol, 0.75 mmol oleic acid and 3 mmol oleylamine was added in 15 mL diphenyl ether. This solution was stirred vigorously at 35^{o}C while purging with argon for 20 minutes. Under argon and vigorous stirring the solution was then it was heated to 185^{o}C and held at that temperature 1.5 hours. To avoid the freezing of the solvent the solution was then cooled down to 35^{o}C and transferred to scintillation vials. The particles were cleaned up by rinsing 3x with 1:1 mixture of hexanes and ethanol. To facilitate faster precipitation a neodymium magnet was placed at the bottom of the scintillation vial. In some cases, it was possible to rinse the particles too much, which could be remedied by adding a small amount of oleylamine back into the solution.

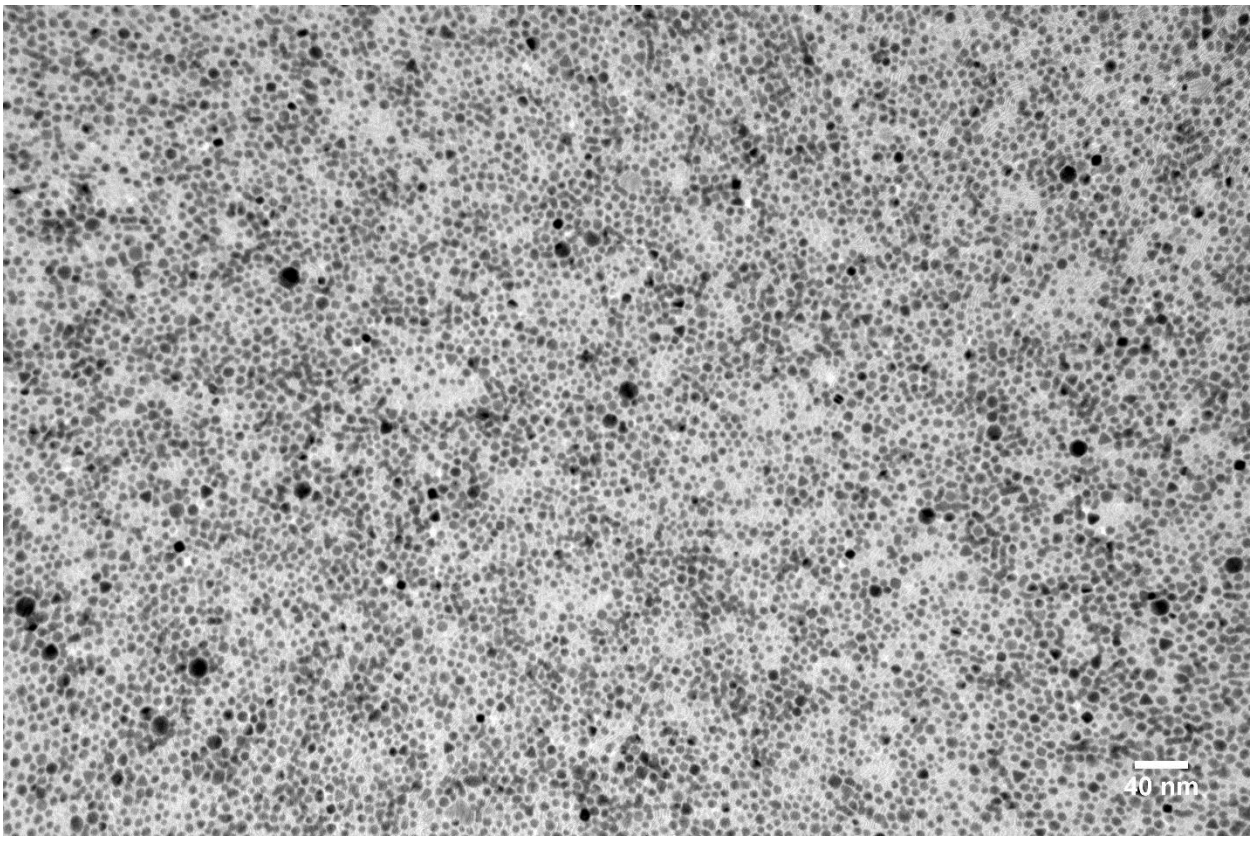

Figure C.S2. TEM of gold coated particles, average particle size is 6.1 nm diameter, standard deviation 2.3nm, particle count 4152. Particle size analyzed with imageJ.

C.1.3 Phase Transfer

To phase transfer the particles a novel two step procedure was used; first an initial exchange and phase transfer from oleylamine coating to 3-mercaptopropanoic acid (3-MPA). Then an exchange of 3-MPA for 11-mercaptoundecanoic acid (11-MUA) to increase solubility in water and biological relevant buffers. In a 20 mL scintillation vial, 2 mL of 17 mg/mL particle solution in heptanes was added with 10 mL of heptanes 5mL of 3-MPA. This is then vortexed overnight. Some phase transfer occurs into the thiol layer almost immediately, but complete exchange was achieved hours later. The particles were then precipitated and washed with 5 mL acetone 3x, until no 3-MPA smell could be detected. The particle pellet was then suspended in 1.5 mL 75 mM

tetramethylammonium hydroxide (TMAOH) solution to give a red solution. The alkalinity and the large counter ion (allowing for larger interparticle separation distance) of the TMAOH solution allowed for incredibly stable suspension of the particles.[3]

To improve the stability of the particles in a wide range of solutions the 3-MPA ligands were further exchanged for longer 11-MUA ligands. To the 1.5 mL batch of phase transferred particles, 3.4 mg of 11-MUA was added and the mixture was sonicated for 20 minutes to facilitate dissolution of the 11-MUA. The mixture was then vortexed for 4 hours at room temp. The particles were then centrifugally precipitated using acetone and rinsed 3x with a 1:1 mixture of acetone to 75 mM TMAOH. Then the particles were resuspended in the working buffer for the thermolysin assay, and exhibited a red solution color characteristic of plasmonic gold nanoparticles < 200nm in diameter.

C.2 Conjugation

A novel conjugation procedure was developed to get around the incompatibility of the solubility of the nanoparticles and thermolysin, which is soluble in high ionic strength solutions. To desalt the thermolysin, which is shipped by sigma Aldrich 20% salt by mass because cations are responsible for the remarkable thermal stability of thermolysin, 15 mg was suspended into 3 mL pH 7.5, 50 mM phosphate buffer. This solution was rinsed placed on a rocker for 20 minutes, following by centrifugal precipitation of the enzyme at 4^{o}C, 4000 rpm for 20 minutes. Then 10 mg of lyophilized and thoroughly rinsed Fe_3O_4@Au NP were dissolved in 3 mL fresh 50 mM pH 6.8 phosphate buffer. The particles were sonicated for ~ 10 minutes until they were clearly in solution. Then 10 mg of HATU was added to the nanoparticle solution and sonicated

for 20 minutes. Note the HATU is poorly soluble in water and forms a poor suspension. After sonication, which activates the carboxylic acid groups on the ligands the solution was diluted with 6 mL of pH 6.8, 50 mM phosphate buffer. This was added directly to the washed thermolysin pellet. This was mixed by inversion in hand and then put in a vortexer for 3 hours at 4^{o}C. The conjugates were then precipitated via centrifuge, rinsed 2x and then resuspended in 10 mL of pH 7.5, 50 mM phosphate buffer. No enzymatic activity was detected in the second rinsing, indicating very little if any free thermolysin. Besides testing the activity of the conjugates, a SDS PAGE was used to confirm conjugation.

C.2.1 SDS PAGE of conjugates

A precast BioRad 4-15% gradient gel (product #4561083) was used to confirm a mobility shift in conjugated nanoparticles and thermolysin vs free nanoparticles and thermolysin. Samples were incubated in NewEngland BioLabs purple gel loading dye with SDS (product #B7024S) at 95^{o}C for 5 minutes in order to thoroughly denature the enzyme.

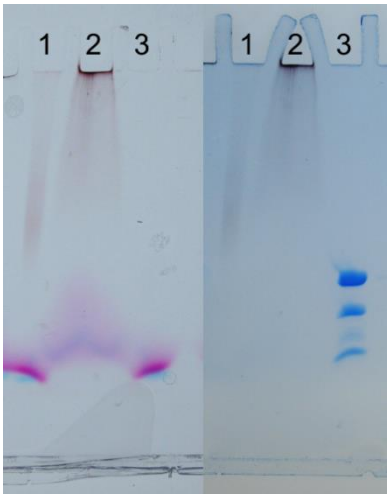

Figure C.S3. SDS page gel (biorad precast gradient gel 4-15%) of 1) free nanoparticles, 2) NP thermolysin conjugates, 3) free thermolysin before (left side) and after (right side) staining with Coomassie brilliant blue protein stain. The large mobility shift of from the free particles in lane 1 to the conjugated particles in lane 2 confirms the

size increase expected with a layer of thermolysin conjugated to it. Note there is also very little to no free thermolysin left over in the conjugates after a thorough rinsing.

C.2.2 Ratio of thermolysin to particles in conjugation

Thermolysin from SigmaAldrich is 70% thermolysin by weight, with the rest of the weight being salt, specifically the Ca^{2+} and Zn^{2+} cations necessary for catalytic activity. I used 15.1 mg for the conjugation so really there is 10.5 mg of thermolysin. The molecular weight of thermolysin is 34.6 kDa, so the 10.5mg is $3.03*10^{-7}$ moles or $1.8*10^{17}$ thermolysin enzymes.

For the particles I used 10mg of 4.5 nm (TEM/core) diameter particles, since the particles are spherical core volume of the particle is So $(2.25*10^{-7}\ cm)^3$ * (4/3) *Pi = $4.8*10^{-20}\ cm^3$. From synthesis paper[2] shell is ~1 nm thick with ratio of Au:Fe weight ratio of 71:29.

For magnetite the unit cell parameter a*b*c=8.39 angst,[4] so unit cell volume is $5.90*10^{-24}\ cm^3$, and there are 8 Fe_3O_4 in each cell so volume per unit cell $73.8*10^{-24}\ cm^3$ with 24 Fe and 32 O weight per unit cell is $307.6*10^{-21}$ g. Weight of iron per unit cell is $2.3*10^{-21}$ g. From my particle size and unit cell size there are 646 unit cells per particle thus $1.41*10^{-16}$ g/particle. And weight of Fe per particle is $646*2.3*10^{-21} = 1.48*10^{-18}$g. So using weight of gold per particle is $(1.07*10^{-18}g)*(71/29)= 3.62*10^{-18}$g Au per particle

Surface coverage of 11-MUA 5.70 nm^{-2} which is 5.7 $*10^{14}\ cm^{-2}$.[5] Surface area of 6.1 nm particle $4*Pi*(3.05\ nm)^2= 78.53\ nm^2$. Thus, there are 5.7*78.53= 448 MUA per particle (218.36 g/mol). The weight of 11-MUA $218.36 *6.02*10^{23}=3.62*10^{-22}$ g per 1 MUA ligand. For each particle there are $3.62*10^{-22} *448= 2.9*10^{-19}$ g MUA so in total $2.9*10^{-19}$ g MUA + $3.62*10^{-18}$ g Au + $1.99*10^{-16}$ g Fe_3O_4 = $2.03*10^{-16}$ g per particle. So,

for 10 mg of particles there are have 0.010g /2.03*10^{-16} = 4.9*10^{13} particles. So the ratio I used in conjugation: 1.8*10^{17} thermolysin / 4.9*10^{13} particles = 3670:1 tln:particle.

C.2.3 Ratio of thermolysin to particles after conjugation and rinsing

Using the molar mass of the particles determined above, a molar absorptivity for the particles was determined using the plasmon absorption peak at 540 nm.

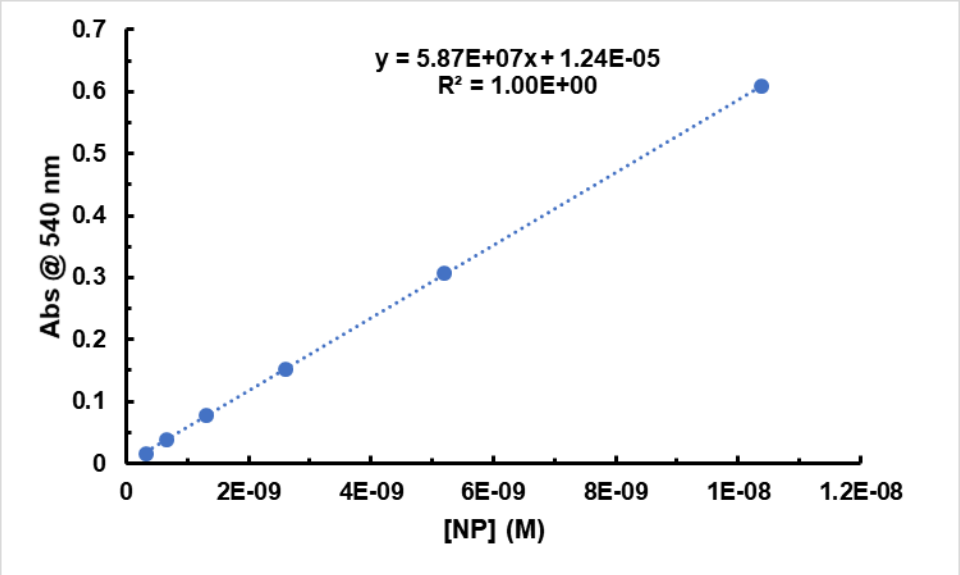

Figure C.S4. Standard cure of particle concentration vs UV-vis absorbance at 540 nm

The absorbance from conjugate sample is 0.139 at 540 nm, using the linear fit this corresponds to a concentration of 1.7*10^{-9} M.

The conjugates were then etched with 0.5 M NaCN, for ~15 minutes until red plasmon peak was no longer visible in uv-Vis. Then a Bradford assay was performed to determine the concentration of thermolysin. First, standard solution of known thermolysin concentrations were made, and then reacted with 0.5 mL Bradford reagent (Sigma Aldrich catalog # B6916) for 5 minutes. At that point the uv-VIS absorption was measured at 595 nm. The cyanide etched conjugate sample was then reacted with 0.5 mL Bradford reagent and using the standard curve the absorbance was converted to a

concentration of 0.048 mg/mL of thermolysin or $7.9*10^{-7}$ M. This gives a ratio of 333 mol of TLN:1 mol of nanoparticles.

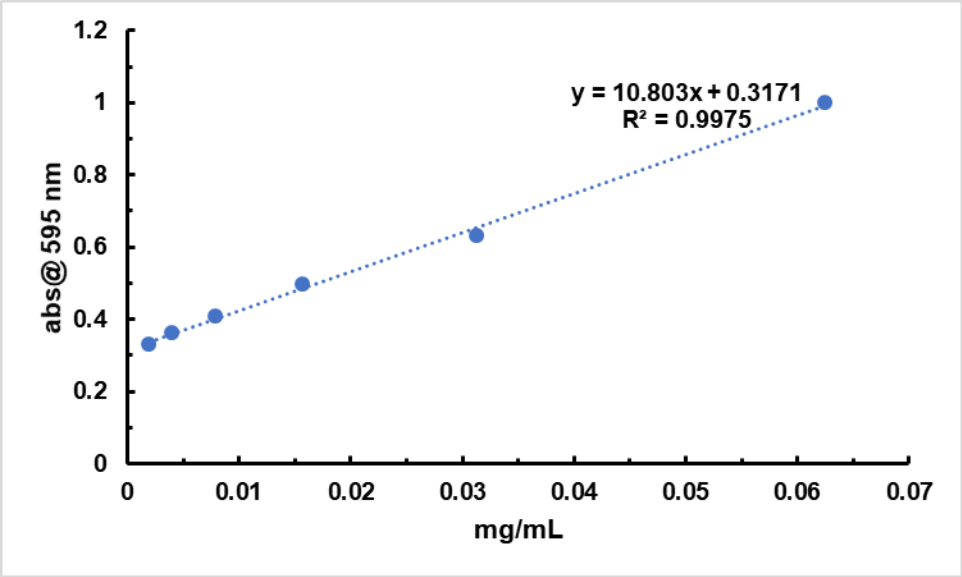

Figure C.S5. Bradford assay standard curve of absorbance at 595 nm vs concentration of thermolysin. This was used to determine concentration of thermolysin in conjugates.

C.3 Enzyme assays:

C.3.1Thermolysin activity assay and bulk heating experiments

The assay was based on the commercially available Pierce™ Colorimetric Protease Assay Kit (catalog # 23263) optimized for the specific enzyme conjugates and substrate. Aliquots (for 0,1,2,3 minute time points) of 50 µL of 4 mg/mL succinylated casein in 50 mM pH 7.5 50 mM phosphate buffer were pre-'heated' at 17.7°C (or different temperature for the temperature studies) in a thermocycler for ~10 minutes along with a buffer blank. Then 5 µL of thermolysin conjugates were added and the samples were heated for 0, 1, 2 and 3 minute time points. To stop the reaction 10 µL of 0.5 M EDTA was added to chelate the catalytic zinc and structural calcium ion, denaturing thermolysin. Then after allowing the reaction to cool back down to room temperature for 5 minutes 25 µL of colorimetric reagent, TNBSA was added. The samples were then incubated at room temperature for 20 minutes, and using the

pedestal on a NanoDrop uv-Vis spectrometer the absorbance was measured at 430 nm to monitor f ormation of the orange product that forms when primary amines react with TNBSA. The slope of the line was then used to calculate the velocity of the enzyme reaction.

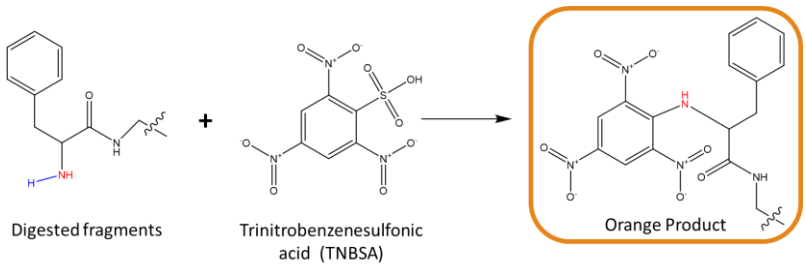

Figure C.S6. Reaction scheme for TNBSA with digested fragments

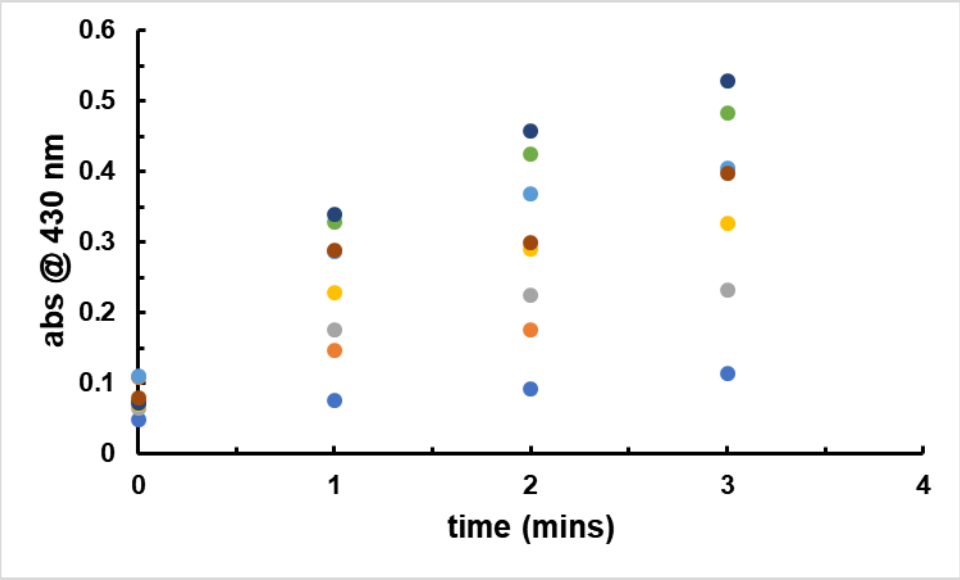

Figure C.S7. Bulk heating in absence of RF field at 17.7°C, average slope of 4 trails (activity) was 0.02 with a standard deviation of 0.0014.

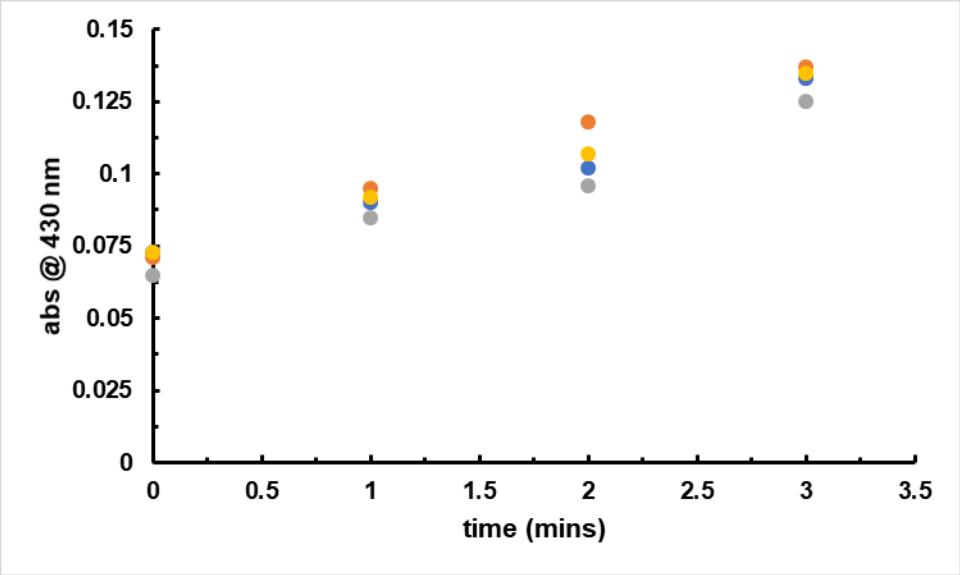

Figure C.S8. Assay results for temperature study. Bulk heating conjugates at 10°C (blue), 20°C (orange), 30°C (grey), 40°C (yellow), 50°C (maroon), 60°C (green), 70°C (dark blue), 80°C (light blue) .

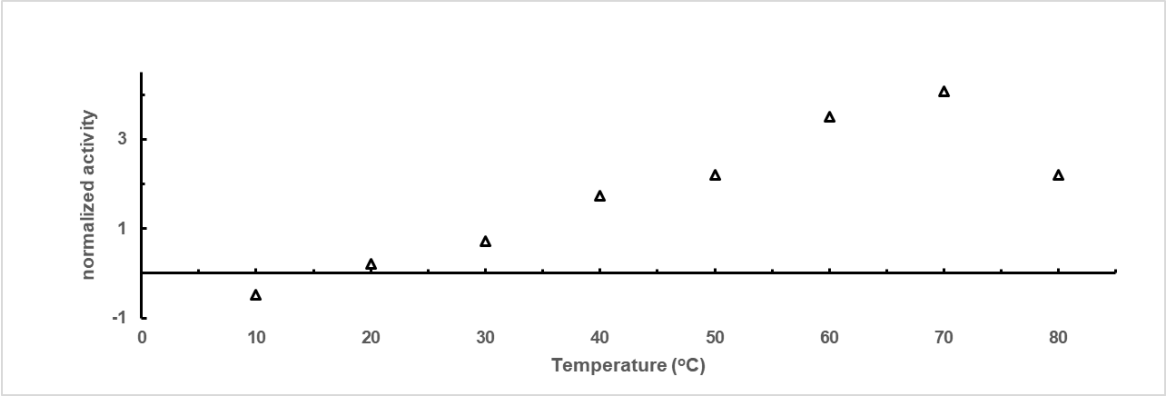

Figure C.S9. Summary of slopes obtained from bulk heating experiments in figure C.8.

C.4 Radiofrequency heating assays

The exact same assay procedure was used for the RF heating experiments so that they were comparable. The fields were generated using a homemade water-cooled solenoid, shown in figure 5. It was powered by a Philips PM5192 function generator to input a 17.76 MHz sinusoidal signal into a IFI scx100 power amplifier. An impedance matching box was used to tune the reflected power to zero, new tunings were required for changes in frequency and applied power. The bulk solution temperature was monitored with a Neoptix Nomad fiber optic temperature probe and then the conjugates were pre- heated in a thermocycler as described above to the same temperature, and the velocities of the two different heating methods were compared.

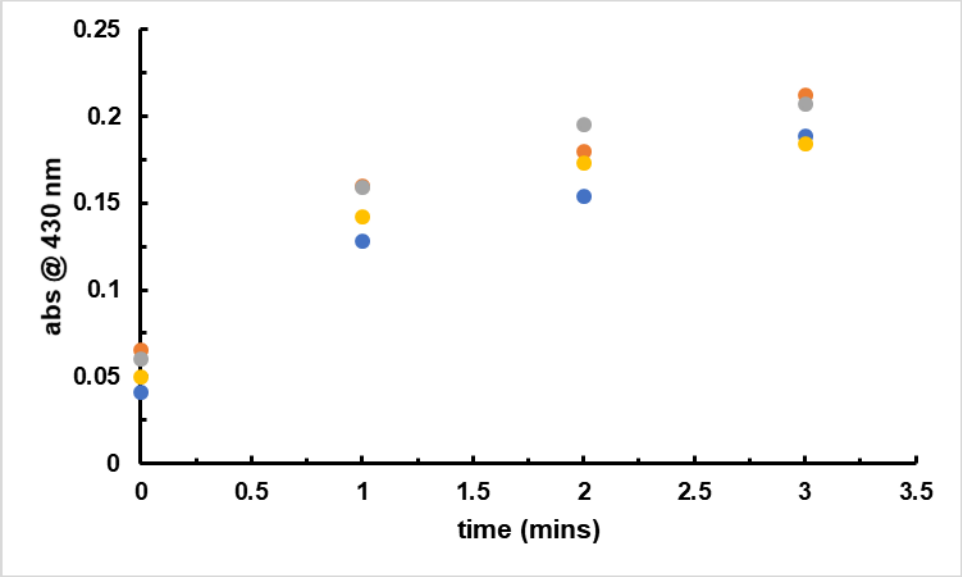

Figure C.S10. RF Heating at 80W, average slope of 4 trials (activity) is 0.046 with a standard deviation of 0.0019

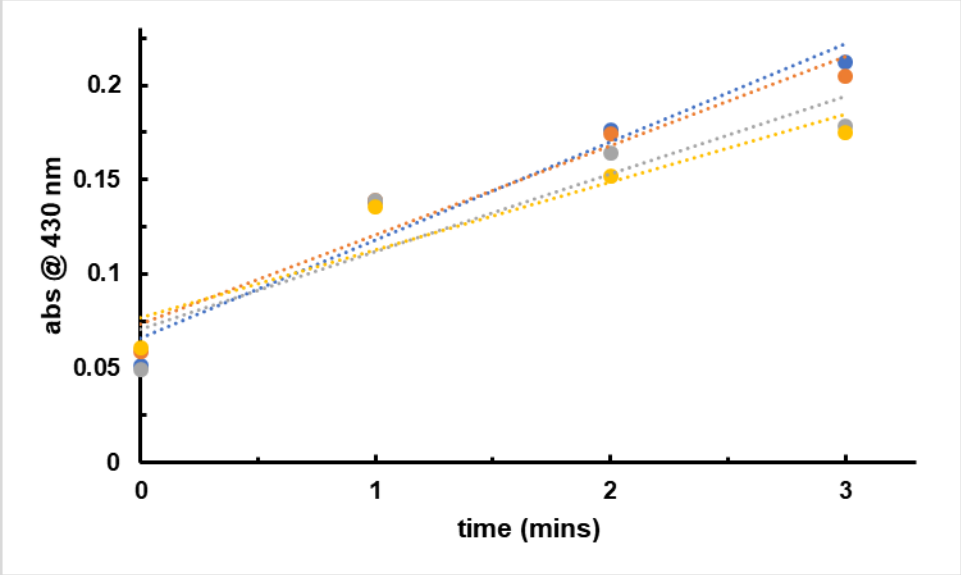

Figure C.S11. Activity assay of RF power study to determine activity as a function of power. Here yellow is 20W with a slope of 0.036, grey is 35W with a slope of 0.041, orange is 65W with a slope of 0.047, blue is 80W with a slope of 0.052.

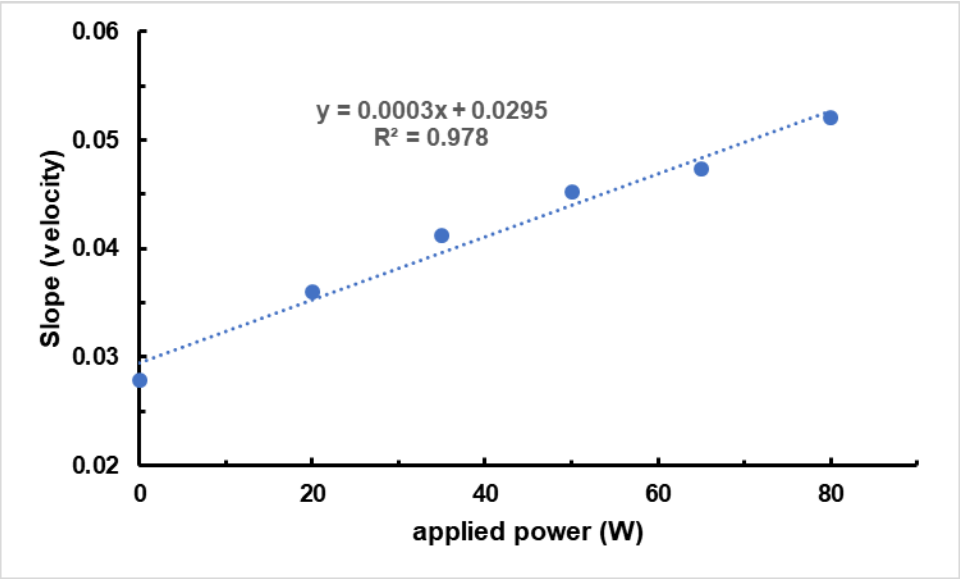

Figure C.S12. Plot of activity in RF vs applied power from the data in figure above. Velocity units are (min^{-1}).

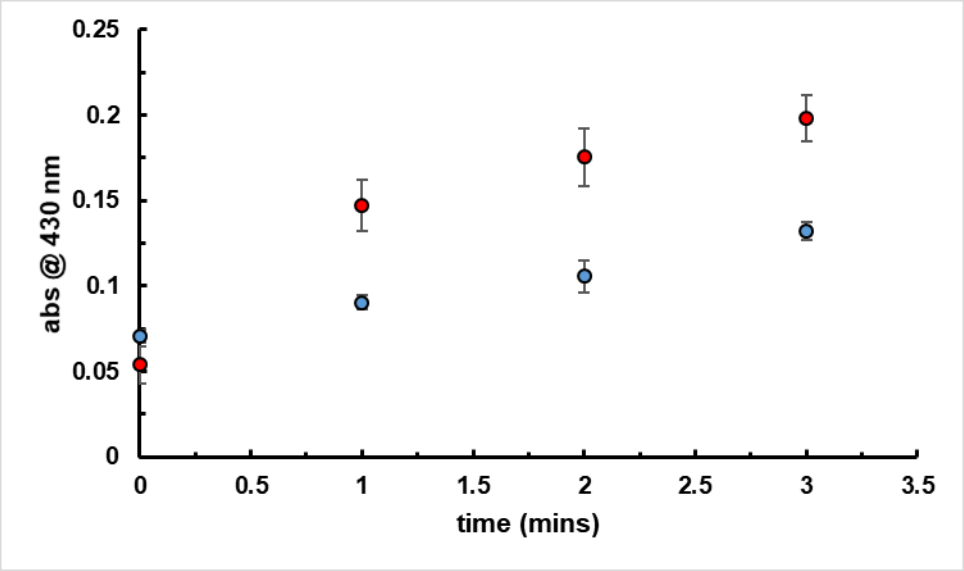

Figure C.S13. Combined bulk at 17.7°C vs RF heating at same temperature but in an 80W RF field. Error bars represent measurements in quadruplicate.

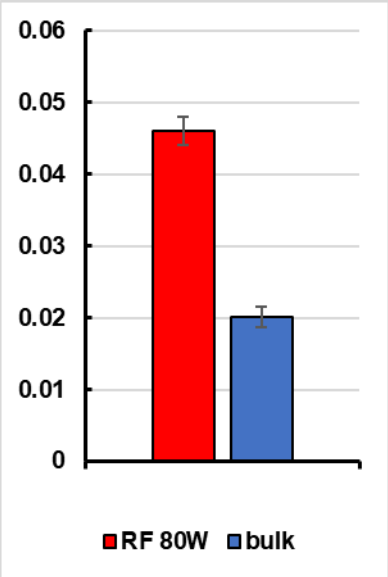

Figure C.S14. Bar graph showing slopes and error bars for RF heating at 80W vs bulk heating at the same temperature in absence of RF field. An increase of activity of 56 ± 8 % is observed for the quadruplicate trials.

C.5 Bulk temperature measurements in RF field

To determine the temperature to compare RF heating trials to bulk heating trials the bulk solution temperature of the reaction mixture had to be measured. This is not something that can be done with a normal thermometer, due to the small volume sizes

(0.5 mL) or a thermocouple, because the thermocouple interacts with the field and heats itself. Instead we must use a fiberoptic temperature probe, in this case it's a Neoptix Nomad fiber optic temperature probe.

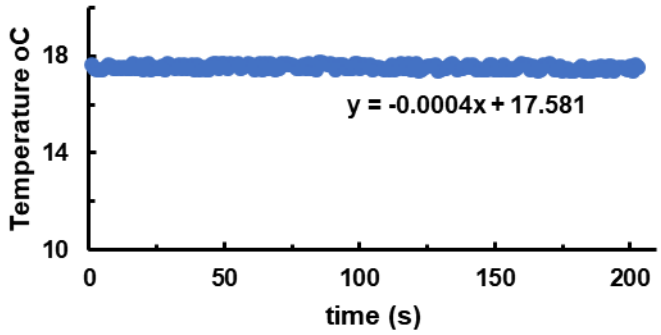

Figure C.S15. Temperature measurement of 80 W RF sample over 3 minutes. The water cooling system kept the samples at essentially the same temperature for all runs. The 80 W heated the coil the most so its temperature was used for the temperature of all the bulk heating experiments (17.7°C).

C.6 Enzyme Kinetics measurements:

The same enzyme assay was used for kinetics experiments, but the substrate concentration was varied so that the Michaelis Menten kinetics model could be used to investigate differences in RF fields vs the absence of RF fields. The assumption for this kinetics model is that the catalysis happens in two distinct steps, substrate binding and catalysis.

$$E + S \underset{k_{-1}}{\overset{k_1}{\rightleftharpoons}} ES \xrightarrow{k_{cat}} E + P$$

Figure C.S16. Simplified reaction scheme for enzyme catalysis used in Michaelis Menten enzyme kinetics model.

$$\frac{1}{v} = \frac{K_M}{V_{max}\ [s]} + \frac{1}{V_{max}}$$

Equation C.S1. Linear fit equation to find kinetic parameters V_{max} (maximum velocity when saturated with substrate) and K_m (Michaelis constatnt). From this information k_{cat} can be calculated.

$$K_m \overset{\text{def}}{=} \frac{k_{cat} + k_{-1}}{k_1}$$

Equation C.S2. Equation for definition of K_m.

$$V_{max} \overset{\text{def}}{=} k_{cat}\,[E]_{tot}$$

Equation C.S3. Equation to find k_{cat} from V_{max}.

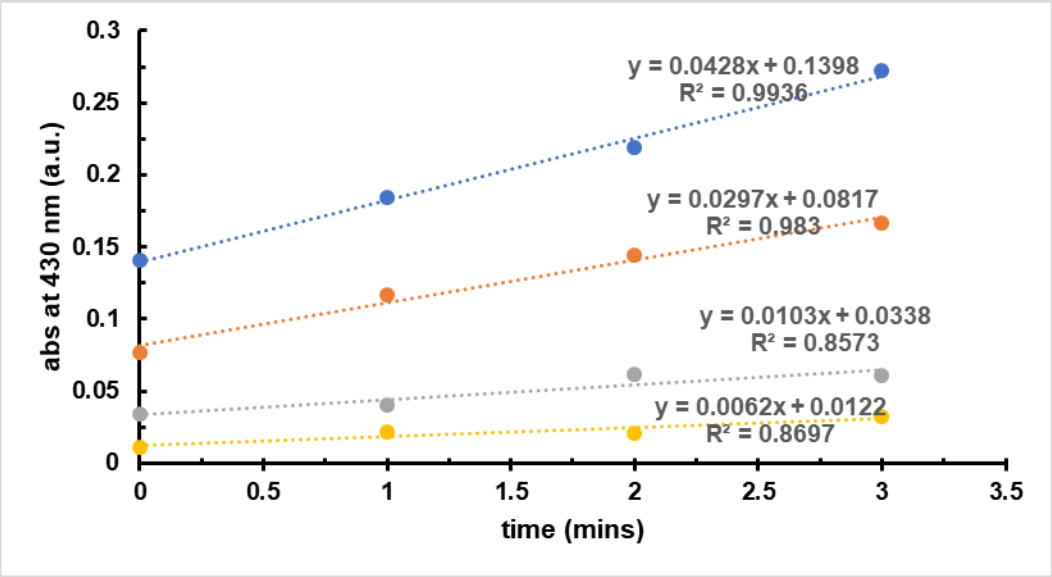

Figure C.S17. Bulk 'heating' at 17*C absorbance measurements of for activity of thermolysin at substrate concentrations of 0.2 (yellow), 0.5 (grey), 2 (orange) and 4 mg/mL (blue).

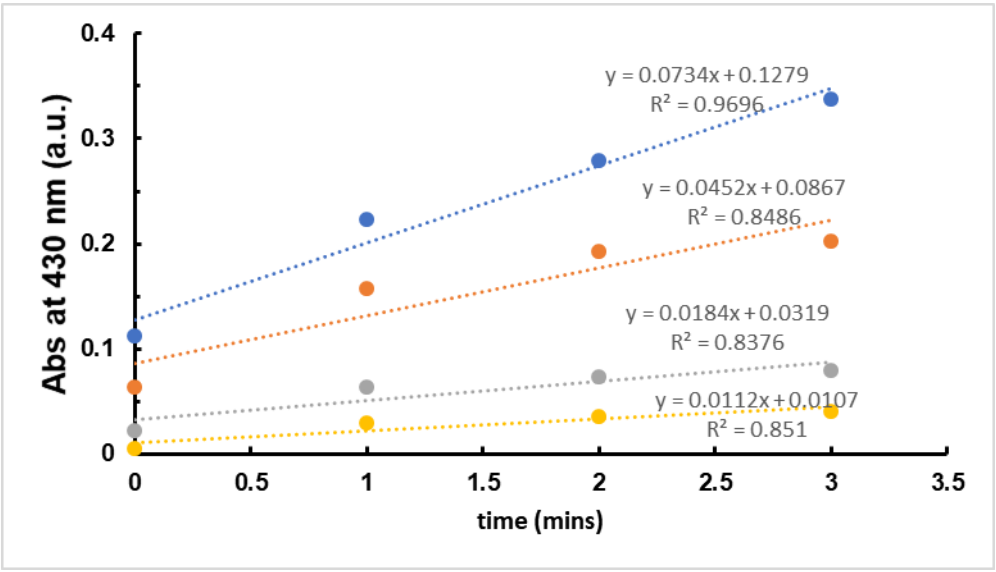

Figure C.S18. RF at 50W absorbance measurements of for activity of thermolysin at substrate concentrations of 0.2 (yellow), 0.5 (grey), 2 (orange) and 4 mg/mL (blue)

Once the velocities were found, from the slopes of the lines shown in the figures above, these were converted from units of min-1 to M product produced per min using the molar absorptivity of TNBSA with a primary amine.[6]

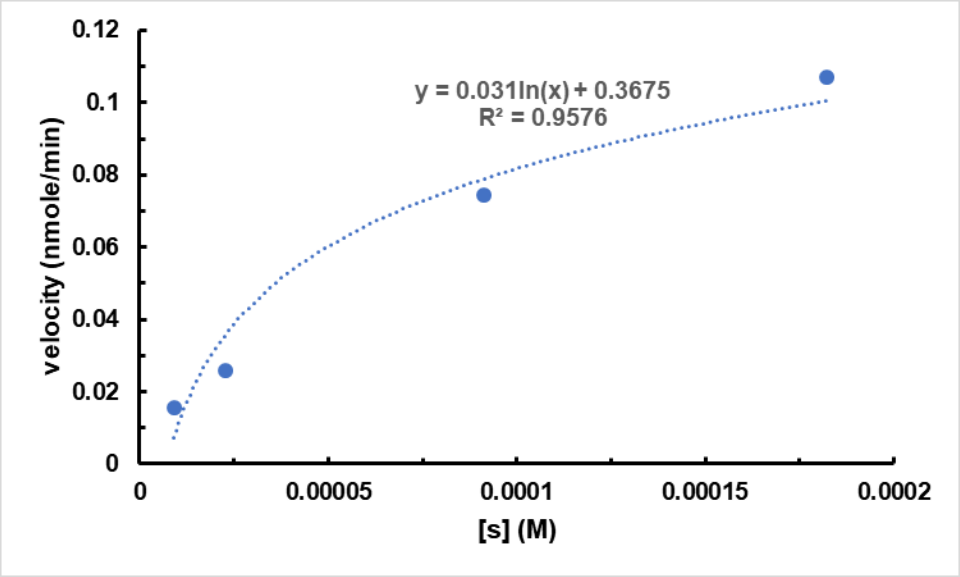

Figure C.S19. Results of velocity vs substrate concentration for bulk heating experiments at 17°C.

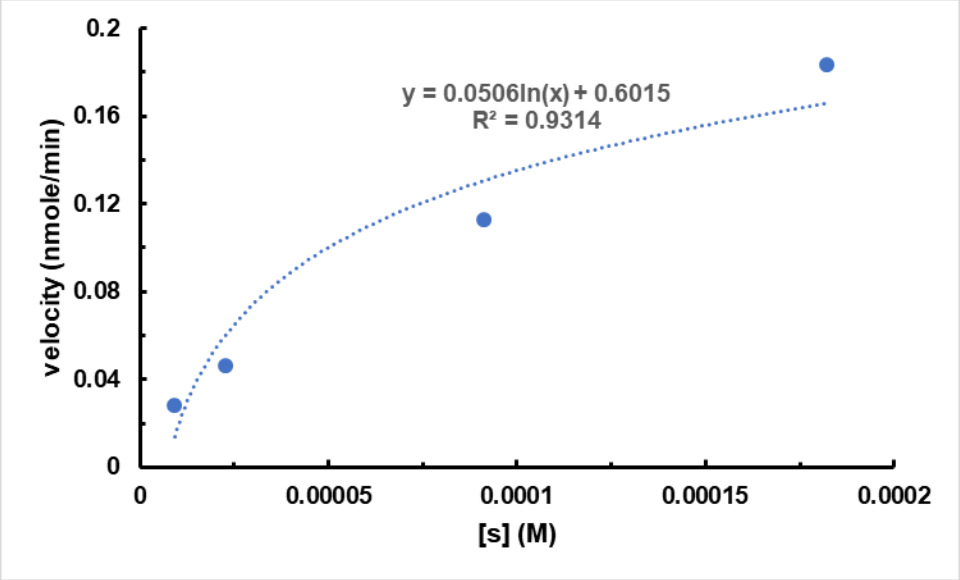

Figure C.S20. Results of velocity vs substrate concentration for RF heating experiments at 50 W.

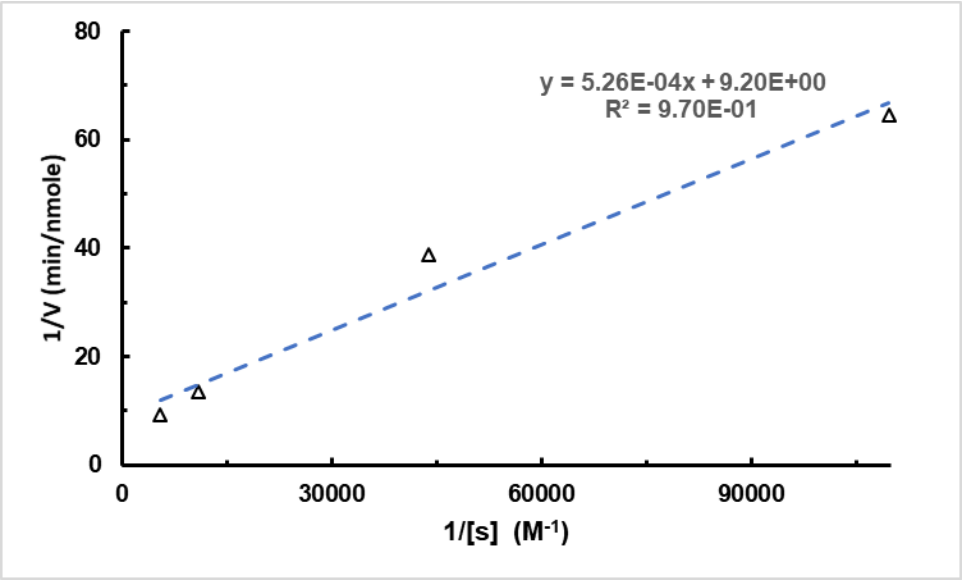

Figure C.S21. Double reciprocal (Lineweaver-Burk) plot of velocity vs substrate from above for thermolysin conjugates in absence of RF field. The slope and intercept were used to determine Km and Vmax.

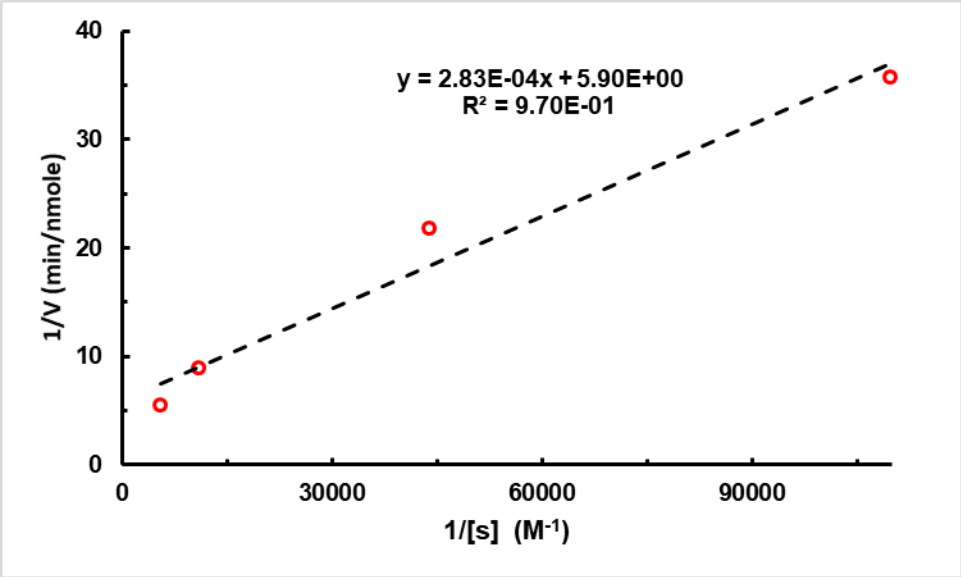

Figure C.S22. Double reciprocal (Lineweaver-Burk) plot of velocity vs substrate from above for thermolysin conjugates in 50W RF field. The slope and intercept were used to determine Km and Vmax.

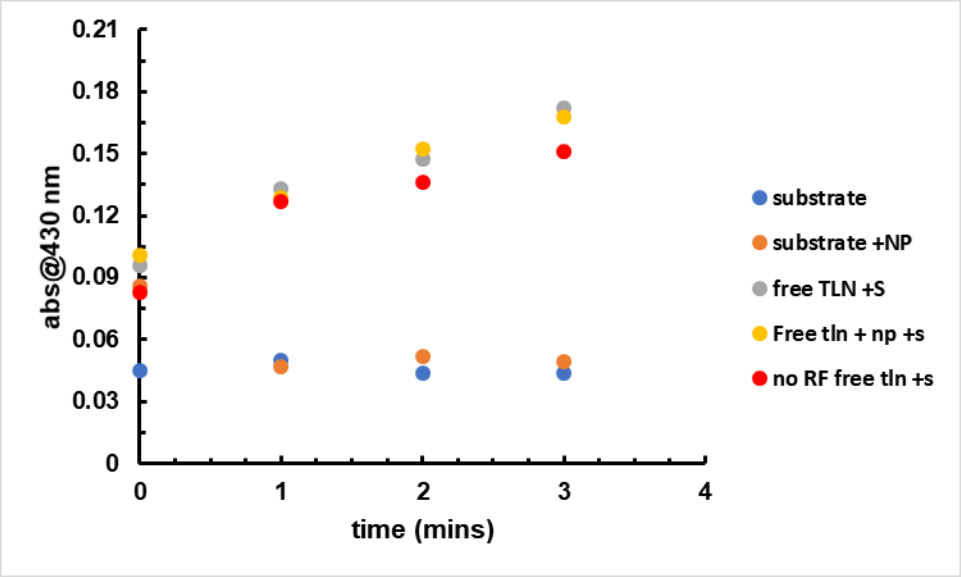

Figure C.S23. Assay results from average of three control experiments in 80W RF field, labels are in legend. S is substrate, NP is for nanoparticles and tln is for thermolysin

REFERENCES

1. Sun, S.; Zeng, H.; Robinson, D. B.; Raoux, S.; Rice, P. M.; Wang, S. X.; Li, G. Monodisperse MFe2O4 (M = Fe, Co, Mn) Nanoparticles. *J. Am. Chem. Soc.* **2004**, *126*, 273–279.

2. WangWang; Luo, J.; Fan, Q.; Suzuki, M.; Suzuki, I. S.; Engelhard, M. H.; Lin, Y.; Kim, N.; Wang, J. Q.; Zhong, C.-J. Monodispersed Core−Shell Fe3O4@Au Nanoparticles. *J. Phys. Chem. B* **2005**, *109*, 21593–21601.

3. Laaksonen, T.; Ahonen, P.; Johans, C.; Kontturi, K. Stability and Electrostatics of Mercaptoundecanoic Acid-Capped Gold Nanoparticles with Varying Counterion Size. *ChemPhysChem* **2006**, *7*, 2143–2149.

4. Kokate, M.; Garadkar, K.; Gole, A. One Pot Synthesis of Magnetite–silica Nanocomposites: Applications as Tags, Entrapment Matrix and in Water Purification. *J. Mater. Chem. A* **2013**, *1*, 2022–2029.

5. Hinterwirth, H.; Kappel, S.; Waitz, T.; Prohaska, T.; Lindner, W.; Lämmerhofer, M. Quantifying Thiol Ligand Density of Self-Assembled Monolayers on Gold Nanoparticles by Inductively Coupled Plasma–Mass Spectrometry. *ACS Nano* **2013**, *7*, 1129–1136.

6. Hatakeyama, T.; Kohzaki, H.; Yamasaki, N. A Microassay for Proteases Using Succinylcasein as a Substrate. *Anal. Biochem.* **1992**, *204*, 181–184.